Investigation into the Effect of Surface Modifications on Hydrogen Evolution Reaction Efficiency and Electrode Longevity During Water Electrolysis



Ciara Smullen B.Sc. (Hons)

School of Physical Sciences, Dublin City University

Submitted for fulfilment of the qualification

Master of Science, M.Sc.

August 2026

Supervised by Dr. Robert O'Connor

Declaration

I hereby certify that this material, which I now submit for assessment on the programme of study leading to the award of Master of Science (M.Sc.) is entirely my own work, and that I have exercised reasonable care to ensure that the work is original and have conformed to the regulations on the use and declaration of Generative AI, and does not to the best of my knowledge breach any law of copyright, and has not been taken from the work of others save and to the extent that such work has been cited and acknowledged within the text of my work. I hereby certify that no Generative Artificial Intelligence (Gen AI) tools have been used in the creation of the thesis.

Signed: Ciara Smullen (Candidate)

ID No.: 20729439

Date: 25/08/2026

Acknowledgements

I would firstly like to thank my close friends and family for their constant support and attempts to understand my research over the past few years. To my parents, Kathleen and James, thank you for giving me the opportunity to pursue my education and unlimited encouragement throughout every aspect of my life. Thank you to my nanny Freda who I had the pleasure to call my housemate for many years of college. I also want to thank my partner Oran for always reminding me of what I am capable of and believing in everything I do.

Thank you to everyone who worked on the wider project that my research was a part of, I thoroughly enjoyed being exposed to knowledge from many different disciplines. A special appreciation for Dr. Michael Brandon, who dedicated countless hours sharing his in-depth knowledge of electrochemistry and conducting time consuming tests on my samples, which complete the story of this project.

To all the staff in the School of Physical Sciences, thank you for making us postgrads feel as though there is no problem that cannot be fixed and keeping the enthusiasm for physics alive. A special thanks to my colleagues and friends in N117 for their teachings, guidance and support, and their ability to somehow create a homely atmosphere in an office space.

Lastly, I would like to express my sincere gratitude to my supervisor Dr. Robert O'Connor. Thank you for giving me the opportunity to work on this project and for offering constant support and advice throughout.

Table of Contents

Declaration i
Acknowledgements ii
List of Abbreviations v
List of Figures vi
Abstract viii
1. Introduction 1
1.1 Project Motivation 1
1.2 Electrolysis of Water 4
1.3 Project Aims 7
2. Experimental Techniques 10
2.1 Electrode Surface Characterisation 10
2.1.1 X-ray Photoelectron Spectroscopy 10
2.1.1.1 Theory 10
2.1.1.2 Experimental 12
2.1.1.3 Analysis 14
2.1.2 Scanning Electron Microscopy 19
2.2 Electrode Surface Modification 22
2.2.1 RF Generated Plasma 22
2.2.2 Atomic Layer Deposition 25
2.2.2.1 Theory 25
2.2.2.2 Experimental 29
2.3 Electrochemical Characterisation 30
2.3.1 Cyclic Voltammetry 30
2.3.2 Electrochemical Impedance Spectroscopy 32
2.3.3 Electrochemically Active Surface Area 33
2.3.4 Acknowledgments 34
3. Development and Characterisation of HER Electrode Surfaces 35
3.1 Introduction 35
3.2 Experimental Procedure 37
3.3 Results 40
4. Effect of Plasma Modification on HER Electrode Surfaces 53
4.1 Introduction 53
4.2 Experimental Procedure 53
4.3 Results 55

5. PEALD of TiO_2 Protective Coatings for HER Electrode 69
5.1 Introduction 69
5.2 Experimental Procedure 70
5.3 Results 72
6. Conclusions and Future Work 82
6.1 Conclusions 82
6.2 Future Work 84
Bibliography 86
Appendix A 94
Appendix B 96

List of Abbreviations

ALD	Atomic layer deposition
AMU	Automatic matching unit
BE	Binding energy
BSE	Back scattered electrons
CCUS	Carbon capture, utilisation and storage
C_{DL}	Double layer capacitance
CE	Counter electrode
CPS	Counts per second
CV	Cyclic voltammetry
CVD	Chemical vapour deposition
DMF	Dimethylformamide
ECSA	Electrochemically active surface area
EDS	Energy dispersive x-ray spectroscopy
EIS	Electrical impedance spectroscopy
FWHM	Full width at half maximum
GHG	Green house gas
GPC	Growth per cycle
HER	Hydrogen evolution reaction
ICP	Inductively coupled plasma
IMFP	Inelastic mean free path
KE	Kinetic energy
LDH	Double layered hydroxide
MOF	Metal organic framework
OER	Oxygen evolution reaction
PEALD	Plasma enhanced ALD
PEC	Photoelectrochemical cell
PEM	Polymer electrolyte membrane
PVD	Physical vapour deposition
RE	Reference electrode
RF	Radio frequency
RHE	Reversible hydrogen electrode
RMS	Root mean squared
RSF	Relative sensitivity factor
SE	Secondary electrons
SEM	Scanning electron microscopy
SHE	Standard hydrogen electrode
SMR	Steam methane reforming
SOS	Spin-orbit split
TALD	Thermal ALD
TDMAT	Tetrakis(dimethylamino)titanium(IV)
TGA	Thermogravimetric analysis
TTIP	Titanium isopropoxide
UHV	Ultra-high vacuum
WE	Working electrode
XPS	X-ray photoelectron spectroscopy

List of Figures

Figure 1.1 Colour terms associated with H_2 production technologies of different carbon footprints (10). 3
Figure 1.2 Types of electrolysers: (i) PEM, (ii) Alkaline, and (iii) membraneless cells. 7
Figure 2.1 Fundamental kinetics of the photoelectric effect. 11
Figure 2.2 Schematic of a typical XPS experimental setup 14
Figure 2.3 Schematic of a conventional experimental SEM setup adapted from literature (37). 20
Figure 2.4 Varying electron escape depths for the electron beam used in SEM. 21
Figure 2.5 Schematic of general ICP 65 plasma source used in this study (44). 24
Figure 2.6 General 4-step ALD cycle where in Step 1 the precursor is pulsed into the ALD chamber and reacts with the sample surface until a complete monolayer is formed. The remaining unreacted precursor is then purged from the chamber in Step 2 completing the first half-cycle. The co-reactant is pulsed in Step 3 where it reacts with the previously formed layer from the precursor. Lastly the chamber is again purged in Step 4 to remove any unreacted co-reactant before the cycle is repeated until a desired film thickness is reached 26
Figure 2.7 The ALD Process Chamber used in this study from Oxford Instruments (44). 29
Figure 2.8 Schematic of H-type electrochemical cell and electrodes. 31
Figure 3.1 Stages of the Ru/Ni-MOF electrode production and control sample synthesis. 36
Figure 3.2 Polarisation curves of different catalyst loadings of Ru/Ni-MOF vs unloaded NF. 41
Figure 3.3 Polarisation curve for each phase of electrode preparation. 42
Figure 3.4 Double layer capacitance values for the Ru/Ni-MOF and Ru/NF and Ru/NiLDH controls, derived from CV experiments. 43
Figure 3.5 Comparison of NF, Ni-MOF and Ru/Ni-MOF survey spectra. 45
Figure 3.6 High resolution XPS spectra showing overlapping of C 1s, Ru 3d and K 2p regions. 46
Figure 3.7 High resolution XPS spectra showing the change in the Ni 2p region following the growth of the NiLDH on the NF substrate. 47
Figure 3.8 SEM images for NF (a & b) and NiLDH (c & d) samples showing growth of the sacrificial metal source layer on the substrate 48
Figure 3.9 Deconvoluted XPS high resolution spectra of the overlapping C 1s and Ru 3d region for the Ru/Ni-MOF sample. 49
Figure 3.10 XPS high resolution spectra of the Ru 3p region for the Ru/Ni-MOF sample. 49
Figure 3.11 XPS high resolution spectra of the O 1s region for the NF, NiLDH, Ni-MOF and Ru/Ni-MOF samples 50
Figure 3.12 SEM of a Ru/Ni-MOF sample pre (a & b) and post (c & d) a long term H_2 production experiment of approximately 200 hours. 51
Figure 3.13 Half-cell chronopotentiometry experiments conducted to evaluate the stability of the Ru/Ni-MOF sample at constant current densities of J = 60 mA/cm^2 and 100 mA/cm^2. 52
Figure 4.1 High resolution XPS spectra for the NF surface taken during the 270°C and 100°C NH_3-based plasma treatments 58
Figure 4.2 XPS high resolution spectrum of the N 1s region showing evidence of signal after a 6 minute NH_3-based plasma of the NF sample despite not being detected in the survey spectrum. 59
Figure 4.3 XPS High resolution spectra for the Ru/Ni-MOF taken during the 270°C and 100°C NH_3-based plasma treatments 60
Figure 4.4 SEM images of the Ru-Ni-MOF sample (a & b) and NF control (c & d) after a 6 minute NH_3-based plasma treatment at 270°C. 62

Figure 4.5 SEM images of the Ru/Ni-MOF sample (a & b) and NF control (c & d) after a 6 minute NH_3-based plasma treatment at 100°C. 63
Figure 4.6 Polarisation curve showing the change in overpotential of the Ru/Ni-MOF and 6 m NH_3-based plasma treated Ru/Ni-MOF. 64
Figure 4.7 XPS survey spectra for different H_2 plasma timed treatments of NF. 65
Figure 4.8 (a) O 1s, (b) Ni 2p, and (c) C 1s high resolution XPS spectra for the NF before and after 5, 10, 15 and 20 minute H_2 plasma treatment. 66
Figure 4.9 (a) O 1s, (b) Ni 2p, and (c) C 1s high resolution XPS spectra of the 20 minute H_2 plasma treated NF after 5 and 10 minute re-exposures to the atmosphere. 67
Figure 5.1 Structure of Tetrakis(dimethylamino) titanium (TDMAT) precursor molecule. 71
Figure 5.2 Survey Spectra of NF control pre and post 50 ALD TiO_2 cycles. 74
Figure 5.3 XPS high resolution spectra evolution as a function of increasing ALD TiO_2 cycles of the (a) C 1s/Ru 3d, (b) Ni 2p and (c) O 1s regions for the Ru/Ni-MOF and (d) Ti 2p region of the NF control. 75
Figure 5.4 Characterisation CVs for NF control samples before and after TiO_2 ALD coating and post HER. 76
Figure 5.5 Polarisation curves for 2 mg/cm^3 Ru/Ni-MOF and NF before and after 50 cycles of TiO_2 ALD. 77
Figure 5.6 Chronopotentiometry experiments conducted to test the stability of the Ru/Ni-MOF electrode before and after 50 cycles of TiO_2 ALD at J = 60mA/cm^2 and 100 mA/cm^2. Bare Ru/Ni-MOF data was previously presented in Figure 3.13. 78
Figure 5.7 Polarisation curves for 3.5 mg/cm^3 Ru/Ni-MOF and NF before and after 50 cycles of TiO_2 ALD. 79
Figure 5.8 SEM images of the Ru/Ni-MOF before (a & b) and after (c & d) and the NF control before (e & f) and after (g & h) 50 cycles of TiO_2 ALD. 80
Figure B1 Non-uniform growth and green appearance of the Ni LDH on the Ni foam substrate shown as produced 96
Figure B2 Ni LDH sample after physical thinning was carried out to obtain a loading of approximately 3 mg/cm^3. 96

Investigation into the Effect of Surface Modifications on Hydrogen Evolution Reaction Efficiency and Electrode Longevity.

Ciara Smullen

Abstract

Targets set by the European Union to reach climate neutrality by 2050 create requirements for improved renewable energy storage solutions in Ireland. The production of renewable energy fluctuates depending on the availability of the source with solar energy, for example, at its peak during the summer months, yet declining in the winter. At peak production time there can be an excess of energy that exceeds the demand of the grid, which can be lost due to lacking storage solutions. However, if there are sufficient storage systems, the surplus can be saved for later use when production dwindles. Hydrogen is known for its high capacity to store energy compared to solid fuels. The production of H_2 through the electrolysis of water using renewable electricity is one method of helping achieve a green storage solution. Membraneless electrolysis cell designs are an innovative approach to remove current barriers towards this method of H_2 production by using less precious metal electrocatalysts and removing the requirement for pure water and components that are rapidly eroded by harsh pH conditions. Metal Organic Frameworks (MOFs) are a growing base for the electrocatalysts used in hydrogen evolution reactions (HERs) due to their ability to provide structure to the catalyst while having large surface areas for reactions.

This study first investigates the efficiency and longevity of a Ru/Ni-MOF electrode for HER in alkaline solutions. As increased surface areas are associated with increased reactions, plasma modifications are conducted to improve electrochemical performance. Environments required for HERs can cause electrode degradation therefore the effect of atomic layer deposited TiO_2 coatings on electrode stability is also reported. The change in surface chemistry and morphology is observed using surface analysis techniques such as x-ray photoelectron spectroscopy and scanning electron microscopy, whilst the electrochemical properties are monitored using cyclic voltammetry and electrical impedance spectroscopy.

1. Introduction

1.1 Project Motivation

Climate change has been recognised as a cause of significant harm to the environment and human health by increasing the risk of extreme heatwaves, floods, biodiversity loss, and food and water scarcity (1). This change is predominantly brought on by the increased production of greenhouse gases (GHGs), such as carbon dioxide (CO_2) and methane (CH_4), through the combustion of fossil fuels (2). The Earth's temperature is kept in equilibrium once it radiates the same amount of heat that it absorbs from the sun. The molecules that make up more than 99.5% of our atmosphere such as nitrogen (N), diatomic oxygen (O_2) and lone noble gas atoms do not interact with the Earth's radiation and therefore do not impact the energy balance. Contrarily, GHGs can absorb and redirect the outgoing radiation causing the atmosphere to warm. What differentiates whether a molecule will interact with this radiation or not depends on quantum mechanics. If the molecule can possess an off-balance electric charge, the shifting electric and magnetic fields of the Earth's radiation can cause it to vibrate. The vibration motion requires energy which is absorbed from a passing radiation wave with the corresponding wavelength that matches one of the quantum states of the molecule. An excited state is then generated and lasts for a few seconds before radiation is released as it returns to ground state. This radiation can propagate in any direction and is typically absorbed by a nearby molecule, eventually escaping to space after a much longer journey through the atmosphere. Therefore, an increase in the amount of GHGs in the atmosphere makes it more difficult for heat to escape and the Earth's radiation increases in order to reach a new, hotter equilibrium. If the addition of GHGs to the air continues

the Earth will proceed with reaching new equilibriums and hence warming the atmosphere (3). With global energy-related CO_2 emissions hitting a new record high exceeding 38 billion tonnes in 2025, an emphasis on increasing accessibility to cost-efficient, green energy sources is crucial to minimise global warming (4).

International bodies including the European Union (EU) have proposed targets for their members to achieve climate neutrality by 2050 in efforts to minimise global warming effects by the end of the century. The government of Ireland has proposed the National Hydrogen Strategy, which includes policies and initiatives, to help achieve net-zero GHG emissions on the island within this deadline (5). With Ireland importing around 81% of its energy sources in 2023, most of which came from fossil fuels, there is opportunity to increase the renewable energy produced within the country to supply green, cost-effective and independent energy (6).

Hydrogen (H_2) is a promising renewable energy contender due to its potential as a zero-carbon energy carrier to store and transfer 140 MJ/kg, almost three times that of the average solid fuel (50 MJ/kg) (7). It has the potential to aid decarbonisation of a variety of applications including energy storage, heavy transport vehicle fuels and in industrial operations (8). H_2 is normally found bonded to other elements, such as in water molecules (H_2O) or natural gas (CH_4), and can be obtained by using energy to split these bonds. Although it is not yet an official grading system, the production of H_2 is often split into different colour categories, referred to as the 'hydrogen rainbow'. Incer-Valverde et al., published an extensive review of the commonly assigned colours in literature (9), and a colour code to enable fast recognition of the source of H_2 molecules, the production process and the energy used to fuel it. As H_2 can be produced from multiple

sources and methods, such as steam methane reforming (SMR), electrolysis or photochemical processes, the code contains up to ten colour grades, with the 4 most commonly reported grades being grey, blue, turquoise and green hydrogen as demonstrated in Figure 1.1. Grey hydrogen, the most popular method of production, uses SMR without carbon capture, utilisation, and storage (CCUS) technologies. This category uses fossil fuels as the energy source, releasing large amounts of emissions, and makes up for 83% of H_2 production. Blue hydrogen is also produced by SMR, however involves CCUS to recycle the CO_2 emissions created during production. H_2 obtained using methane pyrolysis is referred to as turquoise hydrogen, in which CH_4 is cleaved into elemental carbon and H_2 and has no direct CO_2 emissions. Lastly, green hydrogen generally describes H_2 obtained by the splitting of water molecules through renewable energy electrolysis. Out of the 94 Mt of H_2 produced in 2021, only 0.04% was produced using green technologies (9). Although H_2 production technologies have been well defined for over a century, fossil fuel based low-cost methods without complex manufacturing processes have dominated the market. Therefore, efforts are required to improve green hydrogen technologies to encourage their replacement of emission heavy processes (9).

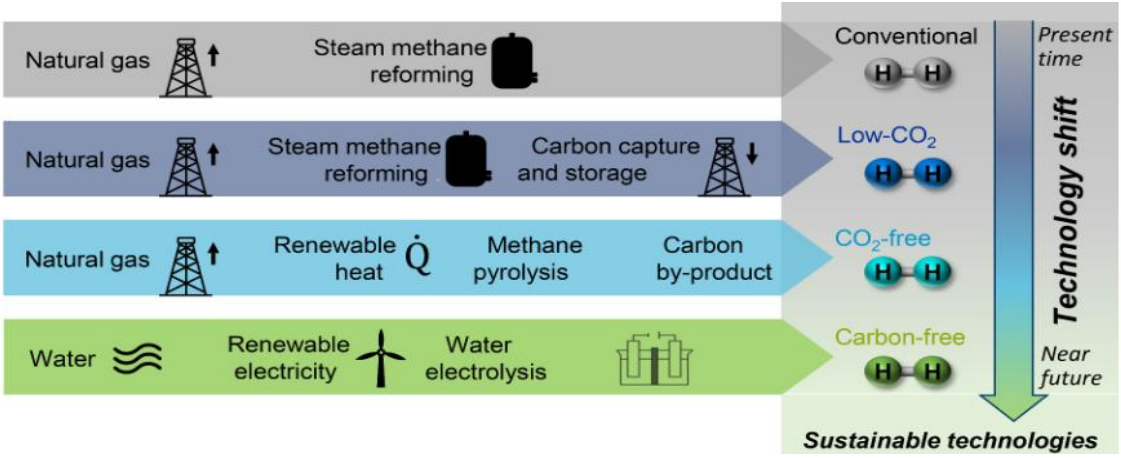


Figure 1.1 Colour terms associated with H_2 production technologies of different carbon footprints (10).

1.2 Electrolysis of Water

The splitting of water molecules using renewable electricity to produce green H_2 has substantial support as the optimal process for encouraging the decarbonisation of many industries. Electrolysis takes place in an electrolyser cell and involves a hydrogen evolution reaction (HER) at the cathode and an oxygen evolution reaction (OER) at the anode. The reactions are driven by an applied voltage that is passed through the cell. The external voltage must surpass the equilibrium voltage of water splitting, typically referred to as 1.23 V in literature for an electrolytic cell at standard temperature and pressure. An electrolyte is used as a conductive medium in which ions travel freely. For acidic electrolytes, the hydrogen ions (H^+) near the cathode gain electrons and are therefore reduced, forming hydrogen atoms. These atoms readily combine to form H_2 gas. However, in electrolytes towards the higher end of the pH scale, such as the KOH used in this study, the concentration of H^+ ions is negligible in comparison to that of water, which results in the reduction of the water molecules instead. The ionic conductivity of the electrolyte causes the hydroxide ions to then flow towards the anode where an oxidation reaction occurs, resulting in O_2 gas (11).

The overall cell reaction for electrolysis in either acidic or alkaline solutions is given by:

$$2H_2O \rightarrow 2H_2 + O_2 \tag{1.1}$$

However, the reactions at the cathode and anode are dependent on the electrolyte used, with the HER and OER for *acidic* mediums described by:

$$2H^+ + 2e^- \rightarrow H_2 \ \ [HER\ acidic] \tag{1.2}$$

$$2H_2O \rightarrow O_2 + \ 4H^+ + \ 4e^- \ \ [OER\ acidic] \tag{1.3}$$

And the corresponding reactions in *alkaline* solutions given by:

$$2H_2O + 2e^- \rightarrow H_2 + 2OH^- \ [HER\ alkaline] \quad (1.4)$$

$$4OH^- \rightarrow O_2 + \ 2H_2O + \ 4e^- \ [OER\ alkaline] \quad (1.5)$$

Conventional polymer electrolyte membrane (PEM) and alkaline electrolysers such as those in Figure 1.2 are the two leading commercially available electrolyser types on the current market. PEM electrolysers contain a solid electrolyte ion-exchange membrane which acts as a physical barrier between the cathode and the anode. This membrane supplies the H^+ ions required for the HER reaction to occur. Perfluorinated sulphonic acid copolymer materials of high ionic conductivity, chemical stability and mechanical strength such as Nafion are widely used for the membranes. The surface of the membrane is deposited with expensive precious metal catalysts which are pressed firmly against the electrodes to obtain high surface contact between the electrolyte and catalyst. They tend to work at high operating current densities (up to 2 A/cm^2) and require deionised water to produce highly pure H_2 (12). Many electrolysers require the use of ultrapure water, to prevent corrosion of sensitive components, of which there is already a global shortage with research showing that 55% of the population experience a scarcity of clean water for at least one month per year (13). Alkaline electrolysers operate at slightly lower current densities (< 0.4 A/cm^2) through the use of a porous separator membrane that contains an alkali electrolyte, typically KOH or NaOH (14). Electrode materials must be permeable to ions so that the resultant products of water electrolysis can travel with ease to the designated storage area. The electrode separator in either type of electrolyser is seen as an essential safety mechanism to prevent potentially explosive mixtures of H_2 and O_2 occurring due to gas bubble cross-over. However, these membranes are inadvertently contributing to the inefficiency of electrolysers in the production of H_2, whilst still arising concerns over preventing

crossover at a larger scale of production (15). Separator membranes tend to have low ionic conductivity with respect to the liquid electrolyte, which can increase the electrical resistance in the cell. The voltage efficiency of PEM and alkaline electrolysers has been reported as up to 68% for operating temperatures of 50-80°C and 70-90°C. In order to achieve net-zero emissions by 2050, the International Energy Agency has listed targets of >80% and >70% efficiency for PEM and alkaline electrolysers respectively, with focus on improving sensitive components and catalyst activity and durability (11). Efficiency can also be reduced when a bubble forms on the electrode surface and fails to release, reducing the free area for reactions to occur. The use of precious metal catalyst such as platinum and iridium drive production costs due to their scarcity and raise concerns over the ethicality of their obtainment (16).

Membraneless electrolysers are an emerging concept in the electrolysis of water that solve many limitations of the previous types. They use complex fluid mechanics to separate the reaction products in place of the separator membrane**.** The lack of a membrane reduces manufacturing and repair costs and makes the cell more resistant to impurities and harsh operating conditions. These electrolysers can operate with lower purity water than required by standard PEM fuel cells and in a range of liquid electrolytes, enabling the reduction of water purification costs and potential use of pH neutral solutions (17). Hence, there is a significant interest in improving membraneless electrolyser efficiency due to their significant potential in the production of green coloured H_2.

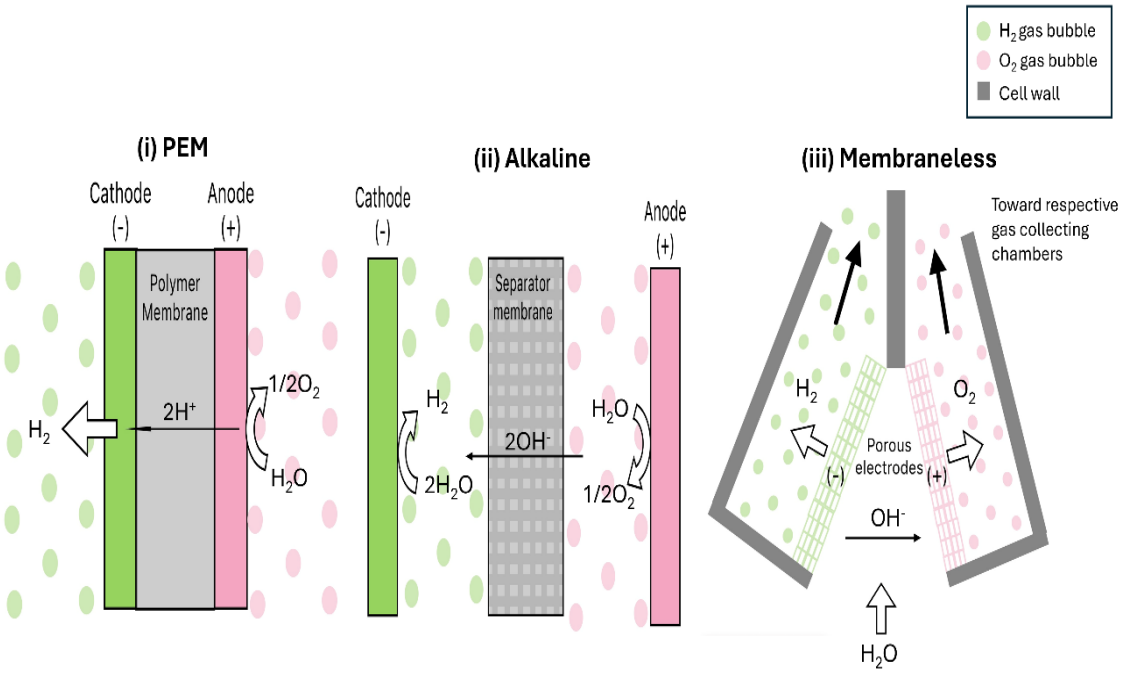


Figure 1.2 Types of electrolysers: (i) PEM, (ii) Alkaline, and (iii) membraneless cells.

1.3 Project Aims

The work in this thesis was conducted as part of a wider project that aimed to introduce a prototype low-cost membraneless electrolyser with the ability to produce green H_2 if renewable electricity is used for electrolysis, resulting in energy production with a minimal carbon footprint. This requires the development of a membraneless electrode which mitigates challenges arising in electrode longevity, safety, sustainability, and cost. The proposed electrolyser design and construction involved collaboration from physicists, chemists, and engineers in DCU and resulted in a 3D printed membraneless electrolyser prototype. The model cell was designed using computational fluid dynamics to promote adequate gas bubble detachment under laminar flow conditions. Cell resistance and gas crossover issues were addressed by optimising the distance and geometry between the electrodes. The HER electrode, or cathode, which is the primary focus of this study, is comprised of a metal organic framework (MOF) catalyst platform grown on a nickel foam (NF) substrate.

The high energy barrier of water splitting in alkaline solutions requires a sufficient catalyst to improve the slow kinetic rate of reaction. The evolution of H_2 gas requires a hydrogen intermediate (H*), of which the formation and desorption process establishes the mechanism and rate of HER. The potential catalytic activity of an element is often described by the Sabatier principle, which states that the interaction between the catalyst and reactant must be neither too strong nor too weak to achieve an ideal catalytic rate (18). The calculation of the free energy of hydrogen adsorption (ΔG_{H^*}) using density functional theory calculations is used to evaluate this interaction, with a high ΔG_{H^*} implying the weak adsorption and generation of H*, and a low ΔG_{H^*} indicating too strong adsorption and therefore difficulty with H_2 desorption. Metal catalysts demonstrating ideal metal-hydrogen binding and therefore HER activity such as Pt and Ir possess $\Delta G_{H^*} \approx 0$. Ruthenium was chosen as the metal catalyst for this study as it possesses a ΔG_{H^*} similar to Pt at a quarter of the price (19). Ru acts as the driving factor of the catalytic activity by reducing the hydrogen adsorption and reaction barriers whilst the MOF structure aids it by providing a high surface area platform for reactions to be seeded.

This thesis reports the characterisation of the HER electrode surface and introduces the effect of surface modifications, such as plasma treatments and the deposition of thin protective films, on electrode HER efficiency and longevity. Chapter 2 details the experimental techniques used to characterise and modify the electrode surfaces at each phase in preparation, whilst the development and the characterisation of the HER electrode is reported in Chapter 3. The plasma modification of the electrode is described in Chapter 4, with the aim of increasing the surface area available for catalyst deposition, activity and thus efficiency. As electrode surfaces suffer from degradation during

hydrogen evolution, Chapter 5 outlines the atomic layer deposition (ALD) of protective coatings or thin films on the electrodes with the aim of increasing longevity with minimal change to performance.

2. Experimental Techniques

2.1 Electrode Surface Characterisation

2.1.1 X-ray Photoelectron Spectroscopy

2.1.1.1 Theory

The primary instrument used in this study is a custom-built integrated Oxford Instruments FlexAL II ALD Reactor (base pressure close to 10^{-6} Torr) coupled in vacuum to a Scienta Omicron X-ray photoelectron spectrometer (XPS) (monochromatic Al Kα X-ray source, base pressure $1x10^{-8}$ mbar) with a 128 channel Argus CU detector. This instrument allows XPS analysis of the electrode pre and post surface modification without leaving vacuum, hence avoiding atmospheric contamination.

X-ray photoelectron spectroscopy is a core electron spectroscopy technique that allows for the analysis of materials at a surface level. It is used to detect the presence of elements on the surface, their chemical states and quantity. It can also be used to characterise the composition and thickness of thin films. It is based on the photoelectric effect, first discovered by Heinrich Hertz in 1887, and was developed in the mid-twentieth century by Kai Siegbahn in Sweden for which he won the Nobel Prize in 1981 (20). XPS involves the use of monoenergetic soft x-rays to irradiate a material, which causes the emission of electrons from the core level of the atom as demonstrated by Figure 2.1.

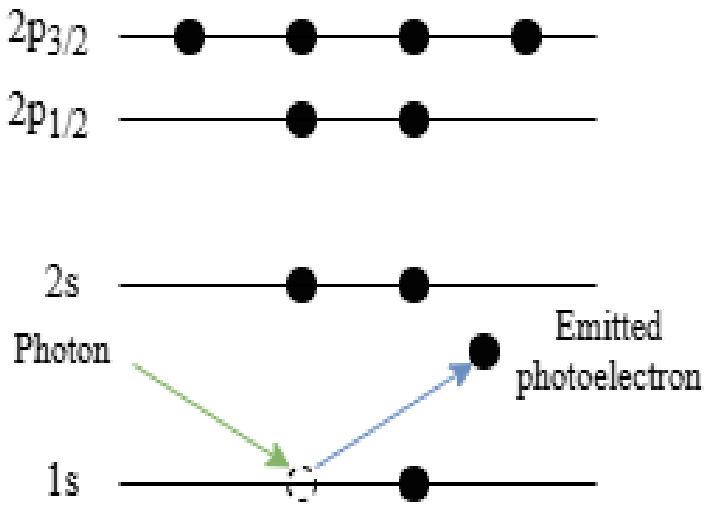


Figure 2.1 Fundamental kinetics of the photoelectric effect.

All elements except for hydrogen and helium can be detected by XPS, which do not appear on the spectra due to their lack of core electrons and small cross-sections (21). Each element has a threshold frequency that it requires the incoming photon to possess in order for a photoelectron to be ejected from the core level (22). This requirement is expressed by equation 2.1, where the energy of the x-ray (*hv*) is equal to the sum of the kinetic energy (*KE*), the binding energy (*BE*), and the work function of the spectrometer (Φ_s).

$$hv = BE + KE + \varphi_s \tag{2.1}$$

The basis of XPS works on the principle that the previous equation can be rearranged to get equation 2.2, to give the BE of an element, as all other components are either constant or measured during the experiment. A relative sensitivity factor (RSF) is included in the calculation as a consideration for the elemental sensitivity as a result of electron scattering. The work function of the spectrometer is included as the BE is measured with respect to the Fermi level rather than to the vacuum level (22).

$$BE = hv - \varphi_s - KE \tag{2.2}$$

The photoemission of an electron from each orbital in each element has an associated binding energy which is widely described in literature and is constant regardless of the x-ray source used (23,24). The peaks are therefore described by the element and core level from which the electron was ejected, for example C 1s refers to the emission of an electron from the 1s orbital of carbon.

2.1.1.2 Experimental

Typical XPS instrumentation is comprised of an x-ray source, a detector, an analyser, a sample stage, and electrostatic lenses. These components are housed in low pressure environments, in the order of 1×10^{-8} mbar. Ultra-high vacuum (UHV) is required for XPS for a multitude of reasons. The first is to reduce the amount of surface contamination that occurs to the sample. It takes approximately 1 s for a surface to adsorb a monolayer of gas at 10^{-6} mbar, meaning that layers of contamination can occur in the typical timeframe for spectral acquisition, leading to an inaccurate profile of the sample. A high-pressure environment also contains a higher number of air molecules with which the photoelectrons can collide, reducing their inelastic mean free path (IMFP) and the likelihood of reaching the detector before scattering. The IMFP refers to the average distance travelled by an electron with a specific KE before inelastically scattering (25). An increased number of scattered electrons reduces the total spectral intensity, while simultaneously increasing the noise (26). Certain XPS components can also be damaged whilst operating in low vacuum such as the analyser and gauges.

Historically, XPS systems contained a dual anode source, of both Al and Mg anodes, which meant that x-rays of two different energies could be generated. Anodes are typically comprised of a copper base material which is coated with either Mg (1253.6

eV) or Al (1486.6 eV). Water cooling is used to remove heat generated from converted electron energy to prevent thermal damage to the source. The x-rays are generated by bombarding one of the anodes with electrons produced from the heating of a tungsten filament. It is possible for the second anode to produce a small number of undesired x-rays if it is accidently bombarded during the use of the first anode, resulting in so called ghost peaks. These peaks often appear at a different BE than expected for the relevant element, as they have been excited by a different energy than expected and cause confusion during analysis. There also is an increased amount of background signal and Bremsstrahlung radiation (artefacts) when using twin anode sources, therefore, modern XPS systems are likely to have a single anode, typically Al, coupled with a monochromator. The monochromator utilises a quartz crystal to Bragg reflect the x-rays towards the sample, allowing for the diffraction of Al Kα lines only. This results in higher resolution spectra where additional Bremsstrahlung radiation contaminants are eliminated, the background decreases and photoemission line widths are lower (27).

Photoelectrons that are ejected from the core levels of the atom scatter at different angles. The electrostatic lenses specify the acceptance angle for collecting electrons, where a large angle leads to improved electron collection efficiency. An electric field is applied across the lens to focus the electrons toward the entrance of the analyser. The energy of the electrons impacts the resolution in XPS, with lower energy electrons achieving a greater energy resolution. Therefore, the extraction lenses also work to reduce the electron energy to a user defined pass energy before entering the analyser. A low pass energy tends to be used for high resolution scans whilst a higher pass energy is used for survey scans, where additional electron throughput is required (22).

The electrons then pass through a hemispherical electron analyser such as that in Figure 2.2, which consists of a pair of semi-circular electrodes with a potential difference across them. This helps direct electrons of the previous defined pass energy toward the detector where they are counted by the electron multiplier.

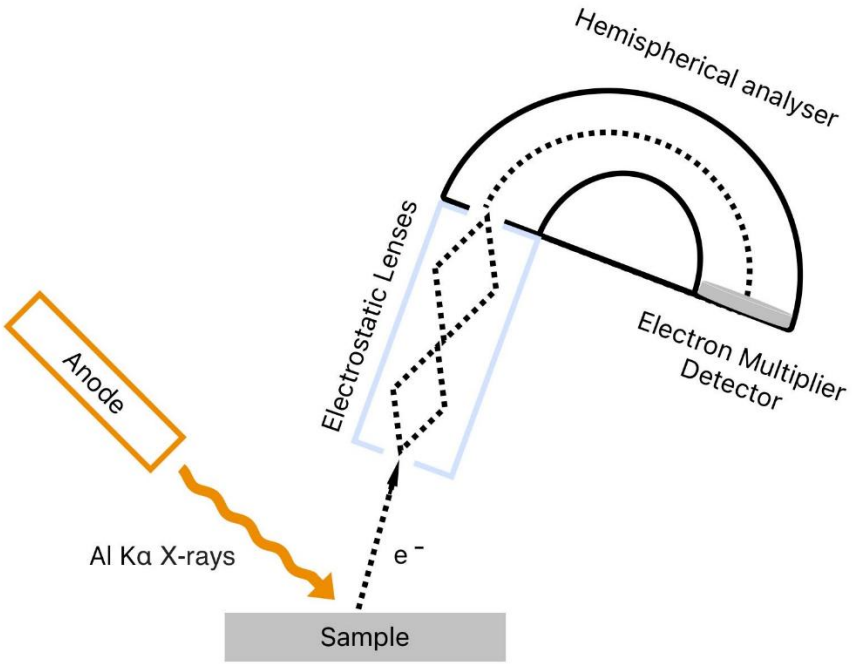


Figure 2.2 Schematic of a typical XPS experimental setup.

2.1.1.3 Analysis

A typical XPS spectrum is a plot of the intensity of the photoemission peak in counts per seconds (CPS) as a function of decreasing binding energy in electron volts (eV). Elements which are present in high quantities typically have peaks from multiple orbitals in expected ratios visible on the spectra (21). Basic peak identification and elemental composition information can be determined through survey spectra, whilst high resolution spectra are used for intense analysis of the precise chemical environment, including bonding and oxidation state studies.

XPS is known as a surface sensitive technique with an analysis depth of ~ 10 nm. This depth is determined by the IMFP of the photoelectrons. In an elastic collision, the kinetic

energy of the electrons is conserved, whereas it is converted to other forms of energy in an inelastic collision. Electrons that have a further distance to travel to the sample's surface are more likely to inelastically scatter before they can escape. The effect of the depth of the electron on the photoemission intensity can be described by the exponential attenuation function known as the Beer-Lambert equation:

$$I_K = I_O e\left(-\frac{d}{\lambda_{IMFP} cos\Theta}\right) \quad (2.3)$$

Where the initial and final photoemission signal intensities are given by I_o and I_K respectively, d represents the distance the electron travels, λ_{IMFP} is the IMFP of the sample and θ is the angle the electrons are emitted at with respect to the surface normal (28).

The elemental composition of a sample determined by XPS depends heavily on the element sensitivity. This sensitivity is based on the binding energy, cross-section, and the photoemission probability. The intensity (I_p) of a photoemission peak for a homogenous sample is given by:

$$I_P = J\rho\sigma \mathrm{K}\lambda_{IMFP} \quad (2.4)$$

With J as the photon flux, ρ the atomic concentration, σ the photoelectric cross-section, K being a constant which describes the instrumental factors and λ the attenuation length of the electron. Assuming a constant photon flux, the σ, K and λ elements of equation 2.4 can be united as a single unique RSF associated with the core level of each element. The Scofield database of RSFs was used in this study obtained from the CasaXPS element library. As some elements have a higher sensitivity than others, a correction must be made to accurately compare photoemission intensities of different elements. The

intensities are generally determined by attributing the size of the area under the peak to the quantity of that element. This area is then divided by the RSF so that the normalised peak intensity is obtained:

$$Relative\ Peak\ Intensity = \frac{Measured\ Peak\ Area}{RSF} \quad (2.5)$$

Allowing for the further calculation of the total elemental composition for the sample:

$$Atomic\ \% = \frac{Relative\ Peak\ Intensity}{\Sigma\ Relative\ Peak\ Intensities}\ x\ 100 \quad (2.6)$$

Uncertainty in determining peak intensities can occur in XPS based on factors such as varying levels of contamination and instrument performance. However, XPS is typically a highly precise characterisation technique with the ability to detect changes in composition within approximately 1% (29).

Peak fitting is carried out on the high resolution scans to identify the different chemical states and the respective concentrations present in the sample. The fitting technique consists of creating a model consisting of component peaks and a background algorithm to account for secondary scattered electrons (30). Curve fitting software such as CasaXPS is used to insert a mathematical function known as the lineshape, and to constrain the fitting parameters such as the background, full width at half maximum (FWHM), position, and area. The contribution to the signal from inelastically scattered electrons must be removed to create accurate intensities for quantification. A Shirley background is typically used as it estimates the change in the background signal to be proportional to the peak intensity above the background at a fixed binding energy, whereas linear and Tougaard backgrounds are less common (28). Once the background is subtracted, peak areas combined with a RSF can be used to accurately determine concentrations.

The lineshape chosen during curve fitting depends on the asymmetry of the peak and the fluctuation of the Gaussian-Lorentzian character. The Gaussian contribution is modified by instrumental factors whilst the Lorentzian component depends on the uncertainty in the lifetime of the core-hole as a result of photoemission, which decreases with increasing atomic number. The Gaussian impact is therefore instrument dependant whilst Lorentzian broadening is consistent for each element. The measured lineshape is a convolution of the Gaussian and Lorentzian functions known as the Voigt function. Gaussian-Lorentzian (GL) line shape typically suits symmetrical peak shapes whilst the asymmetric Lorentzian (LA) and the finite Lorentzian (LF) incorporate an exponential tail appropriate for fitting asymmetric signals (30).

Sample charging occurs with insulating samples when the emission of photoelectrons without fast enough replenishment gives rise to a net positive. Charging can cause peaks to shift to higher BE and increase peak distortions such as broadening or the addition of satellite peaks. The effects of charging can be minimised during sample preparation by creating an electrical contact with a sample holder that is grounded. An electron flood gun can also be used to supply a stream of low energy electrons to neutralise the charge on the sample surface during scanning. The parameters of the gun are changed until the narrowest peaks at the expected binding energy are achieved. Additionally, in data analysis software such as CasaXPS, it is possible to correct the energy scale by using a reference peak. As adventitious carbon is present on almost all surfaces exposed to atmosphere, it is common to shift the lowest binding energy C 1s peak to approximately 284.8 eV. All peaks present in the corresponding high resolution spectra taken for the sample are then shifted by the same amount, assuming that the rest of the sample undergoes the same charging behaviour. As the nature of absorbed carbon can vary,

there have been arguments made against the use of the C 1s for referencing (31). However, due to the lack of alternative charge referencing methods its use is continued and widely reported in literature (32).

XPS peaks are described using the terminology of n*, l* and *j* where *n* is the quantum number, *l* is the orbital angular momentum number and *j* is the total angular momentum number and is equal to the sum of the orbital angular momentum number and the spin projection (*s = ± ½)* as in the equation:

$$j = l + s \tag{2.7}$$

Core-levels with an orbital angular momentum ≥ 1, such as those from the p, d, and f orbitals, occur as doublets as a result of the spin-orbit split, whilst peaks arising from the photoemission of an electron from an s orbital will occur as a singlet. The ratio of the doublet areas depends on the degeneracy of the electronic levels (*2j + 1*) and are as show in Table 2.1 (33).

Table 2.1 Spin-orbit split properties (33)*.*

Subshell	**Total angular momentum number, j**	**Ratio of peak areas**
s	1/2	-
p	1/2, 3/2	1:2
d	3/2, 5/2	2:3
f	5/2, 7/2	3:4

The FWHM of a peak is primarily influenced by the core-hole lifetime. Broader peak shapes tend to be the result of shorter lived core-holes. The FWHM of spin-orbit peaks that are close together tend to be similar, however, the width varies with increasing separation due to the Coster-Kronig effect. The Coster-Kronig effect is a type of emission where the core-hole and relaxing electron originate from the same core level, resulting in broader peak widths for the higher BE component peak. This effect is particularly observed in first and second row transition metals, complicating analysis (34).

2.1.2 Scanning Electron Microscopy

Scanning electron microscopy (SEM) is a technique that uses a beam of high energy electrons used to gain information on a sample surface morphology and topography. The large depth of field of SEM (1mm – 0.4 µm) compared to optical microscopes (55.5 µm – 0.19 µm) makes it a superior method for observing surfaces with complex 3D structures such as MOFs. Its broad magnification range (10x – 300,000x) and ability to reach high resolutions (~ 1-10 nm) make it a popular instrument used in research, especially in material science (35).

A typical SEM setup, as shown in Figure 2.3, consists of an electron gun, condenser and objective lenses, deflectors and a detector, all performing under vacuum pressure. A high vacuum (~10^{-8} Torr) is required to reduce the effects of electron scattering due to collisions with atmospheric molecules, and also to prevent damage to pressure sensitive microscope equipment (36). Images of high resolution are achieved through the careful control of SEM parameters including the magnification, brightness and contrast, accelerating voltage, working distance and probe current.

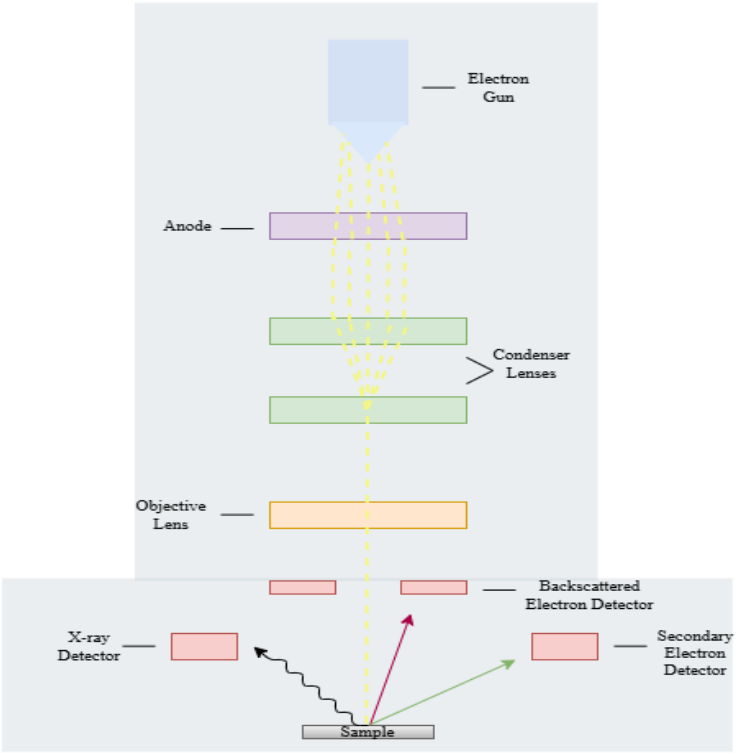


Figure 2.3 Schematic of a conventional experimental SEM setup adapted from literature (37).

Typical electron sources used in SEM include thermionic tungsten or LaB_6 guns, or field emission guns. The SEM used in this study involved a thermionic gun as the electron supply. The tungsten filament cathode inside of the gun is heated to high temperatures (>1000 K) by an applied current, causing electrons to emit from the cathode surface and are accelerated to an energy range of 2-30 kV. The cross section of the beam produced is typically too large to result in clear images at high magnifications, therefore the use of electron lenses reduces the beam diameter so that a more focused beam of high energy electrons interacts with the sample surface. A signal of electrons generated by the sample surface is then picked up by the detector and is used to create an image on a connecting computer display (37). Although the beam generates up to nine types of signals from the sample, that of the secondary electrons (SE) and backscattered electrons (BSE) are the most commonly used to produce SEM images. Auger electrons have the shallowest escape depth whilst X-rays (photons) reach significantly further into

the sample as seen in Figure 2.4. The SE escape from the surface of the sample as a result of inelastic collisions and therefore are low energy electrons (< 50 eV), whilst BSE gain energy (> 50 eV) from multiple elastic collisions and can be used to build compositional information about the sample (37).

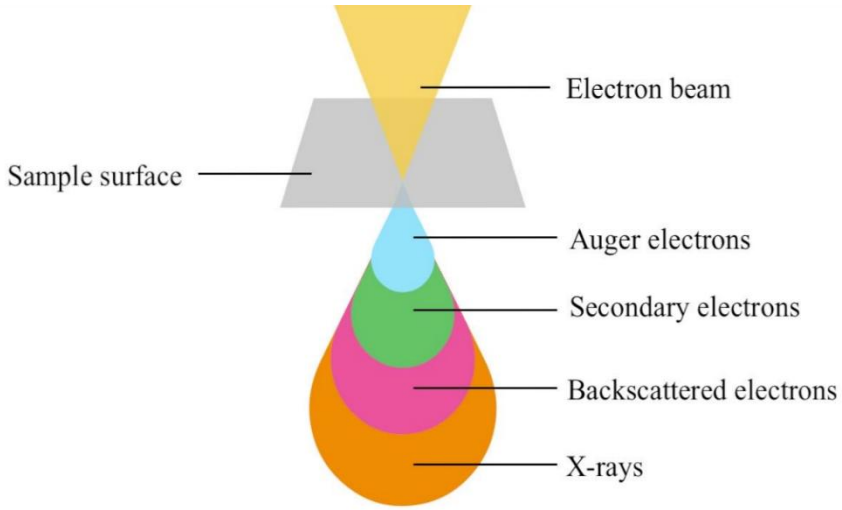


Figure 2.4 Varying electron escape depths for the electron beam used in SEM.

Energy dispersive X-ray spectroscopy (EDS) is another mode of SEM that can be used to observe a spectrum of the energy intensities of the X-rays. It has been used in conjunction with SEM to create elemental maps of samples to show the distribution of elements and check for clustering. It is particularly useful in catalysis, as activity can depend on loading and available metal surface area, which relates to the distribution, size and morphology of the catalytic nanoparticles (38). EDS was not employed in this study due to the magnetic properties of the NF substrate which would interfere with the magnetic field within the field emission-SEM available to the author for EDS but has the potential to be highly beneficial in ensuring uniform deposition of catalysts and thin films. SE imaging exclusively was carried out in this work using a JEOL JSM-IT 100 InTouchScope SEM.

2.2 Electrode Surface Modification

2.2.1 RF Generated Plasma

2.2.1.1 Theory

Plasma is known as the fourth state of matter and is generated through the application of a significant amount of energy to a gaseous substance. Chemical reactions, heat or electrical fields can be used to supply the energy required to partially or fully ionise a gas, transforming it into a plasma. Plasma consists of electrons, ions and uncharged particles that are constantly interacting to create a collectively quasineutral charge. The most common method of igniting a plasma is by an electric field, which can be constant (DC), alternating (AC), or at radio (RF) or microwave frequencies. Plasma technologies can be found in a wide variety of applications, it is used to generate light in neon signs and energy saving bulbs, to etch microscopic components in the microelectronics industry, for sterilisation of biomedical devices such as contact lenses and implants and also to deposit thin films for the protection of surfaces from corrosion (39,40). Its popularity is rising due to its potential as a highly efficient, environmentally friendly and controllable surface modification technique. Plasma can be generated using gases such as H_2, Ar, NH_3 or O_2 with the choice of gas depending on the desired effect on the substrate. NH_3 as a plasma source is particularly advantageous where the nitridation or extensive roughening of a surface is required, whilst O_2 and H_2 plasmas are used for oxidation or the removal of atmospheric contaminants from surfaces respectively (41). Plasma treatments have potential for improving water splitting technologies through the synthesis and modification of electrocatalytic materials. Their use has been reported to

increase specific surface areas and porosity of electrode surfaces and in the deposition and dispersion of catalysts (42,43). A comparative study of the effects of a NH_3 and a H_2 RF generated plasma on the electrochemical activity of the Ru/Ni-MOF electrode is reported in this thesis (43).

2.2.1.2 Experimental

The FlexAL II process chamber was used for the generation of H_2 and NH_3 plasmas in this study. Figure 2.5 shows the expanded schematic of the inductively coupled plasma (ICP) 65 source, illustrated by Oxford Instruments Plasma Technology, situated inside the chamber. The process gas is chosen based on the desired resultant plasma and is supplied to the gas ring within the chamber and to the top of the insulating tube with flows ranging from 10 to 200 sccm. The operating pressure of the process varies from 1 to 60 mTorr and an optimal pressure for plasma striking should be determined with regards to the remaining process parameters. The gas is ignited to a plasma using the power supplied from the RF generator at a frequency of 13.56 MHz, which has a maximum power output of 300 W. The automatic matching unit (AMU) matches the impedance of the ion source and the process chamber to that of the RF generator to ensure maximum power transfer to create an efficient process. The plasma is created in the insulating tube under vacuum as a result of the power supplied to the RF coil. Resultant ozone is removed through the NW40 pumping port included in the screening cover. N_2 is supplied to the chamber for use as an inert gas for chamber venting and purging of process components (44).

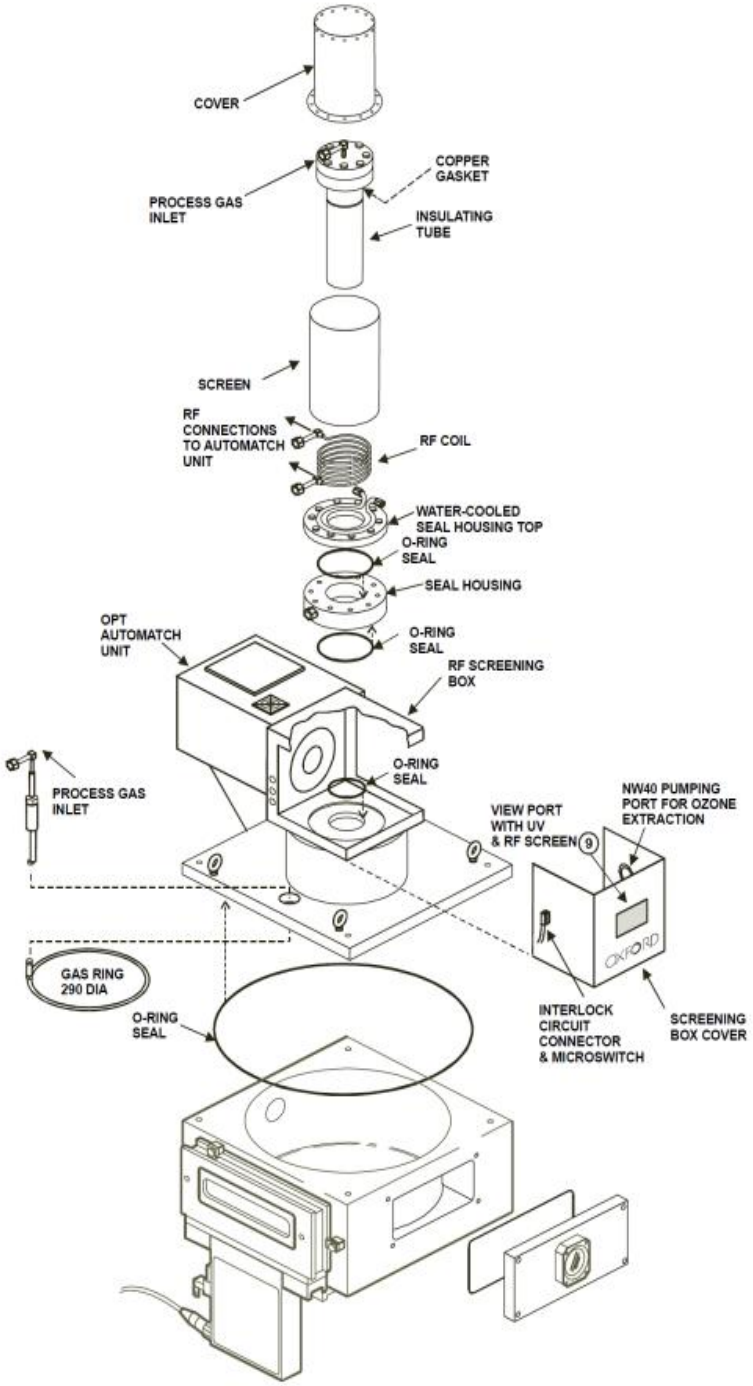


Figure 2.5 Schematic of general ICP 65 plasma source used in this study (44).

2.2.2 Atomic Layer Deposition

2.2.2.1 Theory

Atomic Layer Deposition (ALD) is a popular technique used to produce thin films in semiconductor and energy industries and has been reported to increase the stability of water splitting components of photoelectrochemical cells (PEC) (45,46). The PEC works by the photovoltaic effect where an incident electromagnetic radiation is used to create a potential difference across two semiconductor materials. One of the primary semiconductor materials used in PEC applications is silicon which tends to be unstable in aqueous solutions. The use of harsh pH electrolytes and high potentials can cause photo-corrosion of the Si resulting in the loss of active surface area and the formation of insulating layers. The Si surface can also become inactivated due to photo-passivation, where the interaction of the semiconductor with O_2 in the electrolyte results in the formation of an oxide layer on its surface (47). TiO_2 has been widely investigated as a suitable protective coating for photoelectrodes as it is earth-abundant and provides high stability during water splitting (48). ALD is a suitable mechanism for the application of these coatings due its monolayer-by-monolayer deposition technique, which increases the distance between the electrode and the site of reactions whilst avoiding passivation of the surface (49). Due to the success of ALD in the deposition of protective coatings for photoelectrodes, its application for increasing the stability of electrodes in electrochemical water splitting is investigated in this study.

Modern day ALD is the result of individual work by researchers in the former Soviet Union and Finland in the 1960s and 70s respectively (50). It is a variant of chemical vapour deposition (CVD) but is advantageous due to its self-limiting nature allowing

increased control over film properties. CVD introduces both of the gaseous chemical reactants to the chamber at once, whilst ALD does this in an alternating step manor, allowing for a controlled deposition of materials as demonstrated by Figure 2.6. In a typical four step ALD cycle, the substrate is first exposed to the chemical precursor, where the desired material is deposited on the surface upon reaction. A single monolayer of material is deposited with the reaction stopping once all sites available have been interacted with. This is followed by a purge step with a flow of inert gas, usually Ar or N_2, to remove any unreacted precursor in the chamber before the introduction of the co-reactant in the third step. The same procedure is repeated for the co-reactant until a full cycle is completed after the fourth step. Hence, the reactions regarding the precursor and the co-reactant are independently referred to as half-cycles. The uniformity and conformality of ALD films make it an excellent deposition technique for the coating of complex 3D structures such as MOFs (51).

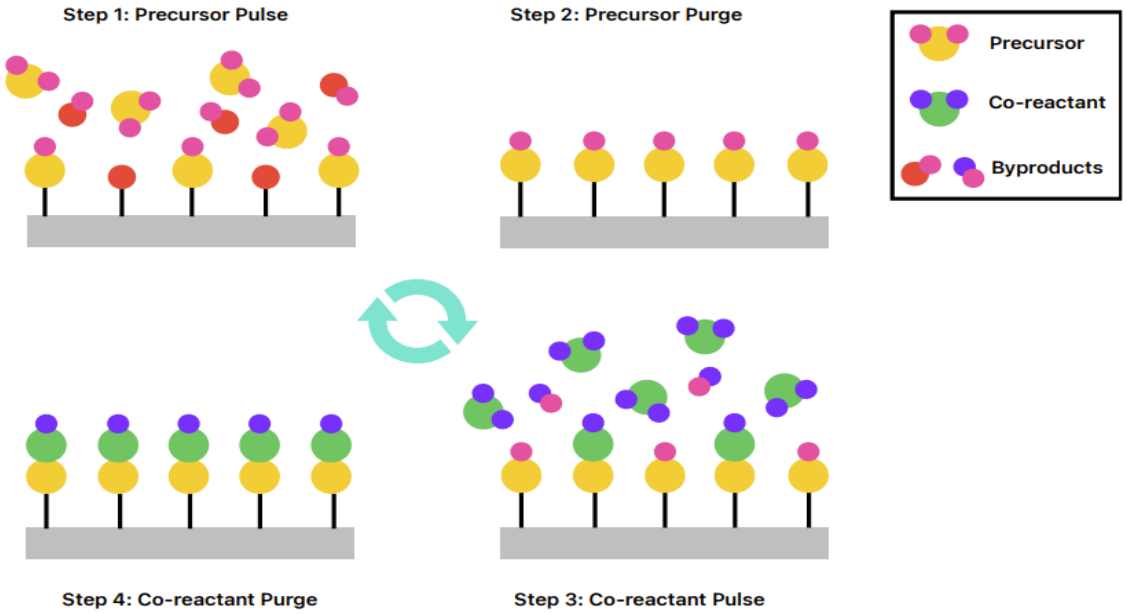


Figure 2.6 General 4-step ALD cycle where in Step 1 the precursor is pulsed into the ALD chamber and reacts with the sample surface until a complete monolayer is formed. The remaining unreacted precursor is then purged from the chamber in Step 2 completing the first half-cycle. The co-reactant is pulsed in Step 3 where it reacts with the previously formed layer from the precursor. Lastly the chamber is again purged in Step 4 to remove any unreacted co-reactant before the cycle is repeated until a desired film thickness is reached.

Two methods of performing ALD are through thermal ALD (TALD) or plasma enhanced ALD (PEALD). To achieve the required energy for reactions to take place, the substrate must be heated to relatively high temperatures in TALD. However, in PEALD the energy is supplied through the ignition of a plasma co-reactant, removing the requirement of high substrate temperatures and thus allowing for depositions on heat sensitive substrates (52). TALD uses two vapour phase precursors whereas the plasma co-reactant in PEALD ensures increased reactivity of the substrate, allowing for a wider variety of precursor choice. PEALD has also been found to have a higher growth rate than TALD. The growth per cycle (GPC) is an established value used to measure the rate at which the ALD film thickness grows with increasing cycle numbers (53). It can depend on the reactants, dose time, process temperature, and substrate material. The GPC for TiO_2 films grown by PEALD has been reported in literature (54,55) for planar substrates however a quantitative value was not possible to determine during this study due to the complexity of the Ru/Ni-MOF surfaces. O'Donnell et al., detail a cycle-by-cycle investigation of the nucleation and film properties of TiO_2 protective coatings for Si based photoanodes, comparing TALD and PEALD processes for two types of precursors. The group report that the GPC (nm/cycle) was higher for PEALD deposited TiO_2 than for TALD for both tetrakis(dimethylamino)titanium(IV) (TDMAT) and titanium isopropoxide (TTIP) precursors, and that atomic force microscopy studies and root mean squared (RMS) surface roughness (pm) calculations showed the PEALD also yielded smoother films for both precursors (56). PEALD is seen as a generally cleaner process as there are less by-products likely to remain in the chamber due to the use of one precursor compared to two. Palmolahti et al., investigated the effect of growth temperature on precursor breakdown in the ALD of TiO_2 films using TDMAT and water at 100-200°C. They

found that lower deposition temperatures can result in films with less Ti suboxide defects but may contain TDMAT traces, which can effect reducibility of the TiO_2 in later annealing processes to strengthen the photoelectrode for artificial photosynthesis (57). Deposition temperatures at the lower end of the ALD temperature window for TiO_2 described by the chamber manufacturer were chosen for this study due to the potential temperature sensitivity of the Ru/Ni-MOF. For this reason, annealing was also not undertaken, as it typically occurs at temperatures up to 500°C. Thermogravimetric analysis (TGA) could be undertaken in further studies of the Ru/Ni-MOF electrode to determine its stability as a function of increasing temperature, and to identify its suitability for such high temperature processes. However, modifications conducted during this study were deliberately conducted at as low temperature as possible above the highest temperature the catalyst was exposed to during preparation (120°C), to avoid unintentional heat damage.

Overall, the choice of ALD process parameters depends on the desired traits of the film and the substrate requirements. Although the ALD of TiO_2 thin films are regularly reported for photoelectrodes in literature, their application on a Ru/Ni-MOF electrocatalyst is a novel technique to improve HER electrode stability and efficiency. Henceforth, referral to ALD will regard PEALD as it is the primary process used for the deposition of thin TiO_2 films in this study due to the potential temperature sensitivity of the samples and its evidential success in the growth of high-quality films to improve electrochemical activity.

2.2.2.2 Experimental

The deposition of TiO_2 thin films by PEALD was conducted in the FlexAL II process chamber. The ICP 65 plasma source described in section 2.2.1.2 is encased in the ALD process chamber as show in Figure 2.7. The precursor is delivered through the inlet port of which flow is obstructed by the gate valve during a plasma or process step to prevent the precursor from coating the plasma source. There is a conical shield in the upper part of the chamber which accommodates the distribution of reactive species, whilst the lower section contains the electrode. The electrode can be heated to high temperatures if required for the ALD temperature window described by the manufacturer recipes. It is possible to connect an ellipsometer for in-situ film characterisation through the ellipsometry ports, however this was not utilised within this project. The properties of the TiO_2 films deposited within this study were characterised by in-situ XPS and SEM, whilst the effect on electrocatalyst stability was determined using H_2 production experiments.

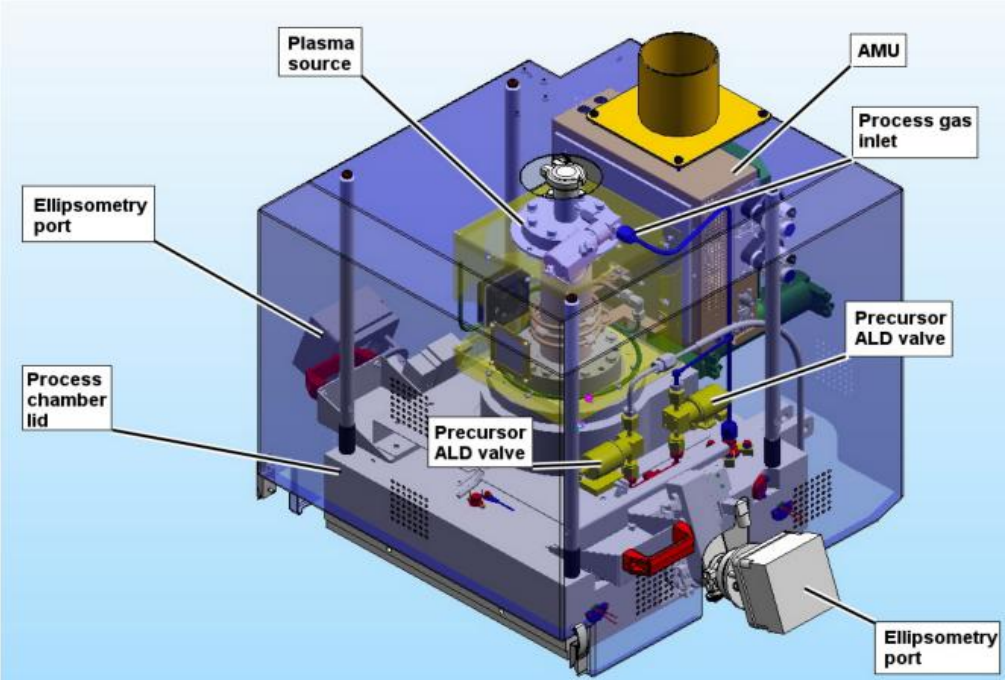


Figure 2.7 The ALD Process Chamber used in this study from Oxford Instruments (44).

2.3 Electrochemical Characterisation

2.3.1 Cyclic Voltammetry

Cyclic Voltammetry (CV) is an electrochemical technique used to study the oxidation and reduction processes for electrode surfaces. It is an invaluable tool used in electrochemistry to compare fundamental characteristics such as the active surface area, overpotential and reaction kinetics of different electrochemical materials that impact performance and stability during water splitting. Therefore, it can be used to observe changes in the forementioned traits of electrode surfaces following surface modifications.

In this study, CV is performed using a H-cell divided by ion-permeable sintered glass such as that shown in Figure 2.8 containing an electrolyte solution in both compartments. The cell contains a working (WE), reference (RE), and counter (CE) electrode. A potential is linearly swept between the WE and RE, whilst the change in current between the WE and CE is recorded using a potentiostat. Electric current generated during HER and OER is referred to as Faradaic current. The WE is the electrode of which the electrochemical properties are of interest. The RE is used as a benchmark to the 0 V mark on the potential scale, with the applied potential therefore reported as 'vs.' the type of RE used. Typical RE used in aqueous solutions for CV are the silver/silver chloride (Ag/AgCl) electrode, the mercury/mercury oxide (Hg/HgO) electrode and the standard hydrogen electrode (SHE). The CE completes the current circuit and tends to be made from platinum or graphite due to their inert properties. The results are presented as cyclic voltammograms, where current density (J) is displayed as a function of the applied

potential (*E*). The scan rate (*v*) describes the rate of change (*mV/s*) at which the potential was varied linearly (58).

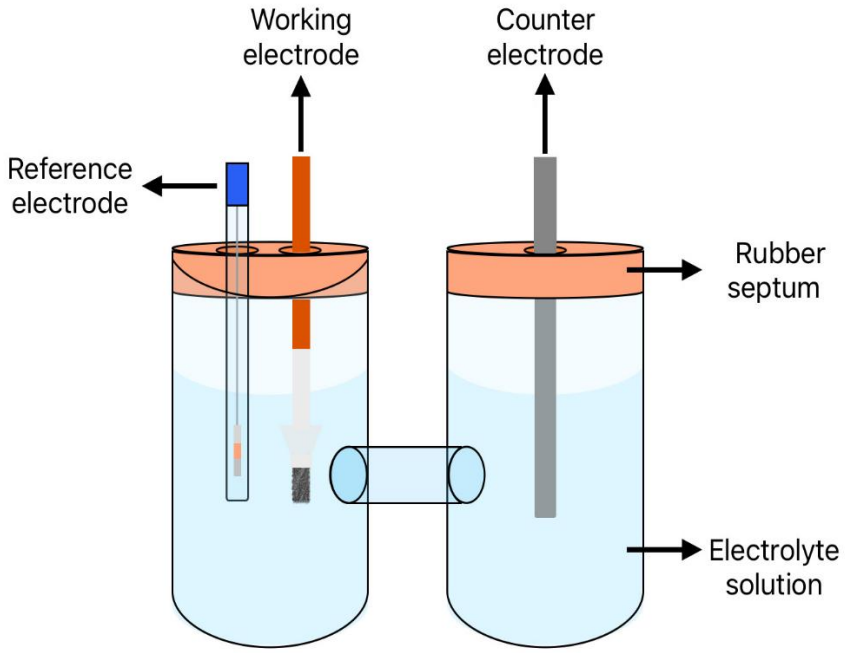


Figure 2.8 Schematic of H-type electrochemical cell and electrodes.

Electrocatalytic performance for HER is often reported in terms of the overpotential (η), which is the difference between the potential required to obtain a particular current density and the thermodynamic potential. It is measured by low scan-rate voltammetry and discussed in reference to the reversible hydrogen electrode (RHE). The current density (J) is determined by dividing the current (I) by the geometric surface area of the electrode, with η often reported for J = 10 mA/cm^2 or J = 100 mA/cm^2. In addition to the reporting of η at these current densities, another essential consideration is the operational stability of the catalyst. An efficient electrolyser should operate at constant J (i.e. at a constant rate of H_2 production) over many hours with a minimal increase in the associated value of η (proportional to the required electrical energy input). An increase in $\eta(t)(j = constant)$ demonstrates deterioration of the catalyst over time,

therefore stability can be measured by polarising the cathode at a constant current density and observing the resultant *E(t)* character.

The potential (E) measured (m) against a Hg/HgO RE ($E_{Hg/HgO\ m}$) can be converted to the RHE scale (E_{RHE}) using the Nerst equation (59):

$$E_{RHE} = E_{Hg/HgO\ m} + (0.0592 \times pH_{electrolyte}) + E_{Hg/HgO\ real} \quad (2.8)$$

where $pH_{electrolyte}$ is the pH of the electrolyte solution and $E_{Hg/HgO\ real}$ is the characteristic potential when the Hg/HgO electrode is filled with 1 M NaOH with a value of 0.1079 V (at 25°C), with the pH value of 1.0 M KOH set as 13.65, the E_{RHE} is simplified to:

$$E_{RHE} = E_{Hg/HgO\ m} + 0.916\ V \quad (2.9)$$

2.3.2 Electrochemical Impedance Spectroscopy

Electrical Impedance Spectroscopy (EIS) is used to determine the impedance of the electrochemical cell by applying either a sinusoidal alternating current (ac) or voltage at a range of frequencies and measuring the response of the corresponding potential or current respectively. EIS can be used to determine the resistance (Ω) of the electrolyte solution, so that an *iR* compensation correction can be applied to account for solution resistance occurring between the RE and WE. The solution resistance (*R*) can be obtained by carrying out an EIS measurement at a potential where no Faradaic current arises at the cathode other than the double layer capacitance (C_{DL}). The C_{DL} or non-Faradaic current is also known as the background current and is a result of the accumulation of balancing electrical charges at the interface between an electrode and an electrolyte solution.

2.3.3 Electrochemically Active Surface Area

The catalytic activity of an electrode is typically proportional to its specific surface area. MOFs are a favourable platform for catalysts due to their high porosity leading to an increased catalytic surface area. The electrochemically active surface area (ECSA) of an electrode is determined through the measurement of the C_{DL}. It is possible to model the interface between an electrode and an electrolyte solution as a capacitance according to the Helmholtz double-layer model (60). The capacitance for a physical parallel plate capacitor is directly proportional to the area of the plate. Using this as an analogy, the capacitance of the double layer is taken to be proportional to the real area of active contact between the electrode and electrolyte solution. The C_{DL} can be determined by recording a series of CVs in the range of potential where no Faradaic current occurs and plotting the measured current as a function of scan rate, where the slope gives the C_{DL} value according to:

$$C_{DL} = \frac{dQ}{dE} = \frac{dQ}{dt} \cdot \frac{dt}{dE} = \frac{i}{v} \tag{2.10}$$

where Q is the surface charge density at a given potential E, i is the double layer capacitive charging current, and v is the is the CV sweep rate or rate of change of the applied potential with time, t. It is possible to calculate a numerical value for the ECSA if a reference value of specific capacitance per unit real surface area, C_{REF}, is known for a given material by:

$$ECSA = C_{DL}/C_{REF} \tag{2.11}$$

However, this type of characterisation is typically used for comparative purposes due to the lack of reliable values of C_{REF} for most materials. For example, if the C_{DL} values are

compared for two similar electrodes, such as the NiLDH and Ni-MOF samples detailed in this study, it can be assumed that the electrode exhibiting a larger C_{DL} value has a larger surface area without determining an absolute numerical value for the ECSA (61).

2.3.4 Acknowledgments

The author would like to thank Dr. Michael Brandon for the development and supply of electrode samples used for physical characterisation and for the acquisition of the electrochemical data presented within this thesis.

3. Development and Characterisation of HER Electrode Surfaces

3.1 Introduction

As outlined in Chapter 1, current commercial electrolysers for water splitting carry limitations which must be overcome for green H_2 to replace fossil fuels in the energy industry. The properties required of an electrode to achieve efficient HER have been widely recognised as the following: (i) being stable to chemical and mechanical stress, (ii) possess a high catalytic activity with a low overpotential, (iii) have a low production cost with regard to an extended lifetime, and (iv) have little to no risk to safety or to the environment during production. The team involved in the wider project created a prototype membraneless electrolyser with the aim of producing green H_2 whilst improving the drawbacks of current electrolyser technologies. The membraneless design reduces the number of components susceptible to corrosion, thereby decreasing the reliance on a supply of high purity water. The growth of MOFs on a Ni foam supported electrode substrate creates a high surface area catalyst platform in which HER can occur. This allows for a reduction in the amount of expensive precious metal-based catalyst required, such as Ru, with the aim of achieving a low overpotential at high current densities. The addition of utilising renewable electricity for the electrolysis results in the production of green coloured H_2.

Chemists at DCU followed a method adapted from literature (62–64) to create a Ru/Ni-MOF catalyst on a nickel foam (NF) substrate for the HER electrode by the process visualised in Figure 3.1 and is detailed in Appendix A. NF was used as the substrate material due to its porous characteristic (3.15 - 4.33 pores per mm, average pore diameter 0.25 mm). A nickel double-layered hydroxide (NiLDH) was grown on the NF as

a sacrificial metal source (65), before being converted to a nickel-based metal-organic-framework (Ni-MOF). The Ni-MOF was doped with Ru catalyst to create the final stage electrode (Ru/Ni-MOF). The suitable Ru loading was determined by creating a range of concentrations (2.0, 2.5, 3.5 mg/cm^3) and investigating the effect of electrode Ru loading by XPS and steady state polarisation tests. NF and NiLDH samples were also doped with Ru to create control samples. These were used to determine if the growth of the MOF increases catalyst retention. Sun et al., observed that for a similar electrocatalyst, the XRD peaks associated with the MOF were lost when the loading of Ru was above 13%, suggesting that high Ru loadings can destroy the MOF structure (63). This chapter details the chemical and physical characterisation of the electrode material at each phase of preparation and post HER.

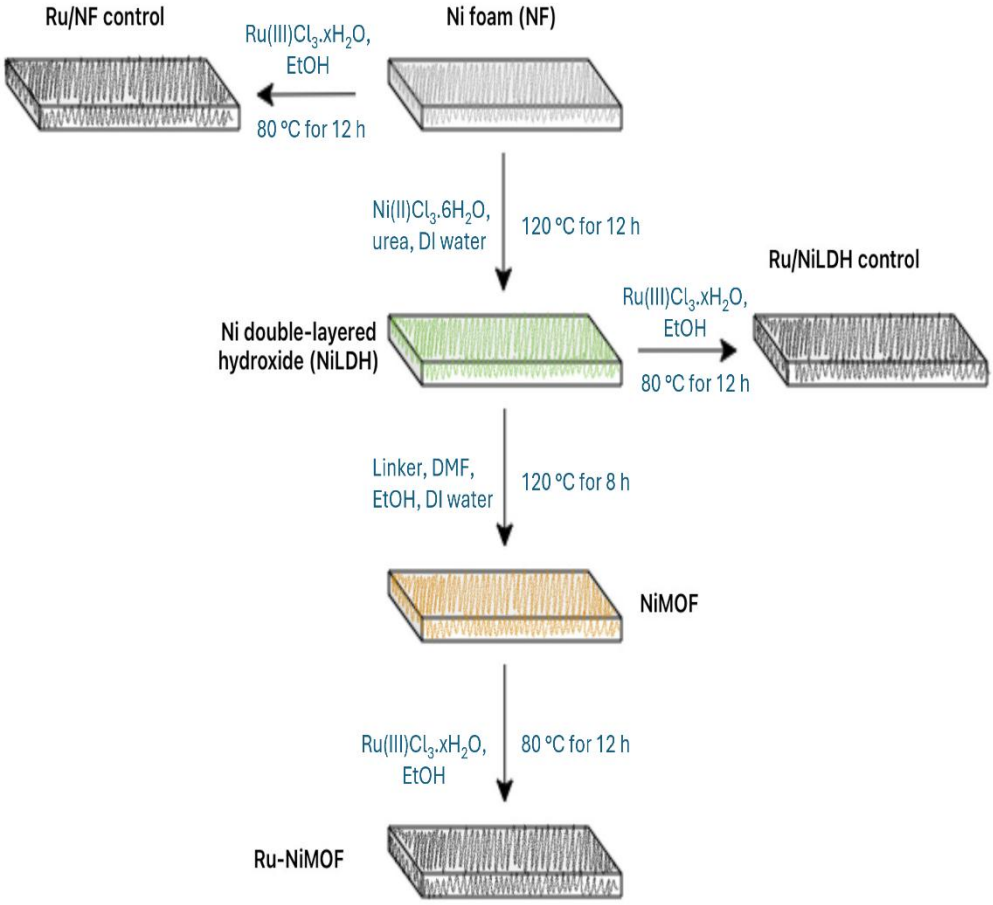


Figure 3.1 Stages of the Ru/Ni-MOF electrode production and control sample synthesis.

3.2 Experimental Procedure

XPS analysis of the electrode surface was conducted at each phase of the preparation and after a long term HER of the Ru/Ni-MOF sample. Survey and high resolution spectra of the C 1s, O 1s, Ni 2p, Ru 3p, N 1s and Cl 2p regions were obtained for the relevant samples with particular focus on the first four regions. The C 1s region was extended where required to include the Ru 3d and K 2p peaks**.** The Ru 3p region was used in place of the Ru 3d region for atomic percentage calculation and determination of oxidation states due to the Ru 3d region overlapping with the C 1s. A Scienta Omicron XPS with a 128 channel Argus CU detector was used to characterise the electrode surface chemistry. Survey scan and high-resolution spectra were obtained using a 1 and 0.1 eV step size respectively, at normal emission. The spectra were fitted with a Shirley-Sherwood background along with Voigt profiles using CasaXPS software. OriginPro was used to stack and overlay spectra. An electron flood gun was operated during scans whilst observing the position of the C-C peak at approximately 284.8 eV in the C 1s region. Electrode morphology was observed using a Jeol JSM-IT 100 InTouchScope SEM in SE mode.

Electrochemical characterisation was performed using a Biologic VSP Potentiostat/Galvanostat controlled by EC-Lab software. Most of the experiments were performed using a two-component glass H-cell. Each compartment was 2.5 cm in diameter with an approximate useable volume of 20 cm^3 and was sealed with a rubber septum. Needles for N_2 purging and venting, and metallic contacts for the electrodes were passed through the septa. The WE was attached to a copper-based crocodile clip crimped to copper wire and sealed using CHT Silcoset 151 Si sealant leaving 0.5 × 0.5 cm

of the electrode exposed. PTFE tape was used to ensure full coverage of the sealed area and clip to avoid contact of any conducting surface except the exposed MOF area with the electrolyte solution as this can introduce additional signal noise. A 1 M KOH solution prepared with 18.2 MΩ/cm resistivity ultrapure distilled water was added to each compartment. The Ru/Ni-MOF working electrode (cathode) and a reference electrode were placed in one compartment and a graphite rod as the counter electrode (anode) placed in the other. A mercury/mercury oxide (Hg/HgO) reference electrode (ALS model RE-61AP) with 1.0 M NaOH filling solution was chosen for the concentrated alkaline solution used in the cell. The cell was placed in a thermostatic water bath held at 25°C during all measurements.

Low scan rate CV was the primary test conducted to investigate the electrochemical activity of the electrodes. The reversible potential for hydrogen evolution was taken as -0.916 V vs Hg/HgO as per section 2.2.1. The typical testing procedure involved sweeping the potential in the negative direction from its initial open circuit value, through the reversible potential and monitoring the rising negative current. The sweep direction was reversed at a specified potential (typically -1.35 V vs Hg/HgO) until the cathode reached a defined upper limit (often -0.76 V vs Hg/HgO), where the process was again reversed to begin another cycle. A scan rate of 2 mV/s was typically used, implying that the i-E data was acquired under quasi-steady state conditions.

EIS measurements were carried out at a potential of -0.5 V vs Hg/HgO which was suitable for the cathodes. A small magnitude ac perturbation (10 mV amplitude) was imposed on top of the applied dc potential. The amplitude and phase of the current response was monitored during the variation of the ac frequency across a range from 200 kHz to 50

mHz. The EC-lab software was used to plot the resultant data in Nyquist plot format, with the negative of the imaginary component of the impedance (-*Z''*) against the real component (*Z'*). The uncompensated solution resistance (R) was directly extracted from the high frequency intercept of the plot with the Z' axis and was typically in the range of 2-2.5 Ohms under the described experimental conditions, with the variation likely due to the slight variability of the distance between the RE and WE.

CVs at scan rates between 100 and 20 mV/s (at 20 mV/s intervals) over a potential range from -0.47 to -0.57 V vs Hg/HgO were used to obtain ECSA measurements for the samples. This potential range corresponds to a region with no visible Faradaic current features. The relevant value for the capacitive current (*i*) was derived from the measured cathodic (i_c) and anodic (i_a) currents at the median potential (E = -0.52 V) according to:

$$i = \frac{|i_c|+|i_a|}{2} \quad (3.1)$$

Where the slope is equal to the C_{DL} for the linear plot of the current as a function of scan rate.

Stability testing was conducted using a variable dc power supply (RS-Pro model D3305P), where the test current density was achieved by operating in constant current mode to polarise the cathode at the negative potential required. A digital multimeter logger (Multicomp Pro model MP730889) was used to measure the potential drop over time across the cathode and an adjacently placed Hg/HgO (1 M NaOH) reference electrode. The electrolyte solution resistance between the WE and RE was measured using EIS in advance of the experiment so that iR compensation could be applied to the *η(t)* data once collected. For long term stability testing, the samples were operated at 60 mA/cm^2

for approximately 70 hours before the current density was increased to 100 mA/cm^2 for over 130 hours.

3.3 Results

The electrochemical performance of Ru/Ni-MOF with three different Ru loadings was compared to that of a non-loaded NF substrate to decide a suitable catalyst loading level. The iR corrected steady state polarisation curves plotted in Figure 3.2 show a dramatic increase in the performance of the Ru/Ni-MOF in comparison to the NF. Although catalytic activity does somewhat improve with concentration, a 2 mg/cm^3 Ru sample does not have a major variation in performance to a 3.5 mg/cm^3 sample. The graph contains two data sets for 3.5 mg/cm^3 Ru loaded samples, which represent two separate batches of Ni-MOF that were created. The slight difference in overpotential between the two samples is assumed to arise from the inherent variation between batches. Considering the data for the 3.5 mg/cm^3 loaded sample (yellow) and 2 mg/cm^3 sample (red) which were created from the same MOF batch, the difference in overpotential is < 10 mV. Therefore, considering the cost efficient and sustainable use of Ru, the minimal increase in performance attained by a 75% increase in $RuCl_3$ was not justifiable.

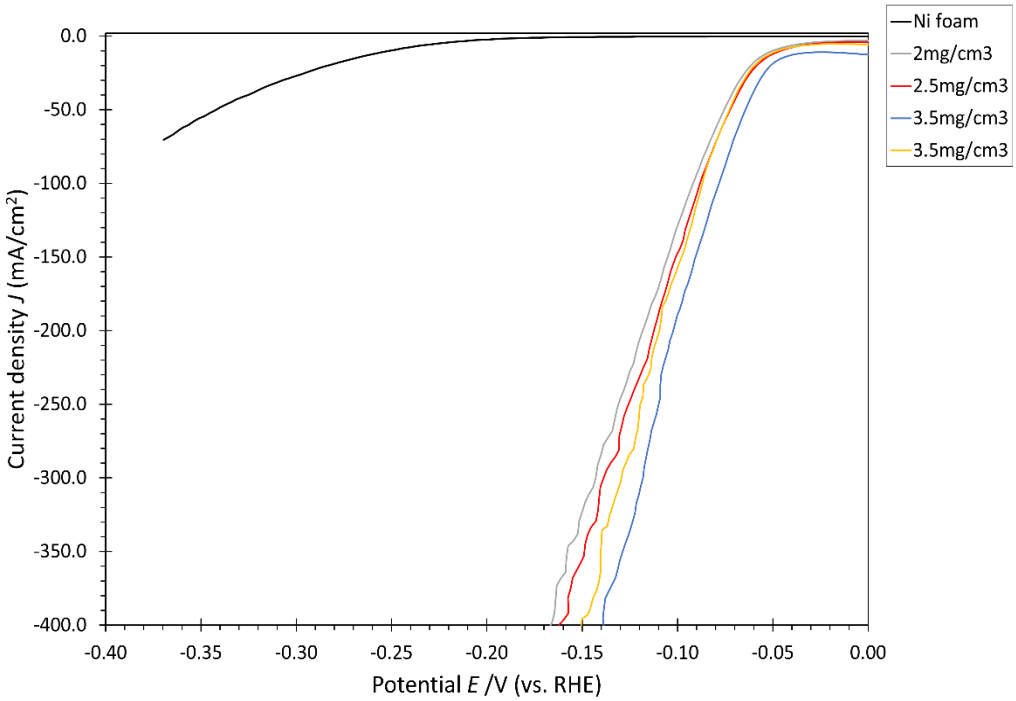


Figure 3.2 Polarisation curves of different catalyst loadings of Ru/Ni-MOF vs unloaded NF.

The overpotential (η) was also compared for each phase of electrode preparation, as presented in Figure 3.3. As the I-V voltammogram measurement by the potentiostat is of high accuracy, the primary source of error in the following reported potentials is a result of the variation in samples due to the non-homogenous nature of the Ru/Ni-MOF as described in Appendix A. It can be observed that the η improves with the addition of the Ru catalyst, with the lowest overpotential of η = 85 mV at a HER current density of J = 100 mA/cm^2 achieved by the Ru/Ni-MOF. This overpotential is impressive compared to that of the state-of-the-art Pt/C electrocatalysts (> 130 mV at J = 100 mA/cm^2) reported in literature for HER (63,64). In comparison to the overpotentials detailed for similar electrode structures, it appears as though the Ru/Ni-MOF retains superiority. Deng et al., who anchored Ru nanoparticles to a Ni-MOF on NF reported $\eta_{J=100} > 100$ mV*, whilst the NiRu-MOF nanosheets on NF developed by Xu et al., achieved $\eta_{J=100} > 150$ mV for HER in alkaline solutions (66,67). The large reduction in overpotential for the Ru/Ni-MOF and the Ru doped control samples compared to the samples without the

catalyst emphasises the capability of Ru in improving electrocatalytic behaviour and was also seen by Tran et al., when comparing the performance of a CoMo-LDH electrode before and after Ru incorporation (68). The improved overpotential for the Ru/Ni-MOF over the Ru/NF and Ru/NiLDH control samples is attributed to the increased catalytic surface area, supported by high double layer capacitance.

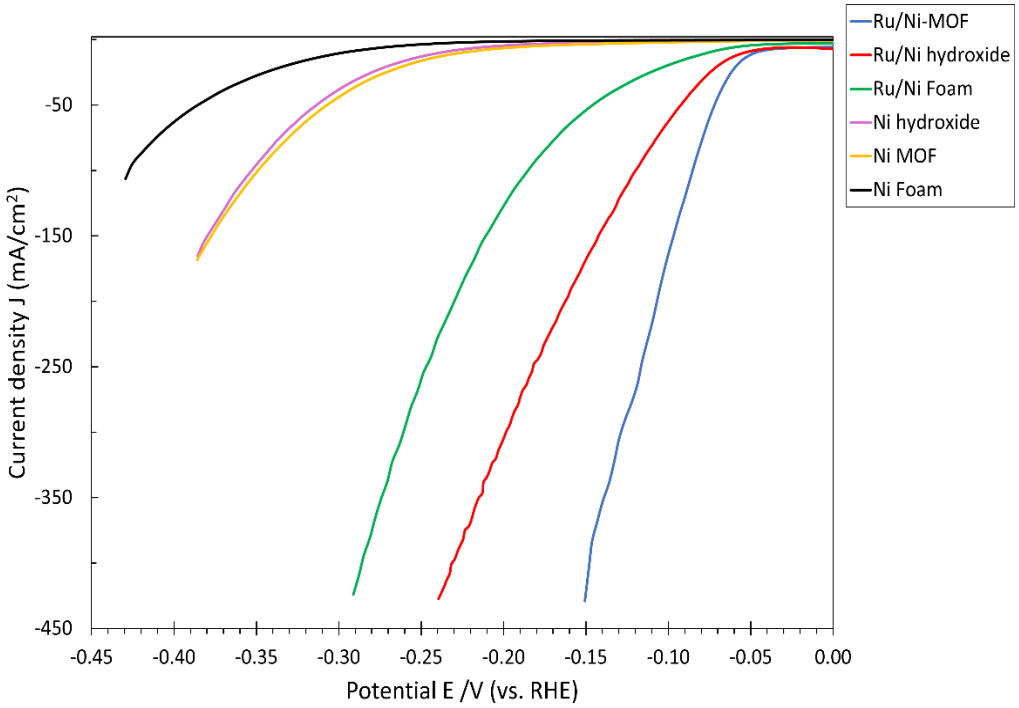


Figure 3.3 Polarisation curve for each phase of electrode preparation.

**Value extracted from reported supplementary data.*

The double layer capacitance (C_{DL}) values in Figure 3.4 for the Ru/Ni-MOF and control electrodes were derived from CV experiments. The C_{DL} values were obtained from the plot of the current density as a function of scan rate, where the slope of the line gave 202 mF/cm^2, 84 mF/cm^2, and 47 mF/cm^2 for the Ru/Ni-MOF, Ru/NiLDH and Ru/NF, respectively. By comparing these values, it can be assumed that the ECSA is greatest for the Ru/Ni-MOF, likely due to its complex 3D structure and high surface area for reactions. The association of increased catalytic performance with higher surface area was also reported by Li et al., who created both 3D and 2D Ru/Ni-MOF structures on NF HER electrodes. When the electrodes were tested in 1 M KOH at J = 100 mA/cm^2, the overpotentials were 68 mV and 122 mV for the 3D and 2D MOFs respectively, further justifying the development of 3D MOFs as a base for the catalyst (64).

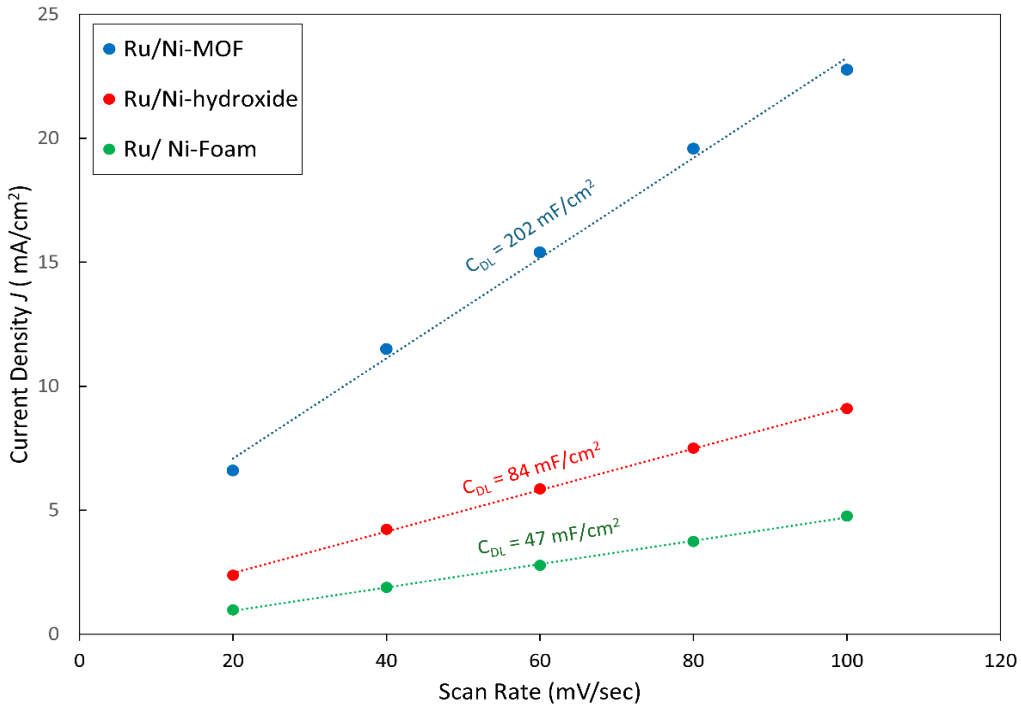


Figure 3.4 Double layer capacitance values for the Ru/Ni-MOF and Ru/NF and Ru/NiLDH controls, derived from CV experiments.

XPS analysis software was used to calculate the atomic percentage of each element present in each sample, as presented in Table 3.1, from the survey spectra based on the

calculations described in section 2.1.1. The recognised error in the calculations and the effect of overlapping regions is considered when interpreting results. The Ni-MOF resulted in the highest retention of Ru compared to the Ru/NF and Ru/NiLDH controls. This result in conjunction with the low overpotential in Figure 3.3 and high ECSA in Figure 3.4 supports the development of the MOF to act as a superior catalyst platform and hence increase catalytic activity compared to the controls. The presence of the Ru 3p peaks proves successful loading of Ru/NF, Ru/NiLDH and Ru/Ni-MOF samples, with 2 mg/cm^3 loading of $RuCl_3$ resulting in sufficient Ru 3p peaks for quantitative analysis. The long term use of the electrode in a high pH solution at high current densities results in a reduction in Ru content which accounts for the increase in overpotential observed in Figure 3.13. A significant percentage of potassium remained with the electrode structure after use in the KOH solution.

Table 3.1: Percent of elements at each phase of electrode synthesis.

	Atomic %						
Electrode phase	*C 1s*	*O 1s*	*Ni 2p*	*N 1s*	*Ru 3p*	*Cl 2p*	*K 2p*
NF	56.54	31.74	11.72	-	-	-	-
Ru/NF	40.18	45.08	9.7	-	5.04	-	-
NiLDH	46.59	39.72	13.69	-	-	-	-
Ru/NiLDH	40.09	41.23	13.19	-	5.49	-	-
Ni-MOF	69.91	19.26	3.91	6.92	-	-	-
Ru/Ni-MOF	51.61	29.11	8.23	4.46	6.59	-	-
Ru/Ni-MOF after long term HER	37.4	41.27	4.76	-	4.11	4.02	8.44

XPS survey spectra of the NF, Ni-MOF and Ru/Ni-MOF are presented in Figure 3.5. The NF spectrum has peaks at binding energies corresponding to Ni, C and O, as expected due to its exposure to the atmosphere. Nitrogen is introduced to the surface chemistry during the development of the Ni-MOF evident by the peak at 400 eV. A small peak around 200 eV can be seen in the survey spectra of the Ru/Ni-MOF attributed to Cl 2p. This peak in addition to the Ru $3p_{3/2}$ and $3p_{1/2}$ peaks, visible at approximately 463 eV and 485 eV, respectively, suggest the successful loading of the $RuCl_3$ catalyst to the Ni-MOF platform, resulting in the final stage Ru/Ni-MOF electrode.

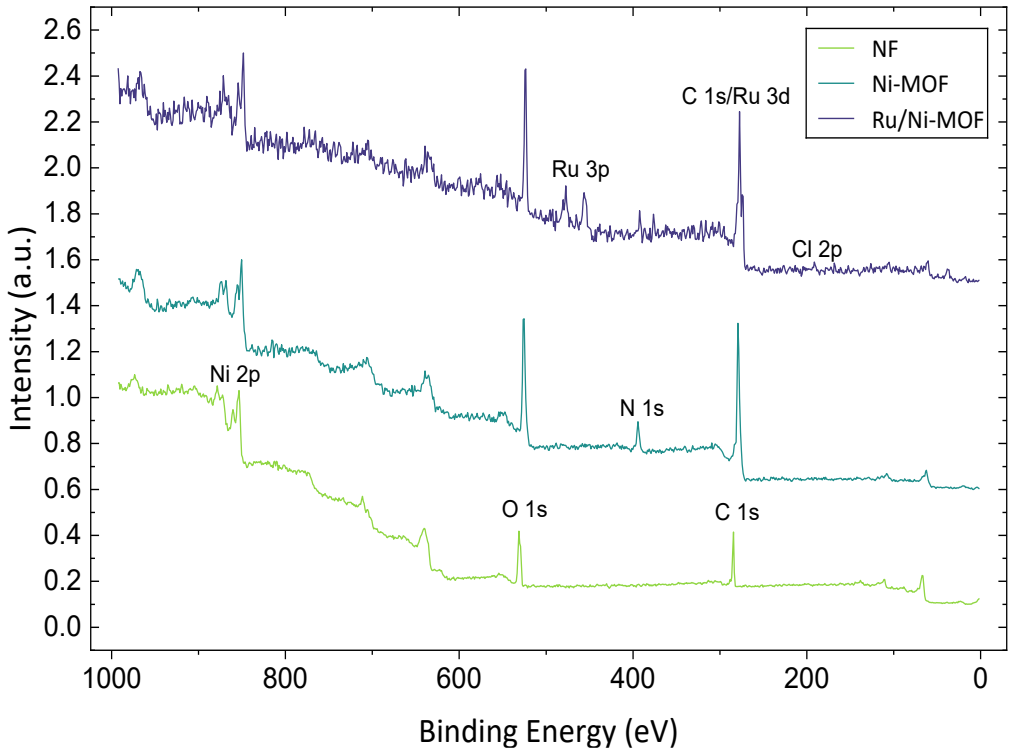


Figure 3.5 Comparison of NF, Ni-MOF and Ru/Ni-MOF survey spectra.

The XPS high resolution spectra in Figure 3.6 demonstrates the overlapping of the C 1s, Ru 3d and K 2p regions that can affect the quantitative analysis of particular electrode stages. The addition of the Ru catalyst is evident by the formation of a peak around 280.1 eV in the Ru/Ni-MOF spectra. Remnants of the KOH solution used during the HER are evident from the presence of K 2p peaks at the higher BE end of the post HER spectrum,

with a less defined Ru $3d_{5/2}$ peak observed at the lower BE end in agreement with the reduction in Ru associated signal detected in the post HER survey in Table 3.1.

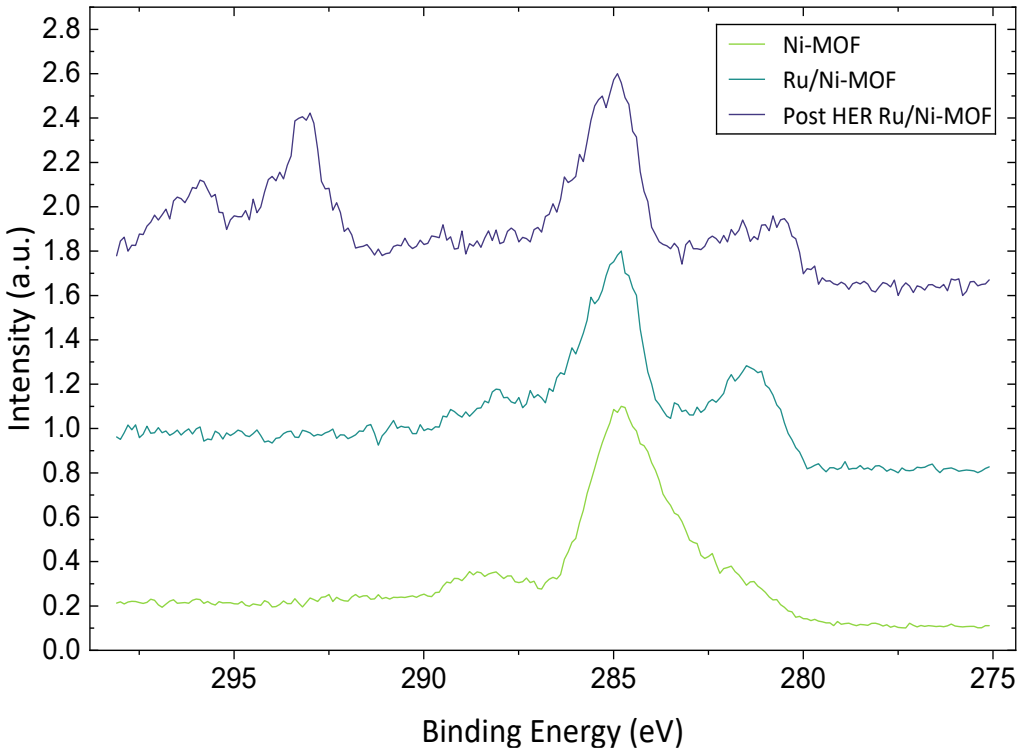


Figure 3.6 High resolution XPS spectra showing overlapping of C 1s, Ru 3d and K 2p regions.

Quantitative analysis of the Ni 2p region is recognised to be complex due to multiplet splitting and the high levels of satellite features which are often confused for higher oxidative states (69). However, the sensible and successful approach to peak fitting developed by Biesinger et al., was utilised in this study to eliminate uncertainties for chemical state analysis of the 2p spectra of first row transition metals such as Ni 2p (70). The asymmetrical trait of the Ni 2p region, large spin-orbit split and tailing towards the higher binding energy side due to shake-up signals gives reasonable justification for solely fitting the $2p_{3/2}$ region in this study.

The high resolution XPS spectra for the Ni 2p region of the NF substrate in Figure 3.7 shows a peak at approximately 853.8 eV. This binding energy in conjunction with the

characteristic strong multiplet splitting of the $2p_{3/2}$ peak suggests the presence of NiO. A native oxide layer was expected on the NF due to exposure to the atmosphere. The shift to a higher binding energy of approximately 855.4 eV and the lesser pronounced multiplet split indicates the growth of a NiLDH layer on the substrate (71). The distinctive lime-green appearance of $Ni(OH)_2$ as shown in Appendix B Figure B1 was also observed upon visual inspection of the sample. The Ni 2p region for the Ni-MOF and Ru/Ni-MOF retained peaks at the same binding energies.

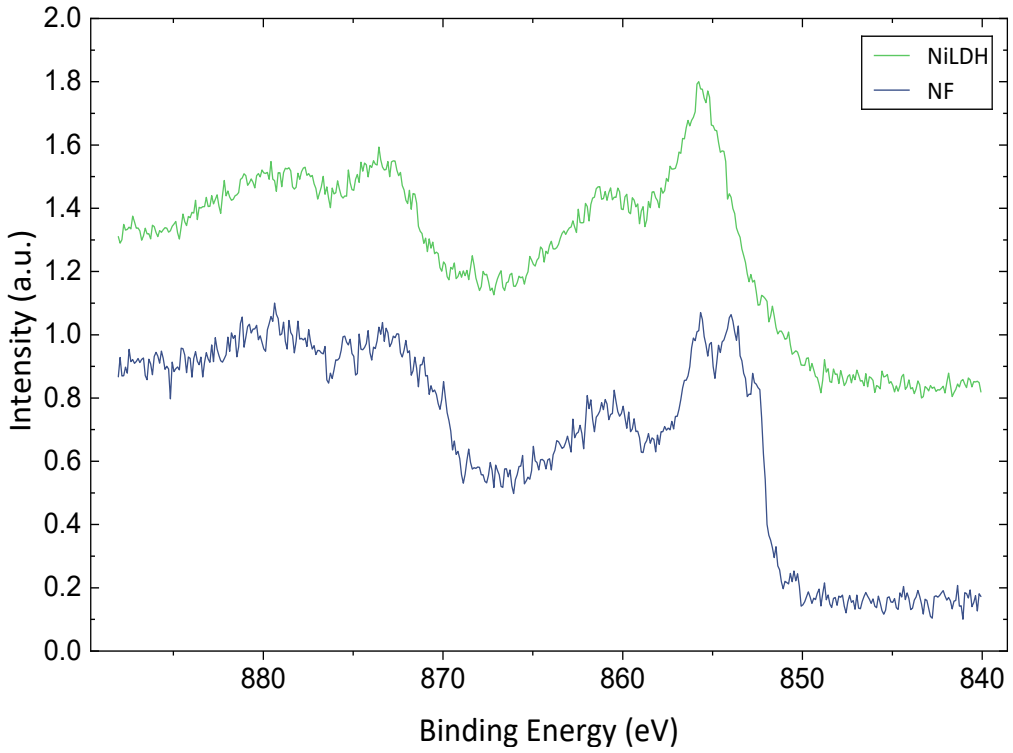


Figure 3.7 High resolution XPS spectra showing the change in the Ni 2p region following the growth of the NiLDH on the NF substrate.

Figure 3.8 contains SEM images of the plain NF substrate before and after the NiLDH layer was developed. NF has a somewhat smooth 3D porous structure affording it a suitable substrate due to its large surface area for catalyst deposition. The images of the NiLDH sample show a textured surface with clusters of particles seen at high resolutions, similarly seen by Li et al., (64). The SEM of the NiLDH supports the conclusion that the higher C_{DL} value in Figure 3.4 is as a result of an increase in surface area of the electrode.

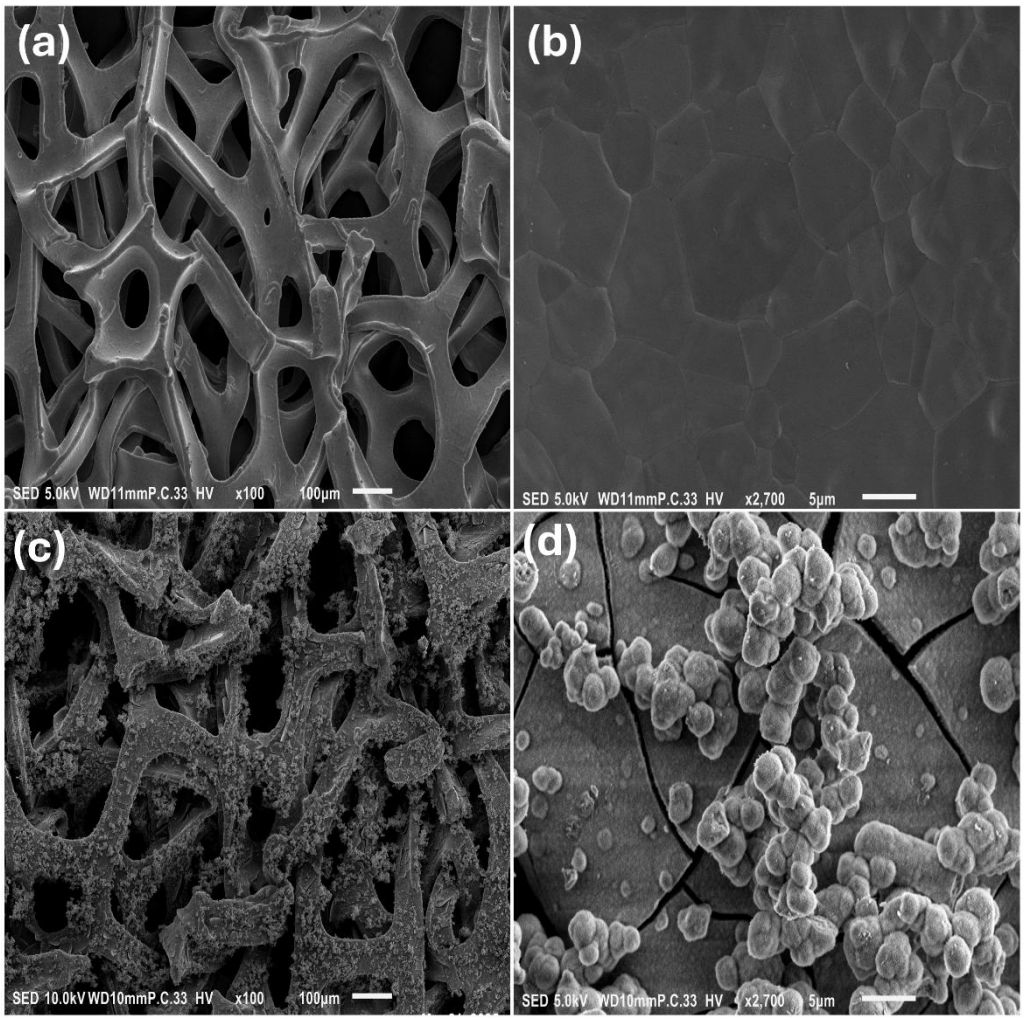


Figure 3.8 SEM images for NF (a & b) and NiLDH (c & d) samples showing growth of the sacrificial metal source layer on the substrate.

The deconvoluted overlapping C 1s and Ru 3d regions and high resolution Ru 3p region for the Ru/Ni-MOF are shown in Figure 3.9 and Figure 3.10, respectively. The Ru $3d_{5/2}$ and $3p_{3/2}$ peaks are positioned at 281 eV and 463 eV, which is in agreement with literature for the presence of hydrated RuO_2 (72). The 3 peaks at approximately 284.8 eV, 285.7 eV and 287.9 eV are recognised as the commonly observed C-C, C-O-C and O-C=O bonds for samples that have been exposed to the atmosphere (73).

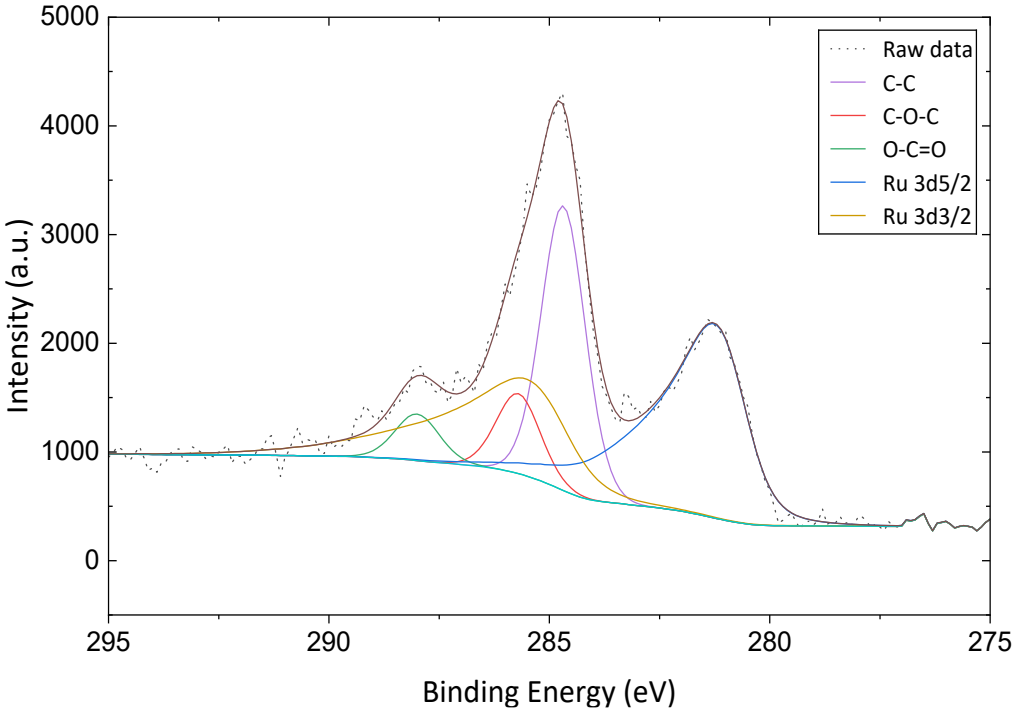


Figure 3.9 Deconvoluted XPS high resolution spectra of the overlapping C 1s and Ru 3d region for the Ru/Ni-MOF sample.

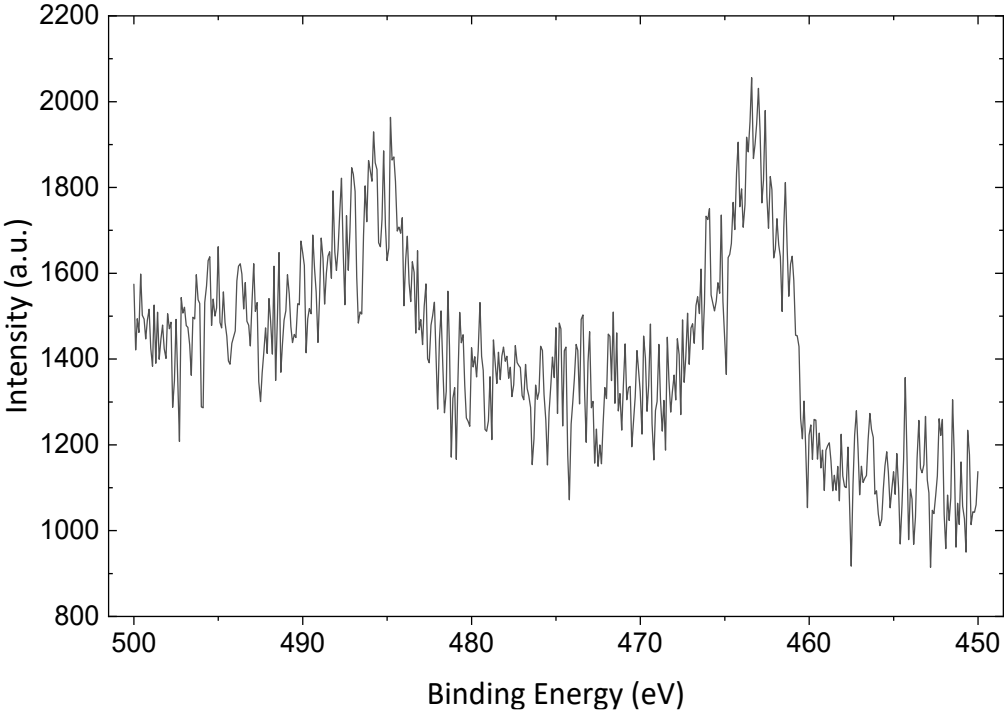


Figure 3.10 XPS high resolution spectra of the Ru 3p region for the Ru/Ni-MOF sample.

The splitting of the O 1s peak in Figure 3.11 for the NF is reflective of the native oxide layer formed on the substrate as a result of oxidation when exposed to the atmosphere. The lower binding energy element is associated with the metal-oxide (M-O) bond, in this

case Ni-O at approximately 529.3 eV, whilst the broader higher binding energy peak is a result of hydroxides (531.3 eV) and organics or absorbed H_2O (532.8 eV). When the NiLDH layer is grown on the substrate, the O 1s peak shifts towards a binding energy of 531.4 eV, indicating the change from NiO to $Ni(OH)_2$ (74). This change is supported by the less prominent multiplet split of the Ni 2p peak. It also transforms to a broader peak shape which remains throughout the following electrode development stages, with the M-O peak becoming slightly more defined once again after the addition of Ru.

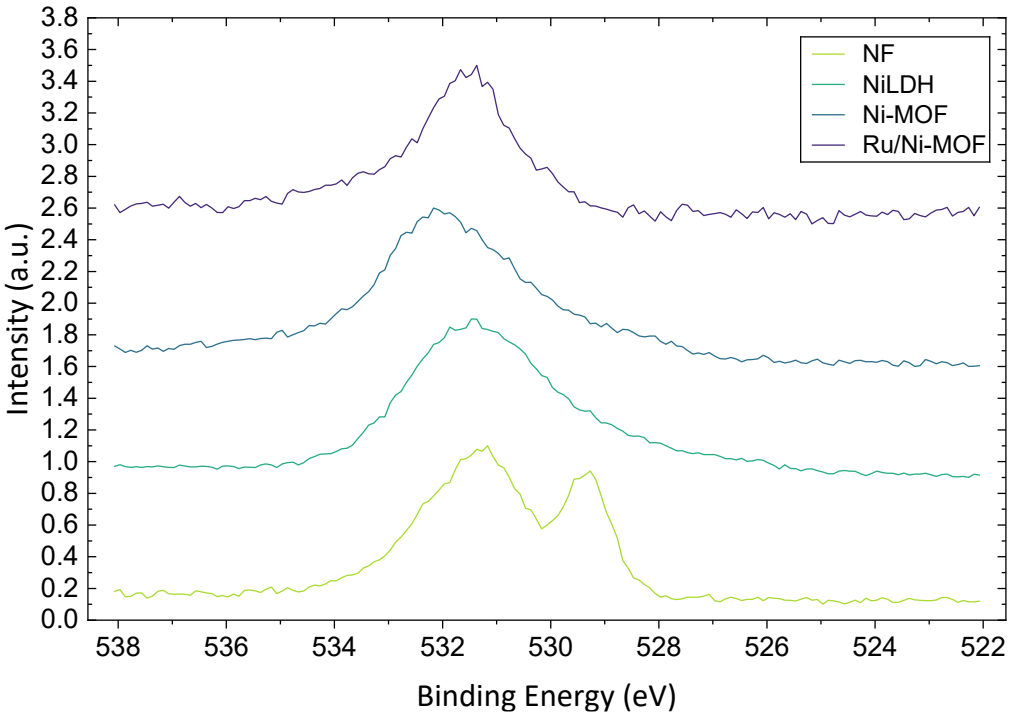


Figure 3.11 XPS high resolution spectra of the O 1s region for the NF, NiLDH, Ni-MOF and Ru/Ni-MOF samples.

The Ru/Ni-MOF shown in Figure 3.12 (a) and (b) covers a substantial percentage of the NF substrate. The catalyst grows as a thick layer on top of the NF, with sections of further sheet-like formations similar to that observed by Sun et al., (63). It is evident that the catalyst structure is significantly altered after a long term HER experiment in Figure 3.12 (c) and (d).

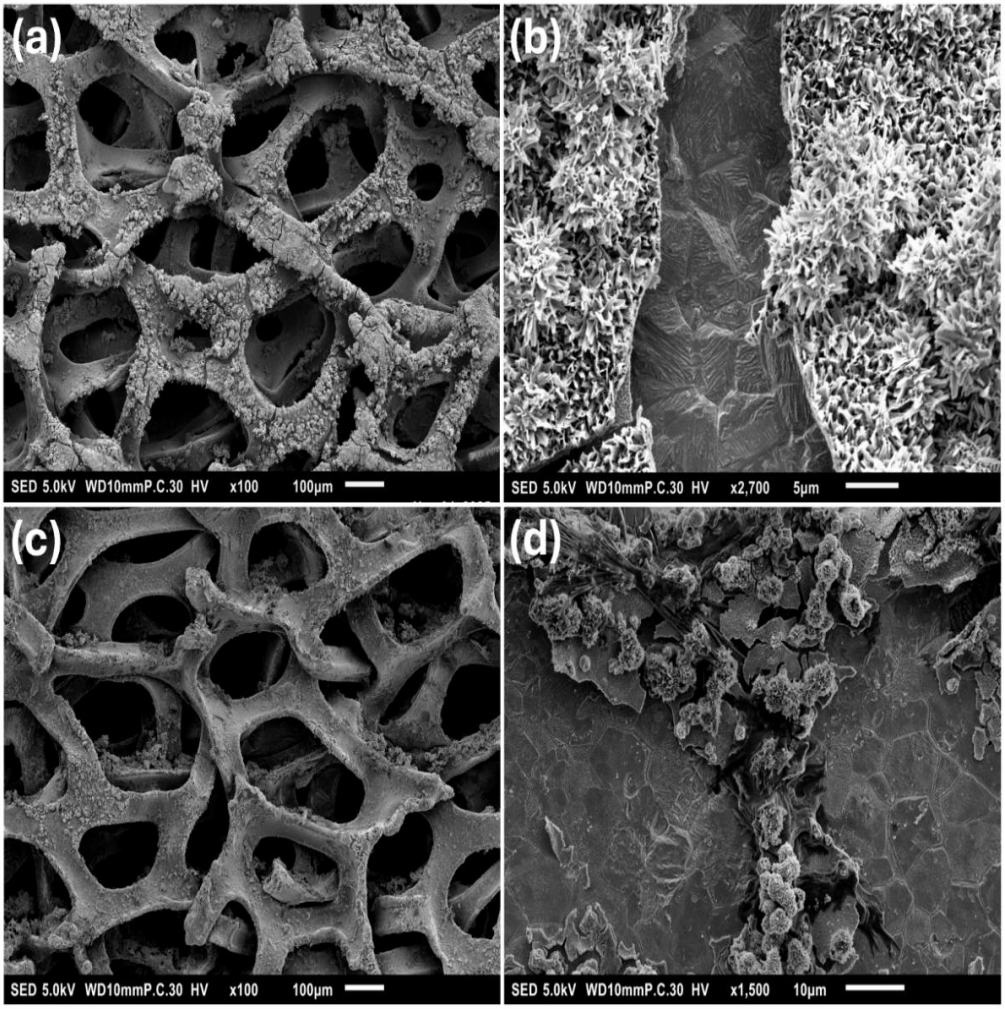


Figure 3.12 SEM of a Ru/Ni-MOF sample pre (a & b) and post (c & d) a long term H_2 production experiment of approximately 200 hours.

The apparent loss in electrocatalytic surface area observed by SEM is reflected by the change in overpotential seen in Figure 3.13 for the Ru/Ni-MOF after long-term stability testing. At 60 mA/cm^2 the overpotential is seen to initially decrease to a minimum of η = 85 mV before an overpotential increase of approximately 84 mV over the next ~70 hours. When the current density was increased to 100 mA/cm^2, a slightly more gradual increase of 47 mV was observed for the next ~130 hours. The constant increase resulting in high overpotential values for the Ru/Ni-MOF during long term operation indicates that the HER catalyst is undergoing continuous degradation which is reducing its efficiency.

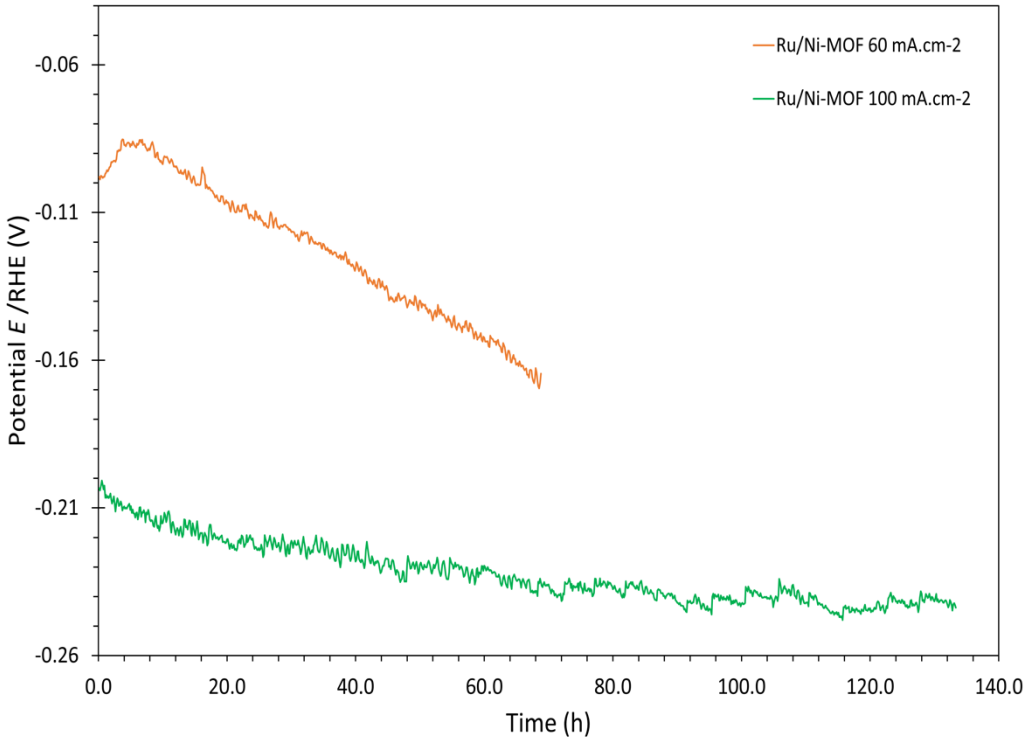


Figure 3.13 Half-cell chronopotentiometry experiments conducted to evaluate the stability of the Ru/Ni-MOF sample at constant current densities of J = 60 mA/cm^2 and 100 mA/cm^2.

The representative SEM images, alongside the observable changes in surface chemistry from the XPS and the electrochemical performance indicate that there is significant degradation of the Ru/Ni-MOF catalyst during hydrogen gas evolution experiments, which could be attributed to different mechanisms of degradation of the electrode. The first is chemical degradation or dissolution of the MOF structure leading to a decline in the porosity of the electrode. As supported by the ECSA and polarisation results, samples with higher porosity and surface area result in superior electrochemical performance. Therefore, if there is dissolution of active sites on the electrolyte surface, this could be the cause for reduced performance. The Ru catalyst itself may also undergo chemical dissolution or mechanical particle detachment, accounting for the reduction in Ru detected by XPS after HER. Due to this observation, the application of a thin TiO_2 protective coating by ALD is investigated in Chapter 5 with the aim of increasing the stability and longevity of the Ru/Ni-MOF electrode.

4. Effect of Plasma Modification on HER Electrode Surfaces

4.1 Introduction

This chapter examines the effect of plasma treatments on the NF substrate and Ru/Ni-MOF electrode. As detailed in Chapter 3, the MOF structure demonstrated a superior performance compared to the NF and NiLDH controls in terms of catalyst retention and overpotential required to achieve a high current density. This is attributed to the high surface area and porosity of the resulting 3D MOF creating additional area for the catalyst to deposit. The ability to perform surface modifications without the use of harsh chemicals or high temperatures affords RF plasma treatments a suitable technique for the sensitive MOF structures. A NH_3-based plasma was chosen to modify the electrode due to its ability to roughen the surface whilst enhancing charge transfer kinetics, therefore increasing the active sites for hydrogen gas evolution to occur. A preliminary study was conducted on the effect of a H_2 plasma on the NF control. If successful at roughening the NF surface, the plasma treatment may have the potential to increase the surface area before catalyst deposition to improve its affinity to the substrate.

4.2 Experimental Procedure

The surface roughening of the samples was conducted using a FlexAL chamber using a ICP 65 inductively coupled plasma (ICP) source. The effect of chamber temperature and length of treatment using NH_3 plasma on surface chemistry, morphology and electrochemical performance was observed for a 0.5 × 1 cm Ru/Ni-MOF and a 0.5 × 1 cm NF control. The chamber was allowed to reach the desired process temperature of either 100°C or 270°C. The samples were then exposed to a 3 or 6 minute plasma process at a pressure of 50 mTorr, 300 W and NH_3 flowed at 50 sccm. A 5 second purge of Ar at

50 sccm and 1 minute of vacuum pumping ended the process. Parameters associated with a typical plasma process are shown in Table 4.1.

Table 4.1: NH_3-based plasma process parameters for recipe conducted at either 100°C or 270°C.

Step	**Time**	**Pressure (mTorr)**	**Ar Flow (sccm)**	**NH_3 flow(sccm)**	**Power(W)**
Vacuum pumping	5 s	0	0	0	0
Pre-heat	3 m	200	20	0	0
Pressure set-up	5 s	50	100	50	0
Plasma gas stabilisation	5 s	50	0	50	0
Plasma	3/6 m	50	0	50	300
Post plasma purge	5 s	80	100	0	0
Vacuum pumping	1 m	0	0	0	0

The samples were XPS scanned pre-plasma and then following 3 and 6 minute plasma treatment. SEM imaging was conducted of the 6 minute treated samples. The overpotential of a 6 minute NH_3 plasma at 100°C was determined by conducting steady state polarisation tests at J = 100 mA/cm^2.

The effect of varying H_2 plasma treatment lengths on a 0.5×1 cm NF was conducted at 100°C. The H_2 plasma process is given in Table 4.2. After pre-heating the chamber, the samples were exposed to a plasma process at a pressure of 50 mTorr, 300 W and H_2 was flowed at 50 sccm. Once again, the chamber and lines were purged for 5 seconds with Ar at 50 sccm and 1 minute of vacuum pumping. XPS was conducted after 5, 10, 15 and 20 minute plasma processes. The 20 minute plasma treated sample was then re-exposed to the atmosphere for 5 and 10 minutes in the load lock before XPS scans were

conducted again. The spectra were analysed using CasaXPS software and fit with Voigt profiles and a Shiley Sherwood type background. An electron flood gun was operated during scans whilst observing the position of the C-C peak at approximately 284.8 eV in the C 1s region. Electrode morphology was observed using a Jeol JSM-IT 100 InTouchScope SEM in SE mode.

Table 4.2: H_2 plasma process parameters for recipe conducted at 100°C.

Step	**Time**	**Pressure (mTorr)**	**Ar Flow (sccm)**	**H_2 flow (sccm)**	**Power (W)**
Vacuum pumping	5 s	0	0	0	0
Pre-heat	3 m	200	20	0	0
Pressure set-up	5 s	50	100	50	0
Plasma gas stabilisation	5 s	50	0	50	0
Plasma	5/10/15/20 m	50	0	50	300
Post plasma purge	5 s	80	100	0	0
Vacuum pumping	1 m	0	0	0	0

4.3 Results

The effect of the NH_3-based plasma on the surface chemistry as determined by XPS survey spectra of the Ru/Ni-MOF and NF at 270°C is presented in Table 4.3. The introduction of N 1s signal to the NF within the first 3 minutes and increase in signal for the Ru/Ni-MOF indicates bonding of N atoms from the plasma to the substrate. The O 1s signal is significantly reduced for the Ru/Ni-MOF compared to that for the NF. The plasma process increases the exposure of the Ru catalyst with time. The plasma treatment reduces the intensity of Cl 2p to an undetectable level by XPS after 3 minutes.

Table 4.3: Surface chemistry of the Ru/Ni-MOF and NF samples at different intervals of NH_3-based plasma treatment at 270°C.

		Atomic %					
Sample	*Time of plasma (m)*	*C 1s*	*O 1s*	*Ni 2p*	*N 1s*	*Ru 3p*	*Cl 2p*
NF	0	46.18	36.04	17.77	-	-	-
	3	35.08	33.06	26.43	5.43	-	-
	6	28.36	38.5	25.65	7.48	-	-
Ru/Ni-MOF	0	53.27	26.59	8.42	-	7.87	3.85
	3	73.47	8.51	4.54	5.36	8.12	-
	6	66.75	6.12	6.45	9.34	11.35	-

The surface chemistry of the NF and Ru/Ni-MOF exposed to a 6 minute 100°C NH_3 plasma is presented in Table 4.4. At this temperature, N was not detected in the survey scan of the NF after 6 minutes, however its presence is confirmed with a small peak in the N 1s region within the high resolution spectrum (Figure 4.2), suggesting that the intensity may have been too low to be detected in the survey. Although the plasma process at this temperature appears less successful at removing surface oxides and contamination on the NF surface than at 270°C, the substantial increase in the Ru 3p signal indicates that it may be the optimal temperature plasma for the Ru/Ni-MOF, with increased exposure of the catalyst after 6 minutes.

Table 4.4: Surface chemistry of the Ru/Ni-MOF and NF samples at different intervals of NH_3-based plasma treatment at 100°C.

		Atomic %					
Sample	*Time of plasma (m)*	*C 1s*	*O 1s*	*Ni 2p*	*N 1s*	*Ru 3p*	*Cl 2p*
NF	0	53.01	36.73	10.26	-	-	-
	6	71.99	23.58	4.43	-	-	-
Ru/Ni-MOF	0	48.98	30.34	8.61	4.98	3.57	3.51
	6	49.06	19.4	4.74	10.94	13.53	2.34

The high resolution XPS spectra of the two process temperatures on the NF are compared in Figure 4.1. For the 270°C process, the ratio of the M-O peak area at the lower BE and the peak attributed to C-O/OH bonds at the higher BE side changes from approximately 1:1 to 2:1 within the first 3 minutes of treatment before stabilising, suggesting a reduction in the amount of absorbed water and carbonate groups. The 100°C process temperature does not appear as successful at exposing more Ni-O/$Ni(OH)_2$ in Figure 4.1 (d) as the ratio of the peaks does not significantly change after 6 minutes of modification. Again, the spectrum in Figure 4.1 (b) suggests a superiority of the 270°C process temperature at increasing the Ni 2p intensity, with higher definition of peaks and satellite features, than that of the 100°C in Figure 4.1 (e). As seen in Table 4.4, the intensity of the C 1s peak in Figure 4.1 (f) increases at 100°C instead of the expected reduction with increasing treatment length such as that observed at 270°C in Figure 4.1 (c).

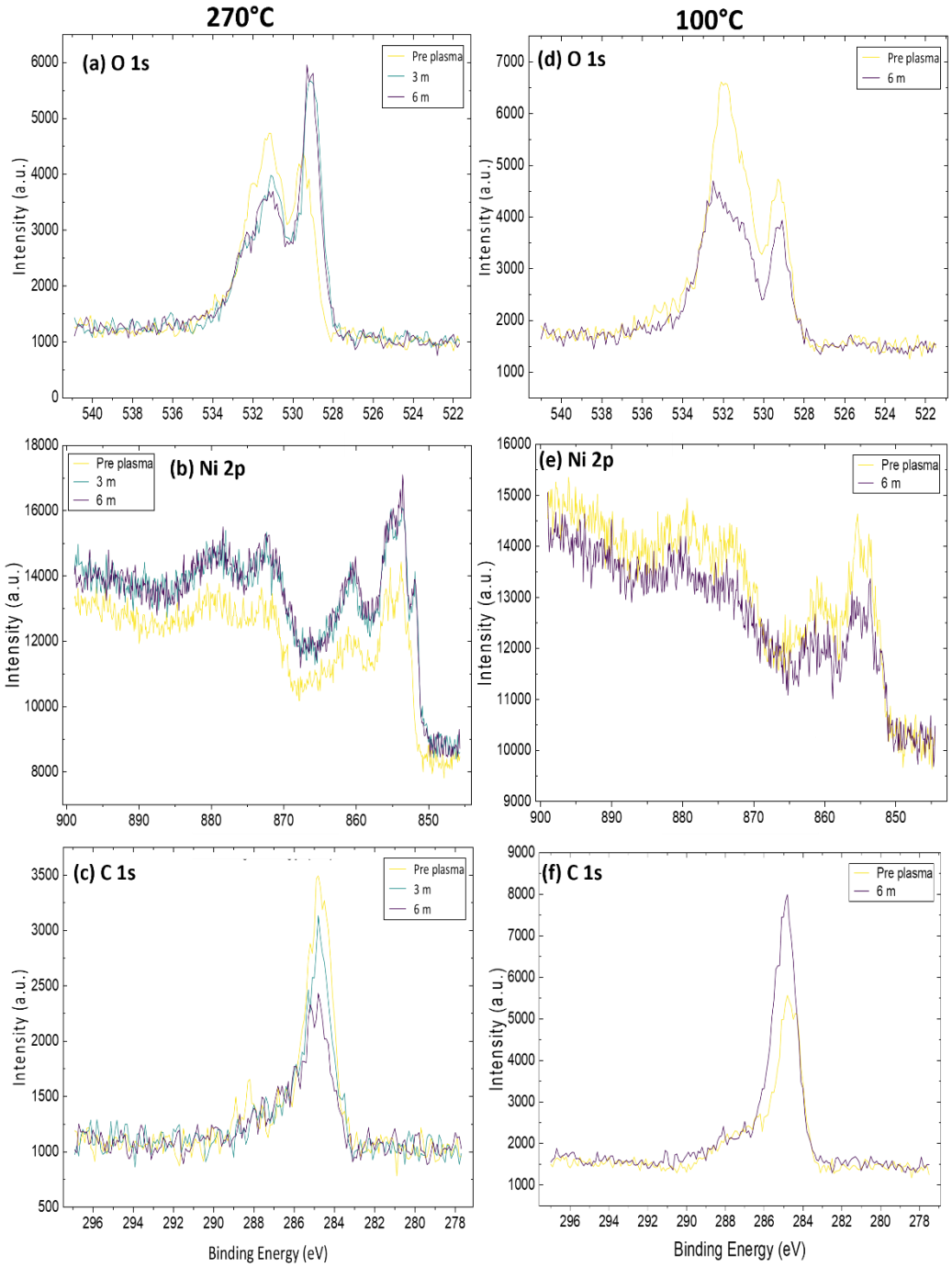


Figure 4.1 High resolution XPS spectra for the NF surface taken during the 270°C and 100°C NH_3-based plasma treatments.

Although the survey spectrum did not detect N 1s signal for the NF sample after the 100°C process, the high resolution spectrum in Figure 4.2 shows evidence of a small N 1s peak after the 6 minutes of treatment. Considering this peak and the increase in N 1s signal for the Ru/Ni-MOF at this temperature in Table 4.2, it is possible to rule out a

failure in the generation of the NH_3-based plasma at 100°C as a reason for the poorer surface modification result as compared to the 270°C process.

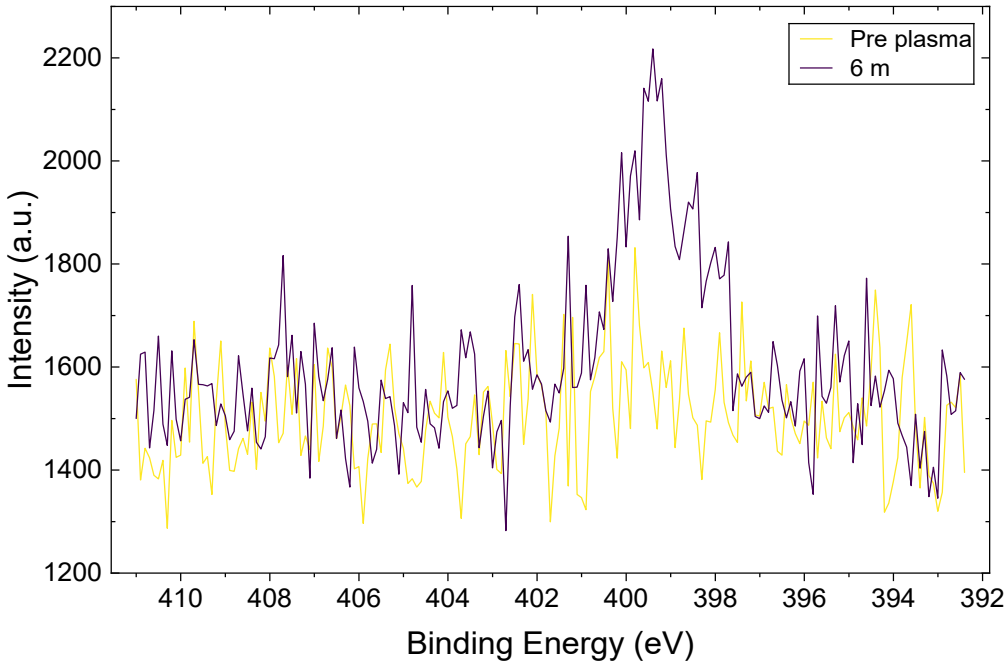


Figure 4.2 XPS high resolution spectrum of the N 1s region showing evidence of signal after a 6 minute NH_3-based plasma of the NF sample despite not being detected in the survey spectrum.

The decrease in intensity of the O 1s peak (Figure 4.3 (a)) coincides with the increase in the Ni 2p signal (Figure 4.3 (b)) for the Ru/Ni-MOF achieved during the 270°C process. As for the NF control sample, the 100°C process temperature did not have a substantial effect on the O 1s content (Figure 4.3 (f)) of the Ru/Ni-MOF and even caused a decrease in the Ni 2p signal (Figure 4.3 (g)), likely due to the increased C 1s signal (Figure 4.3 (h)). The sharp asymmetric peaks observed in Figure 4.3 (c) after the 3 and 6 minutes of plasma treatment are attributed to signal from the Ru $3d_{5/2}$ and Ru $3d_{3/2}$ orbitals, in agreement with the increased intensity of the Ru 3p signal (Figure 4.3 (d)) and percentage detected in the survey scan (Table 4.4). Additional N 1s signal is observed after plasma treatment for both temperatures (Figure 4.3 (e & j), indicating the formation of N containing species on the Ru/Ni-MOF surface as a result of the NH_3-based plasma.

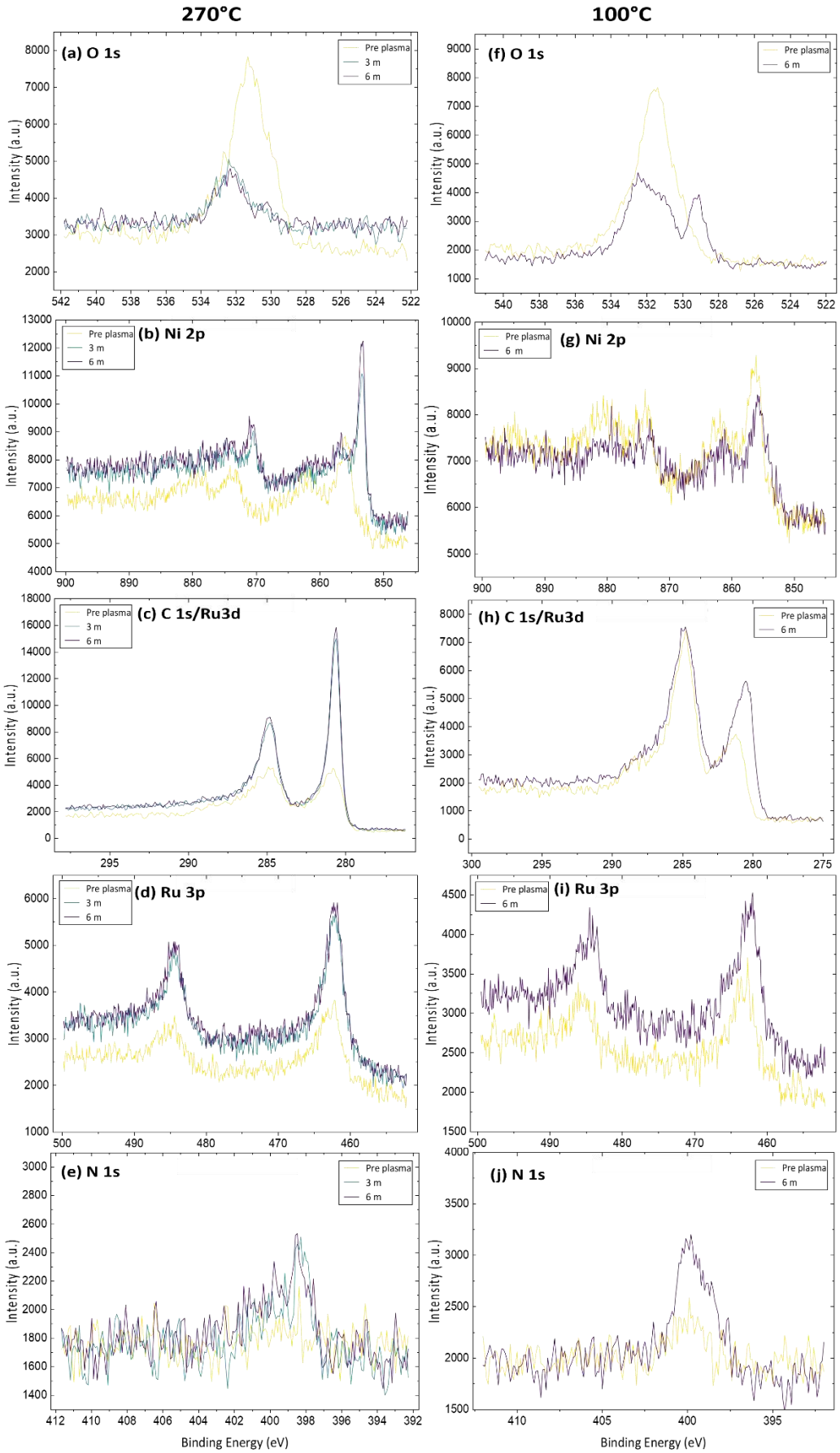


Figure 4.3 XPS High resolution spectra for the Ru/Ni-MOF taken during the 270°C and 100°C NH_3-based plasma treatments.

Despite the higher level of catalyst exposure achieved by the 270°C plasma as demonstrated by XPS and SEM images shown in Figure 4.4, the effect of the 6 minute NH_3 plasma treatment on the electrode and substrate morphology indicates substantial modification to the Ru/Ni-MOF. Figure 4.4 (a) shows how the surface coverage of Ru/Ni-MOF catalyst appears reduced and fractured. At high resolutions (Figure 4.4 (b)) it is evident that large proportions of the catalyst layer have been removed with a textured surface remaining alongside the remnants of the MOF structure. Although the surface of the NF control is not visibly altered at the resolutions in Figure 4.4 (c) and (d), multiple artefacts appear positioned on the surface. Considering these features resemble the Ru/Ni-MOF catalyst layer, it can be assumed that this plasma treatment was too aggressive, causing the catalyst to dislodge and re-deposit onto the NF control, as they both were situated adjacent in the chamber during the process. In regards to the operating temperature of this plasma process, the experiment was repeated at 100°C, with the aim of reducing the destructive effect of the plasma to the Ru/Ni-MOF.

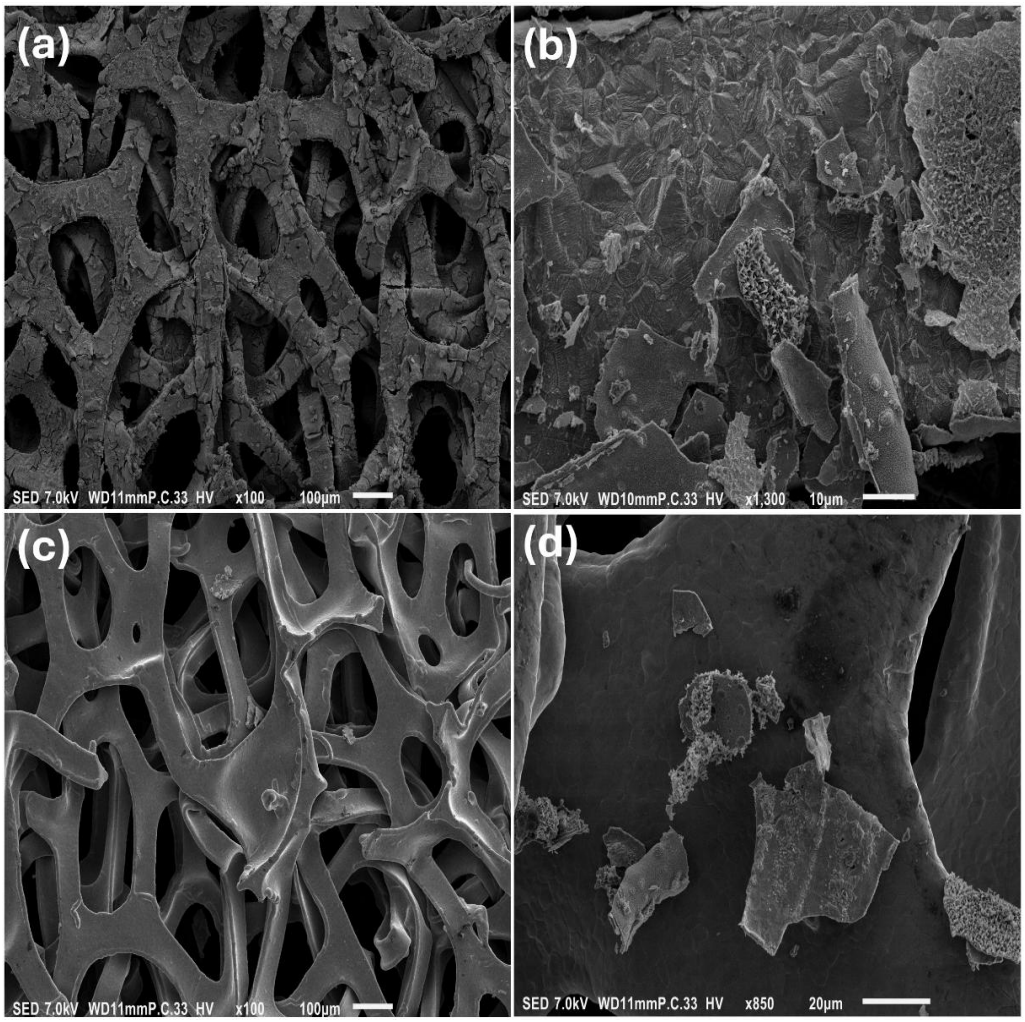


Figure 4.4 SEM images of the Ru-Ni-MOF sample (a & b) and NF control (c & d) after a 6 minute NH_3-based plasma treatment at 270°C.

The SEM images in Figure 4.5 a & b show a somewhat less modified Ru/Ni-MOF layer; however, it is evident that the catalyst layer is still significantly shattered at 100°C chamber temperature. The plasma length and type of discharge gas used could also be contributing factors to the evidential damage of the sensitive MOF catalyst structure.

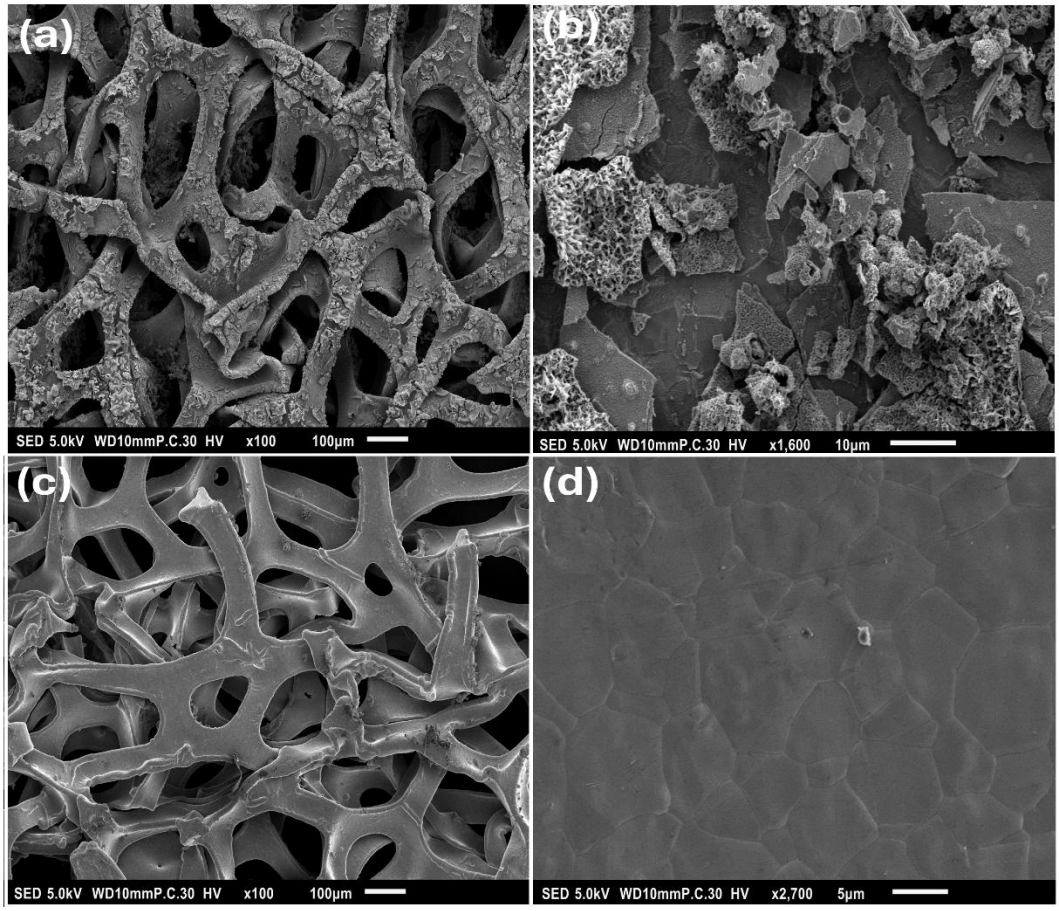


Figure 4.5 SEM images of the Ru/Ni-MOF sample (a & b) and NF control (c & d) after a 6 minute NH_3-based plasma treatment at 100°C.

The steady state polarisation curve in Figure 4.6 shows a decrease in overpotential of around 10-15 mV at J = 100 mA/cm^2 for the Ru/Ni-MOF after a 6 minute NH_3-based plasma treatment at 100°C. Although the decrease in overpotential may be due to an increase in surface area for reactions to occur, this value may also be within the margin of error for this type of experiment, especially considering the inhomogeneous nature of the MOF electrodes. De et al., utilised a NH_3 plasma to achieve both micropatterning and nitridation of Ni electrodes, which resulted in a higher performance than a Pt thin film catalyst commonly used in microfabrication (75). The effect of different combinations of Ar, O_2 and H_2 gas plasmas on Ru/NF electrodes for HER were reported by Liu et al. The study detailed an increase in overpotential at J = 10 mA/cm^2 for a pure Ar and a 95% Ar 5% H_2 plasma, however a decrease in the overpotential for a 95 % Ar

5% O_2 plasma treated electrode tested in alkaline solution (76). The success of plasma treatments at improving the overpotential for poor performing electrodes has been reported in literature; however, the Ru/Ni-MOF used in this study achieved an impressive overpotential of just η = 85 mV at J = 100 mA/cm^2 before any surface modification. Therefore, it may be difficult to achieve a greater decrease in overpotential for this electrode due to the potential saturation point of Ru catalyst performance. However, the 270°C NH_3-based plasma process could be used in future studies to successfully reduce surface contaminants on the NF substrate before deposition to increase catalyst adhesion.

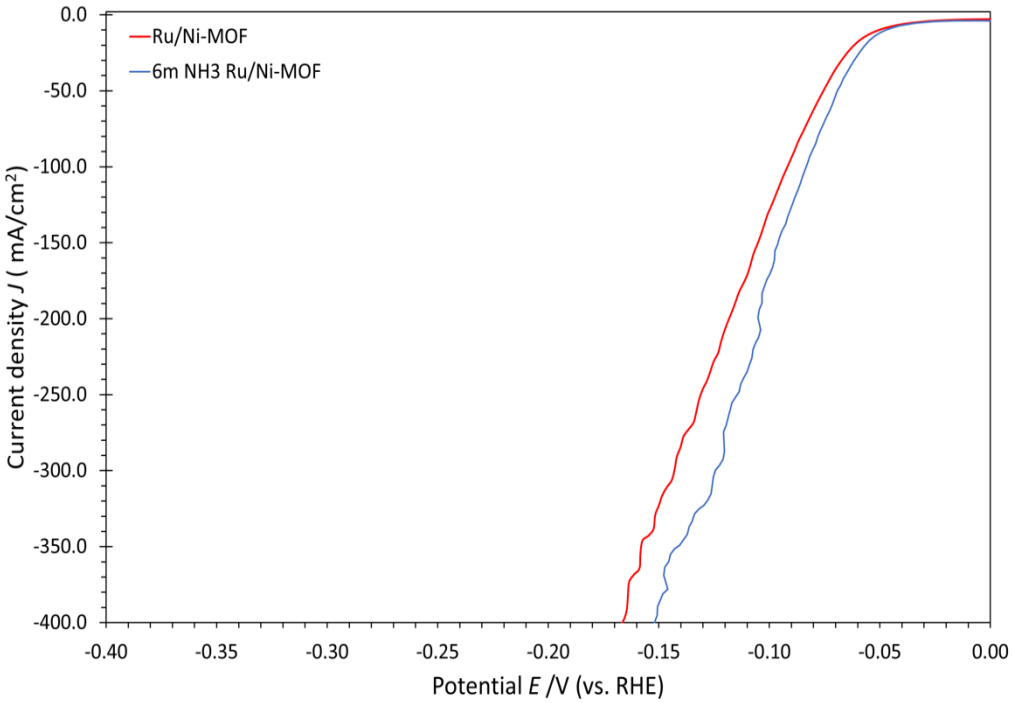


Figure 4.6 Polarisation curve showing the change in overpotential of the Ru/Ni-MOF and 6 m NH_3-based plasma treated Ru/Ni-MOF.

The change in the surface chemistry of the NF obtained from XPS survey spectra sampled at 5 minute H_2 plasma length intervals and after a 5 and 10 minute exposure to the atmosphere (atm) is presented in Table 4.5. The Ni 2p signal almost triples within the first 5 minutes of H_2 plasma modification and continues to rise with increasing treatment time. The increased exposure of the NF substrate is also indicated by the increased

sharpness of the Ni LMM Auger peak around 624.7 eV in the survey spectra of Figure 4.7.

Table 4.5: Surface chemistry of NF at various stages of H_2 plasma treatment and re-exposure to the atmosphere.

	Atomic %		
Length of plasma (m)	*C 1s*	*O 1s*	*Ni 2p*
0	54.66	30.66	14.68
5	30.03	28.86	41.11
10	22.44	20.04	57.52
15	21.69	19.44	58.87
20	21.36	14.81	63.83
20 + 5 m atm exposure	20.99	38.66	40.34
20 + 10 m atm exposure	22.16	39.49	38.35

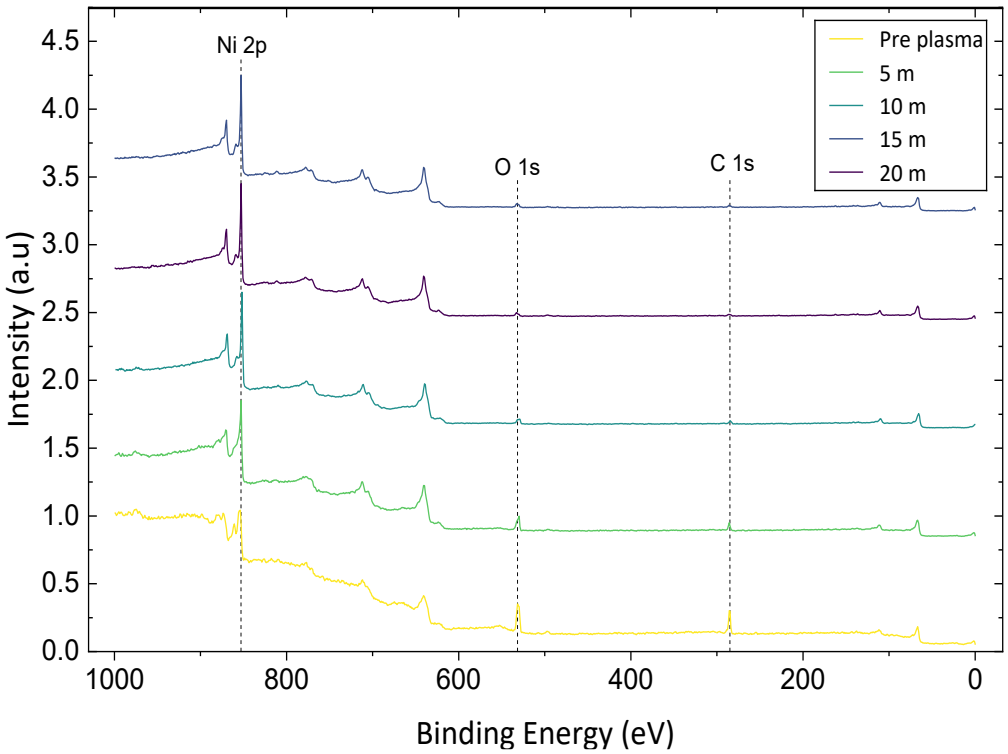


Figure 4.7 XPS survey spectra for different H_2 plasma timed treatments of NF.

The Ni 2p signal in Figure 4.8 (b) assumes a shaper peak shape associated with the formation of metallic Ni(0) over time compared with the distinctive multiple-split shape seen for the untreated NF. This correlates with the reduction in the native oxide layer as observed by the decrease in O 1s signal over time displayed in Table 4.5. The high resolution O 1s spectra in Figure 4.8 (a) shows how the C-O bond peak at the higher BE end decreases dramatically with the detection of C 1s signal shown in Table 4.5 within the first 5 minutes. After 10 minutes the lower BE NiO bond is significantly reduced, with the spectrum becoming increasingly noisy with longer treatment lengths. The reduction in the C 1s signal is attributed to the H_2 plasma removing adventitious carbon from the substrate; however, the reduction stabilises after the first 10 minutes. This is reflected by the C 1s high resolution spectra in Figure 4.8 (c), where the signal to noise ratio is very low after 10 minutes.

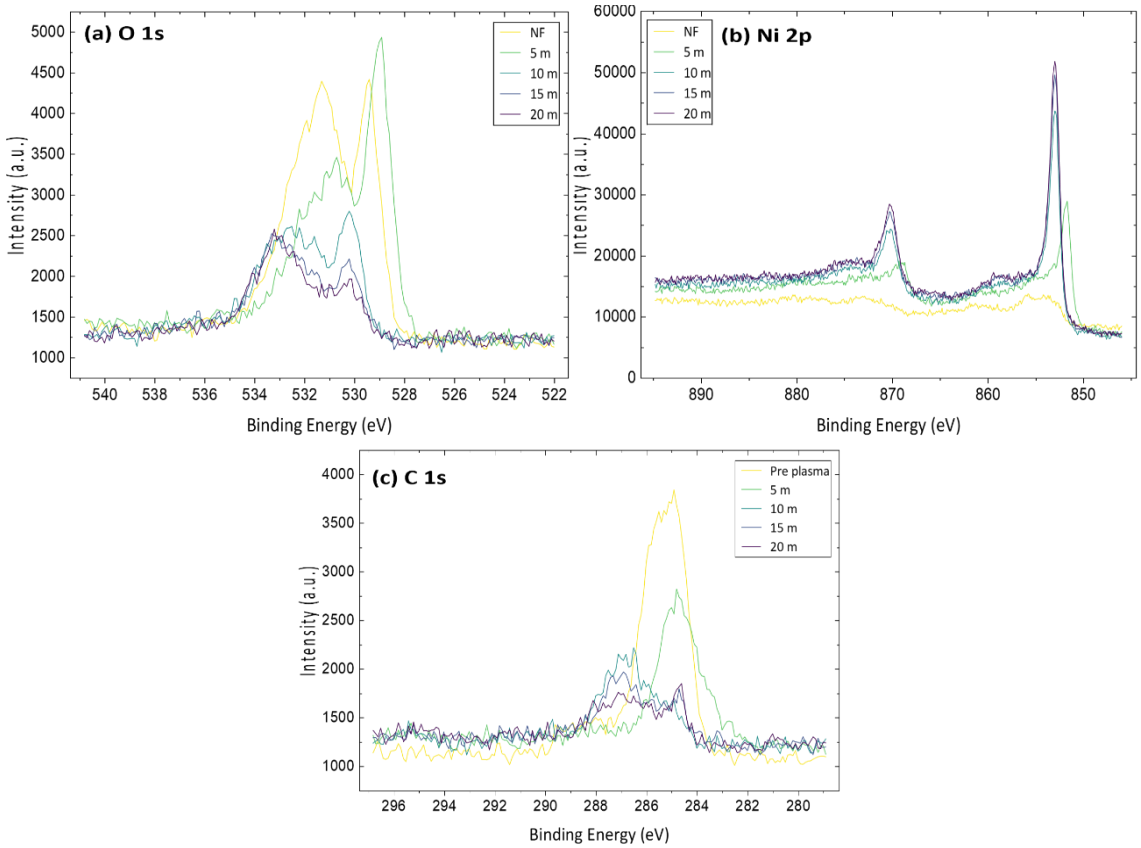


Figure 4.8 (a) O 1s, (b) Ni 2p, and (c) C 1s high resolution XPS spectra for the NF before and after 5, 10, 15 and 20 minute H_2 plasma treatment.

Exposure to the atmosphere results in adventitious carbon deposit and a native oxide layer generation on the surface, making the analysis of the surface chemistry difficult due to the highly surface sensitive nature of XPS. The high resolution spectra in Figure 4.9 shows the importance of in-situ surface modification and characterisation under vacuum with the spectra resembling the pre-treatment data within the first 5 minutes of re-exposure to the atmosphere. The O 1s signal in Table 4.5 quickly increases once again after exposure to the atmosphere indicating the regrowth of the native oxide and suppression of the Ni 2p signal from the substrate.

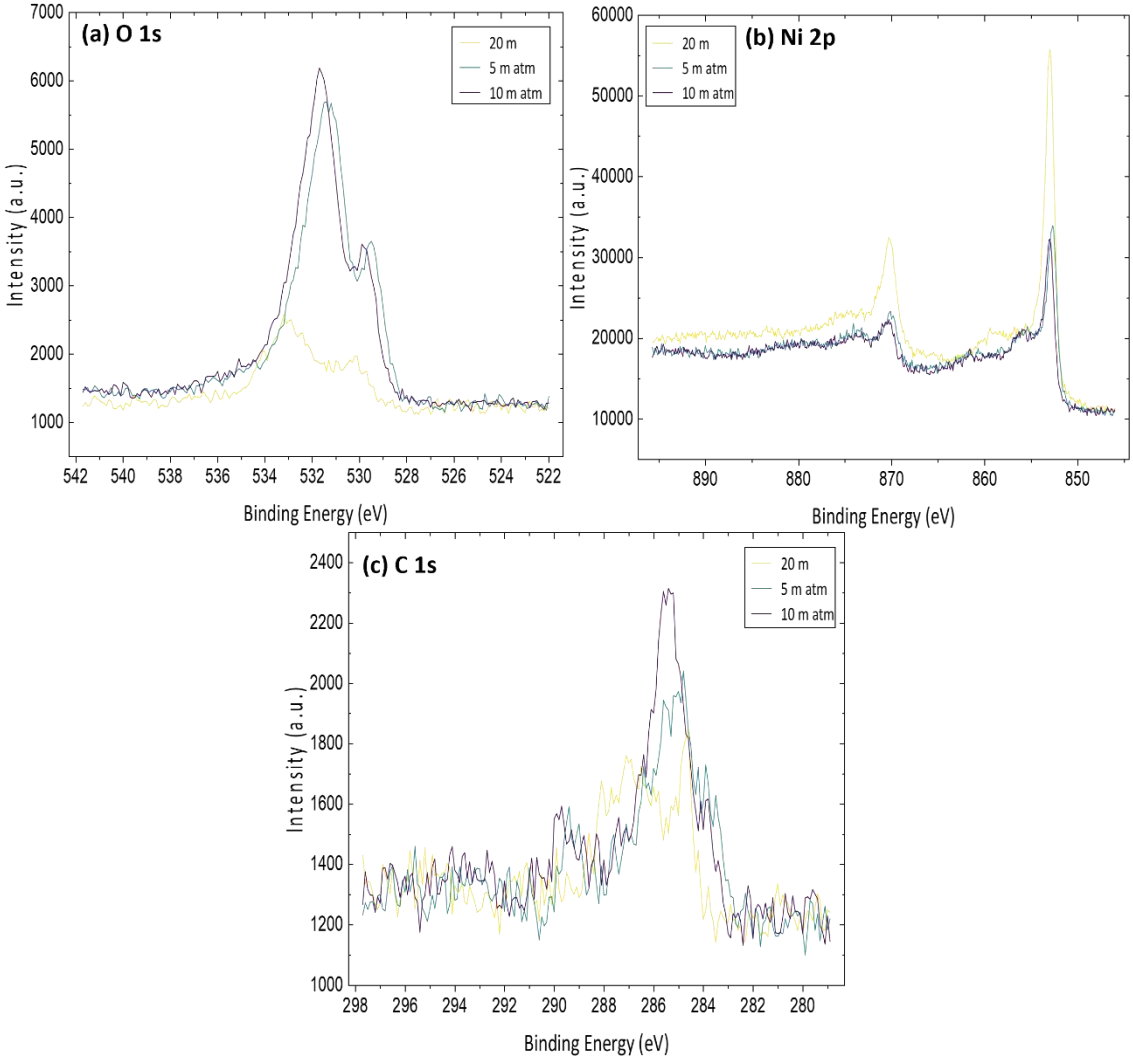


Figure 4.9 (a) O 1s, (b) Ni 2p, and (c) C 1s high resolution XPS spectra of the 20 minute H_2 plasma treated NF after 5 and 10 minute re-exposures to the atmosphere.

It is evident that levels of modification can be made to the surface of the Ru/Ni-MOF sample and NF control using different RF generated plasmas at varying lengths of times and temperatures. The results of the NH_3-based plasma experiments show that whilst the 270°C temperature appears excessively destructive for the Ru/Ni-MOF, it has a potential use in the pre-treatment of the NF substrate to remove surface oxides with the aim of increasing catalyst adhesion. The 100°C experiment was somewhat less damaging to the Ru/Ni-MOF and resulted in a decrease in the overpotential, which may be due to an increase in the surface area for catalytic activity. H_2 plasma treatment of the NF exhibited the successful exposure of the substrate surface after minimal treatment time and therefore could has potential in the modification of the Ru/Ni-MOF to increase catalyst exposure. The rapid regrowth of the native oxide layer on the NF following re-exposure to the atmosphere successfully demonstrated the role of in-situ plasma treatment and XPS characterisation.

5. PEALD of TiO_2 Protective Coatings for HER Electrode

5.1 Introduction

The notable change in surface chemistry, morphology, and performance of the Ru/Ni-MOF after hydrogen evolution observed in Chapter 3 suggests that there are areas for improvement with respect to catalyst stability and longevity. Degradation occurs as a result of the interaction between the intrinsic properties of the catalyst and environmental factors such as the pH, the presence of oxygen, the applied potential or current, pressure and temperature. Although a catalyst is defined as a molecule or material that speeds up the rate of reaction without being consumed during the process, there are numerous mechanisms in which electrochemical catalysts can be deactivated (77). Dissolution of the catalyst or substrate material results in the loss of active sites to the electrolyte solution, with the possibility of redeposition of the removed material in an alternative part of the electrode. The active catalyst surface area can become blocked due to impurities from the electrolyte solution and the gaseous products which have failed to release. Particle detachment and agglomeration has been associated with a reduced support-catalyst interaction. There are many routes to diminishing the degradation of catalysts in electrochemical applications. Using decreased nanoparticle loadings is suggested to reduce agglomerations due to increased distances between particles (78). The utilisation of a pore structure such as a MOF leads to lower levels of agglomerations in the embedded particles than for those situated on the outer surface. Alloying with noble and non-noble metals can lower the dissolution of the catalyst, whilst functionalisation of supports may increase corrosion resistance (79).

The technique that is investigated in this chapter is the encapsulation of the electrocatalyst in a thin semipermeable layer by ALD. Introducing a protective coating increases the distance between the sensitive catalyst and the site of the HER, with the aim of reducing the deteriorative effects of the H_2 production on the catalyst platform. Thin coatings of TiO_2 have been reported to reduce the agglomeration and detachment of Pt particles (80) and are investigated below for the effect on the current density and stability of the Ru/Ni-MOF. ALD is a highly suitable deposition technique for uniform films on complex substrates such as MOFs. This chapter reports the effect of depositing thin layers of TiO_2 onto the Ru/Ni-MOF, and studying the surface chemistry, morphology, and electrochemical performance, specifically in long-term H_2 production.

5.2 Experimental Procedure

The deposition of thin films of TiO_2 was conducted and monitored using the integrated Oxford Instruments FlexAL II ALD Reactor and Scienta Omicron XPS with a 128 channel Argus CU detector. The protective coatings were deposited on two types of samples, a 0.5 × 1 cm Ru/Ni-MOF and a 0.5 × 1 cm NF control. The control was included so that the development of the Ti 2p region could be assessed by XPS without overlap from the Ru 3p region that occurs for the Ru/Ni-MOF, and to observe suppression of any Ni oxidation peaks in characterisation CVs. All samples were exposed to atmosphere before processing and therefore contain some level of adventitious carbon.

Tetrakis(dimethylamino)titanium(IV) (TDMAT, Strem Chemicals 99.99%) (Figure 5.1), O_2 and Ar were used as the precursors, co-reactant and inert gas respectively. The bottle temperature was set at 75°C based on the reporting of high quality TiO_2 films at low bottle temperatures by Avila et al., and Hannula et al., (81,82). The sample was

preheated to 200°C with an Ar gas flow of 50 standard cubic centimetres per minute (sccm). The lowest possible temperature within the manufacturer's suggested temperature range for successful deposition was chosen to reduce the risk of thermal decomposition of the electrocatalytic surface**.** The results were monitored for residual N to ensure full breakdown of the precursor molecule was occurring at 200°C**.** Purge flows occurred using Ar gas at 100 sccm. Once the chamber was heated, the TDMAT precursor was dosed for 0.5 s, followed by a purge of 5 s to remove any remaining particles from the ALD chamber. The O_2 co-reactant was then stabilised for 2 s before the plasma was ignited using 300 W power for 4 s. Lastly, the co-reactant was purged from the chamber for 2 s, and the recipe was repeated for the desired number of cycles. The samples were transferred in vacuum pressure to the XPS so that the deposition process could be monitored in real time to avoid atmospheric contamination of the films.

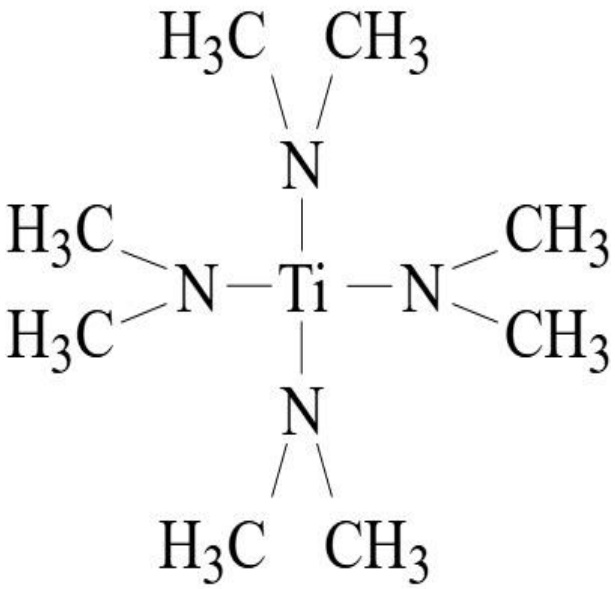


Figure 5.1 Structure of Tetrakis(dimethylamino) titanium (TDMAT) precursor molecule.

The surface chemistry of the samples was monitored pre-deposition and at 10 cycle intervals up to a total of 50 cycles using XPS. Step sizes of 1 and 0.1 eV were used for the

survey scan and high-resolution spectra at normal emission, respectively. CasaXPS software was used to analyse the spectra with Shirley - Sherwood type background. Voigt functions used to fit high resolution spectra and photoemission peaks were corrected according to the hydrocarbon signal in the C 1s region at 284.8 eV. An electron flood gun was turned on during each XPS scan to neutralise any sample charging whilst monitoring the adventitious carbon peak in the C 1s region. SEM imaging of the Ru/Ni-MOF and NF control was carried out before and after 50 cycles of ALD were conducted.

Ni characterisation CVs were conducted for the bare NF and for TiO_2 coated NF after 10, 20, 30, 40 and 50 ALD cycles. A 50 cycle coated sample was characterised before and after measuring a HER polarisation curve. Steady state polarisation experiments were conducted for 2 mg/cm^3 and 3.5 mg/cm^3 Ru/Ni-MOF samples before and after 50 ALD cycles. The 50 ALD cycle coated Ru/Ni-MOF and NF were subject to long term H_2 production experiments in 1 M KOH at current densities of J = 60 mA/cm^2 and 100 ma/cm^2 over a total of 130 hours.

5.3 Results

The Ni 2p, C 1s and Ru 3d regions of a Ru/Ni-MOF sample were observed for signal attenuation as a function of the increasing cycle numbers. As the thickness of the protective coating increases, the intensity of the signal from the substrate should decrease. The Ti 2p and O 1s regions were monitored for the development of TiO_2. Table 5.1 displays the change in surface chemistry of the Ru/Ni-MOF sample from pre-deposition to post 50 ALD TiO_2 cycles monitored using the survey spectra. Ti 2p signal is detected within the first ten cycles along with complete suppression of the Ru 3p signal, indicating rapid early-stage surface coverage. Detection of the N 1s and Ni 2p signals

cease after the 30th cycle, with the N present at low cycle numbers attributed to that which pre-exists in the Ru/Ni-MOF structure, rather than a byproduct of the TDMAT molecule.

Table 5.1: Percent of elements at 10 cycles of TiO_2 ALD intervals for a Ru/Ni-MOF sample.

	Atomic %					
Number of ALD cycles	*C 1s*	*O 1s*	*Ni 2p*	*N 1s*	*Ru 3p*	*Ti 2p*
0	51.61	29.11	8.23	4.46	6.59	-
10	38.12	44.34	4.24	4.21	-	9.09
20	27.1	47.68	3.77	4.17	-	17.29
30	20.52	57.98	-	-	-	21.5
40	10.87	64.66	-	-	-	24.48
50	9.78	62.51	-	-	-	27.71

The full dissociation of the TDMAT molecule can be concluded from the survey spectra of a NF control sample in Figure 5.2, which shows no N signal at 400 eV. The C 1s signal is not fully lost after the 50th cycle; however, continues to decrease as a function of the number of cycles. This supports the theory that the TDMAT molecule is fully dissociating and that the C signal is not a result of ligand incorporation and is potentially due to its relatively high XPS sensitivity, considering C is present in high concentrations in the starting substrate. The Ti:O ratio achieved by the 50th cycle is in good agreement with the stoichiometric literature values of a 1:2 composition (83).

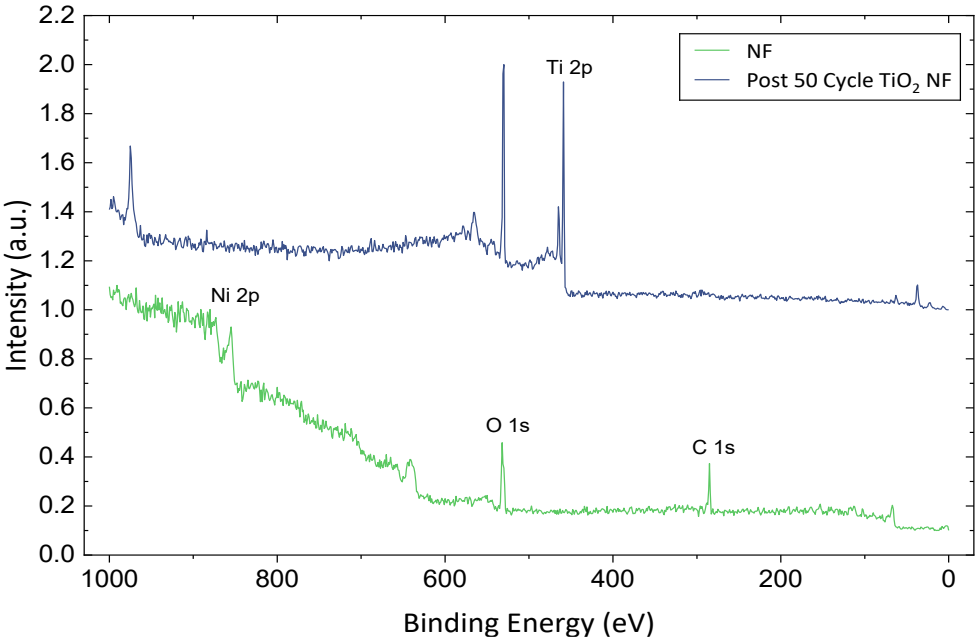


Figure 5.2 Survey Spectra of NF control pre and post 50 ALD TiO_2 cycles.

The C1s/Ru 3d, Ni 2p and O 1s high resolution spectra of the Ru/Ni-MOF sampled throughout the ALD process are displayed in Figure 5.3, along with the Ti 2p region of the NF control. The NF control was used to monitor the development of Ti 2p due to the overlap of the region with the Ru 3p causing inaccuracies in quantitative analysis for the Ru/Ni-MOF. In Figure 5.3 (a) and (b) the attenuation of the Ni 2p, C 1s and Ru 3d regions as a function of increasing ALD cycles is observed with a concurrent increase in the intensity of the O 1s (Figure 5.3 (c)) and Ti 2p (Figure 5.3 (d)) regions. The peaks relating to the C 1s region experience a broadening at the higher BE end with increasing cycles due to the increase in C-O bonds and becomes too noisy for accurate peak fitting by the 40th cycle. The Ni 2p region becomes significantly noisy by the 20th cycle and is completely supressed by the 30th cycle. The growth of O 1s signal as a function of increasing cycle number is seen in Figure 5.3 (c). The O 1s peak of the Ru/Ni-MOF can be deconvoluted into two peaks associated with metal hydroxides (531.7 eV) and C-O bonds (533.7 eV). These bonds contribute to a small peak seen at the higher binding energy end of the O 1s peak for the increasing cycle numbers. The emergence of the

TiO_2 peak at 530.5 eV is observed after 10 cycles and increases in intensity with the number of cycles. The Ti 2p region in Figure 5.3 (d) supports the conclusion that TiO_2 is growing effectively within the first 10 cycles due to the Ti $2p_{3/2}$ and $2p_{1/2}$ peaks at 458.75 eV and 464.5 eV respectively, commonly associated with Ti^{4+} (84). There are no peaks associated with the growth of metallic Ti (453.7 eV) seen at any stage of the ALD process.

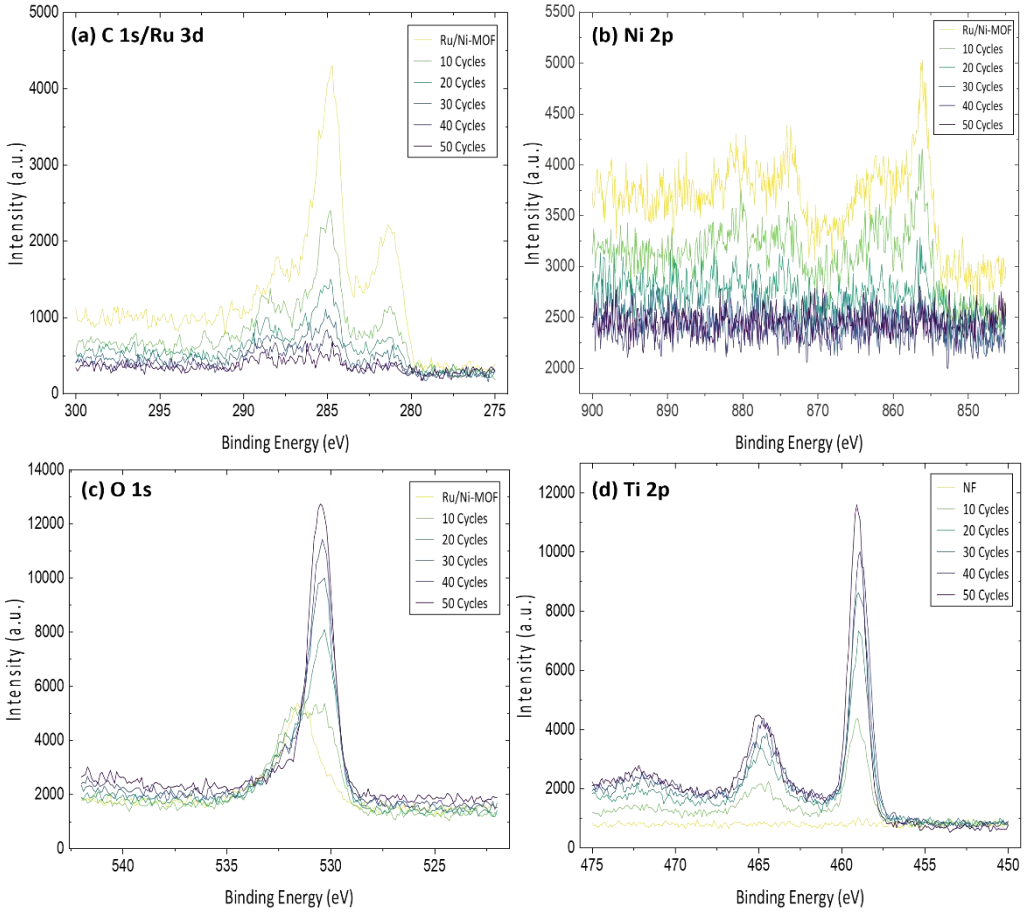


Figure 5.3 XPS high resolution spectra evolution as a function of increasing ALD TiO_2 cycles of the (a) C 1s/Ru 3d, (b) Ni 2p and (c) O 1s regions for the Ru/Ni-MOF and (d) Ti 2p region of the NF control.

The effect of the TiO_2 ALD on the NF was determined by comparing the characterisation CVs of 6 separate samples that had undergone either 0, 10, 20, 30, 40 or 50 cycles of ALD, and also the 50 cycle ALD coated sample post HER. It is clear in the NF CV characterisation shown in Figure 5.4 that the charge associated with the oxidation of the Ni(II) to Ni(III) is significantly suppressed after ALD of the TiO_2 film indicating that the Ni

surface is substantially separated from the electrolyte solution at this potential. The suppression of the NF peak appears to increase only slightly with the number of cycles, which is justifiable as the thickness of the layer after 50 cycles and 10 cycles likely varies by just a few nm. When comparing the curves of the 50 cycle coated NF sample that was tested pre (blue) and post (red) HER, it can be assumed that the TiO_2 coating may have been partially removed during active hydrogen evolution, due to return of the peak shape towards the bare NF profile.

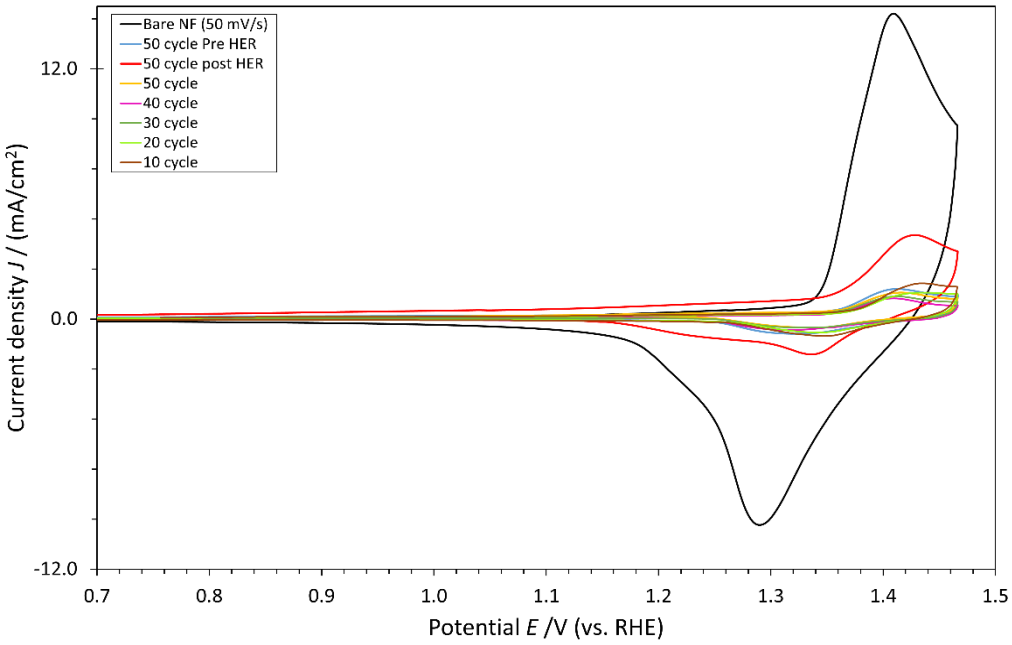


Figure 5.4 Characterisation CVs for NF control samples before and after TiO_2 ALD coating and post HER.

The polarisation curve in Figure 5.5 of the NF control after 50 ALD cycles of TiO_2 shows reduced performance compared to the bare NF, in agreement with the heavy suppression of the Ni peak in Figure 5.4. Two *J-E* curves are presented in this graph for two separate bare Ru/Ni-MOF samples labelled S1 (red) and S2 (green). For S2, there are two data sets for the 50 cycle TiO_2 version. The blue curve represents the same piece of sample that was used in a long term stability test (Figure 5.6) and therefore the negative potential extent was deliberately limited to avoid damaging the coating prior to conducting longevity testing. The blue curve suggests that the overpotential of the

coated sample increases with the addition of the coating once the current surpasses J = -25 mA/cm^2. However, a contradictory result of a superior overpotential was achieved for this sample in the long-term stability test (Figure 5.6). The yellow curve in Figure 5.5 also implies a superior overpotential for a different section of the same coated sample compared to both S1 and S2 uncoated Ru/Ni-MOF.

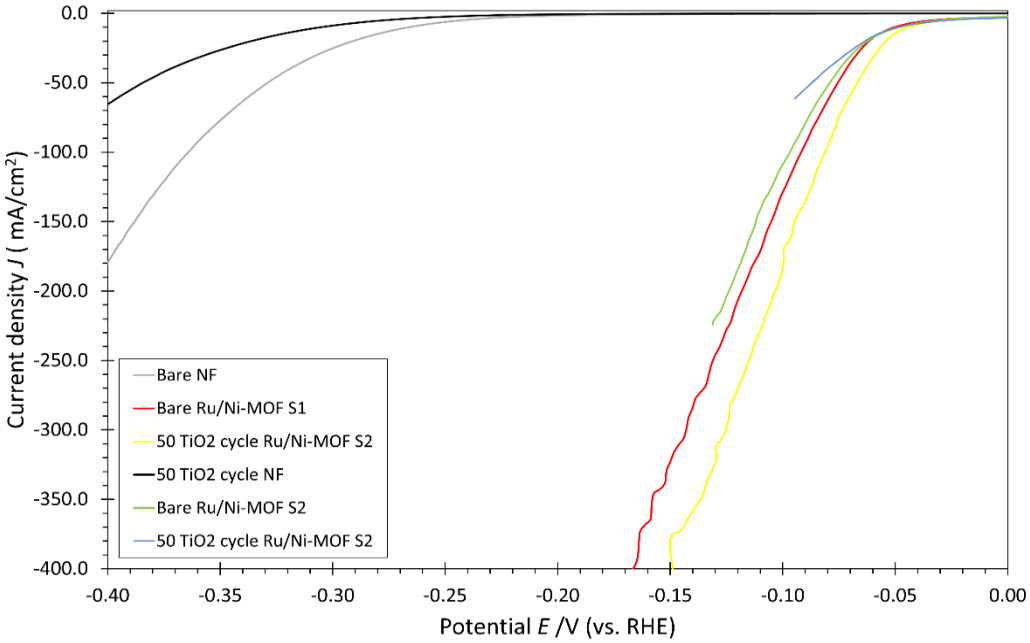


Figure 5.5 Polarisation curves for 2 mg/cm^3 Ru/Ni-MOF and NF before and after 50 cycles of TiO_2 ALD.

The long-term stability test of the Ru/Ni-MOF electrode as described in Chapter 3 was repeated for the 50 cycle TiO_2 ALD coated sample as displayed in Figure 5.6. As bare NF typically requires a potential in the order of -0.5 V to achieve a current density of 100 mA/cm^2, the operation of the samples at potentials more positive than -0.24 V suggests a level of retainment of Ru after the long-term tests. However, it appears as though the variation in the overpotential over time for the coated and uncoated samples is highly similar, hence suggesting that the 50 cycle TiO_2 coating of the Ru/Ni-MOF did not particularly improve its longevity during HER. The suppression of the Ni(II)Ni(III) peak for the NF in Figure 5.4 and reduction in its HER performance in contrast to the lack of clear

impact of the coating on the performance and stability of the Ru/Ni-MOF could imply that the TiO_2 coating had different affinities towards the two surfaces. Although the versatility of ALD for 3D structured samples has been demonstrated for efficient water splitting, it has also been reported that ALD modifications on samples with higher specific surfaces areas can suffer from agglomeration problems and lower efficiency than for that on planar substrates (85,86). The higher surface area of the Ru/Ni-MOF compared to the NF could have reduced the adhesion of the coating to the substrate. H_2 plasma modifications have been used to improve surface hydroxyls on substrate surfaces before the deposition of TiO_2 coatings to improve nucleation (56). The level of absorbed H_2O and organics on the Ru/Ni-MOF is potentially greater than for the NF due to the hydrated RuO_2, resulting in a lower level of hydroxyls, which could be a further cause for the variation in affinity.

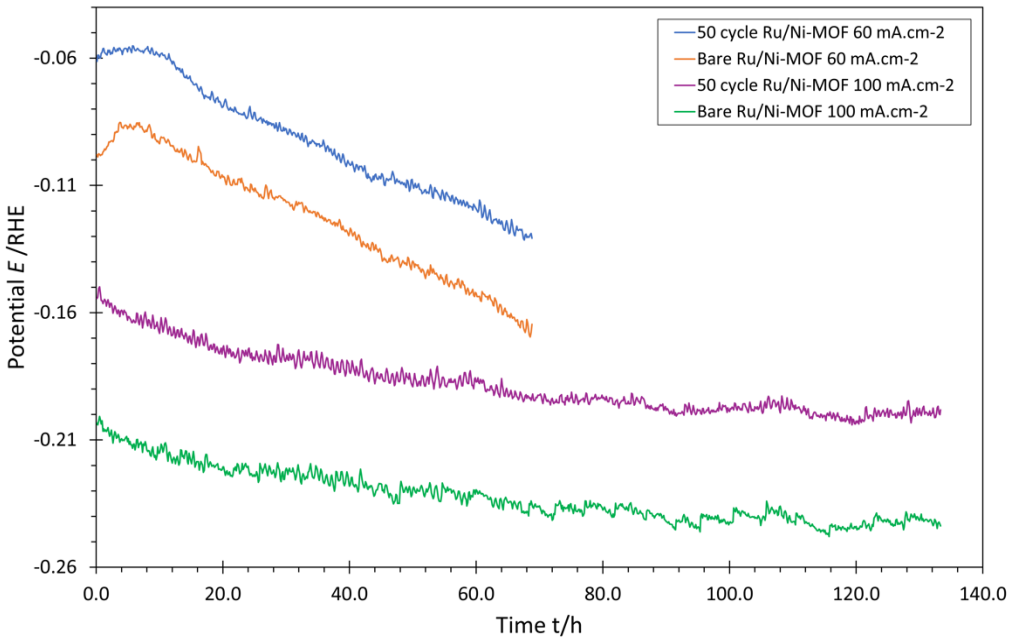


Figure 5.6 Chronopotentiometry experiments conducted to test the stability of the Ru/Ni-MOF electrode before and after 50 cycles of TiO_2 ALD at J = 60mA/cm^2 and 100 mA/cm^2. Bare Ru/Ni-MOF data was previously presented in Figure 3.13.

A similar experiment conducted for a 3.5 mg/cm^3 loaded Ru/Ni-MOF also suggests that the coated sample has a superior curve than the uncoated (Figure 5.7). It is difficult to

be conclusive with regards to the effect of the 50 cycle TiO_2 coating on the HER *J-E* curve for the Ru/Ni-MOF on the basis of this data; however, it could be suggested that the coating does not particularly alter the curve in a negative way.

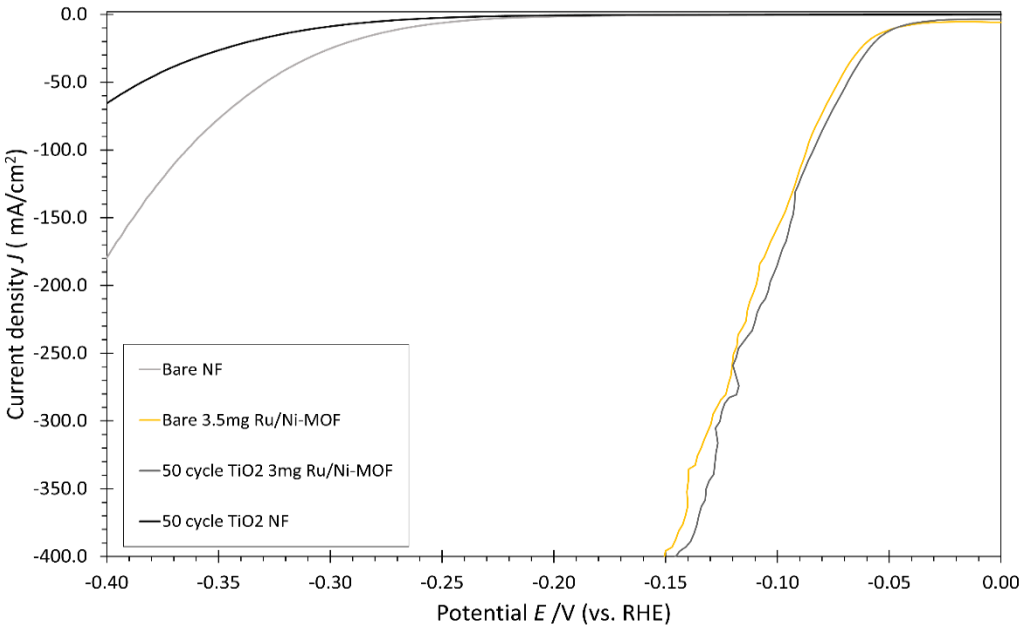


Figure 5.7 Polarisation curves for 3.5 mg/cm³ Ru/Ni-MOF and NF before and after 50 cycles of TiO_2 ALD.

The SEM images in Figure 5.8 of the Ru/Ni-MOF as prepared in (a) and (b) and after 50 ALD cycles of TiO_2 in (c) and (d) show visible reduction in the surface area coverage by the catalyst at low magnifications with little observable difference at higher magnifications. This accidental catalyst detachment could be a result of the plasma element of the PEALD being too harsh on the sensitive catalyst platform, similar to that seen in Chapter 4. No substantial differences are observed in the morphology of the NF control at these resolutions from before (e) and (f) and after the deposition in (g) and (h). It appears that small clusters of particles are visible in Figure 5.8 (g), which could be catalyst that has been dislodged from the Ru/Ni-MOF sample and redeposited on the NF control during the ALD as they were situated adjacent to each other during the process.

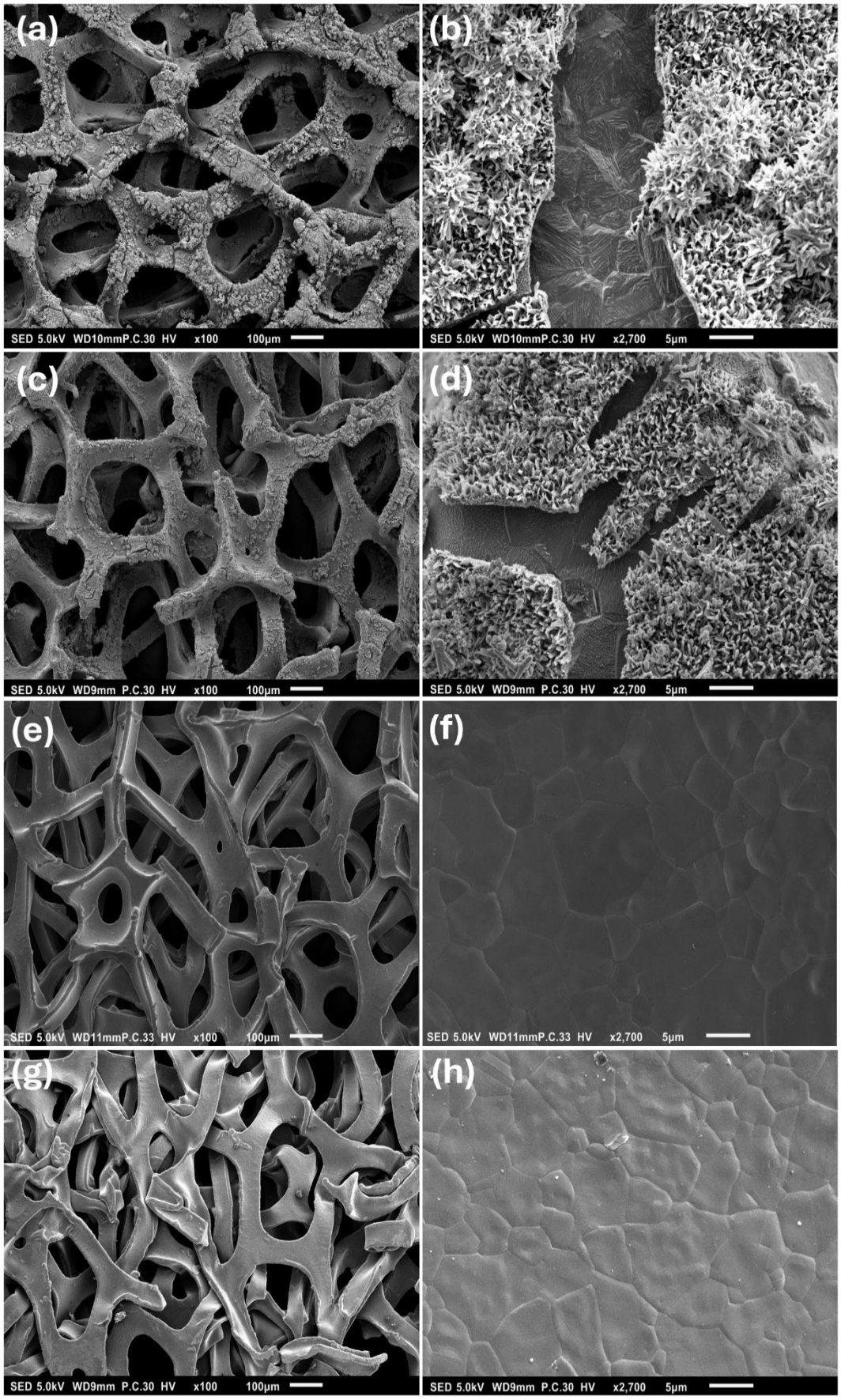


Figure 5.8 SEM images of the Ru/Ni-MOF before (a & b) and after (c & d) and the NF control before (e & f) and after (g & h) 50 cycles of TiO_2 ALD.

The PEALD of a TiO_2 thin film was successfully carried out using a TDMAT precursor at a chamber temperature of 200°C. Ti 2p signal was first detected on the Ru/Ni-MOF sample and NF control within the first ten ALD cycles, with stoichiometric TiO_2 deposition achieved by the 50^{th} cycle. Despite the successful deposition of a thin film on the Ru/Ni-MOF with no particularly negative effect to the overpotential, the similar change in overpotential for the uncoated and coated samples over time during HER experiments suggest its inefficiency as a protective layer for the electrode.

6. Conclusions and Future Work

6.1 Conclusions

This thesis reports an in-depth investigation into the performance of a Ru/Ni-MOF (on Ni foam) electrode for hydrogen evolution reactions and the surface modifications that can be implemented to increase efficiency and longevity to improve green labelled H_2 production technologies. In Chapter 3 the surface chemistry, morphology and electrochemical performance of the Ru/Ni-MOF electrode surface was characterised at each phase of electrode preparation. The reduced overpotential observed upon the introduction of Ru to the MOF demonstrates its effectiveness at increasing reaction kinetics. The overpotential of η = 85 mV for a current density of J = 100 mA/cm^2 that was achieved with a low catalyst loading was superior to that reported by studies developing similar electrodes and commercial Pt/C for HER in alkaline solutions at high current densities (> 130 mV at J = 100 mA/cm2) (63,64). The electrocatalytic performance of the Ru/Ni-MOF therefore has potential to reduce the cost of electrode materials whilst increasing efficiency by utilising smaller amounts of less precious metals. The role of the Ni-MOF structure as a catalyst platform was validated by increased catalyst retention, higher electrochemically active surface area and lower overpotential compared to the control samples of the NF and NiLDH. Although the Ru/Ni-MOF demonstrated an initial low overpotential at high current densities, the increase in overpotential with time for the long-term HER and the change in morphology observed by SEM suggested the insufficient longevity of the electrode requires improvement.

The effect of RF generated plasma treatments on the Ru/Ni-MOF and NF substrate was investigated in Chapter 4. The impact of chamber temperature for an NH_3-based plasma

treatment showed that the higher temperature of 270°C was sufficient at removing surface oxides from the NF and increasing catalyst exposure for the Ru/Ni-MOF. However, the small decrease in overpotential seen in the polarisation test and damage to the MOF structure suggested by SEM led to the conclusion that the high temperature plasma may have been too destructive to the Ru/Ni-MOF catalyst. A more significant decrease in overpotential as a result of plasma treatments may be observed if this process was performed on catalyst with a high starting overpotential, as the change in overpotential for the Ru/Ni-MOF catalyst may be limited by a Ru saturation point. When the temperature was decreased to 100°C, the NH_3-based plasma was less efficient for the treatment of the NF but caused a greater catalyst exposure with less visible damage for the Ru/Ni-MOF. The study of plasma treatment length of a H_2 plasma on the NF showed that the majority of the change in surface chemistry occurs within the first 5 minutes of treatment and stabilises significantly by the 10^{th} minute, with the removal of surface oxides and exposure of metallic Ni. The importance of in-situ plasma treatment and XPS characterisation was proven by a regrowth of the native oxide layer on the NF within 5 minutes of atmospheric exposure.

The plasma enhanced atomic layer deposition of TiO_2 protective coatings was conducted on the NF and Ru/Ni-MOF in an attempt to reduce the increase in overpotential as a function of time seen for the electrode during long-term stability HER tests. The complete dissociation of the TDMAT precursor was observed at the lowest process temperature suggested by the manufacturer. Stoichiometric TiO_2 was achieved by the 50^{th} cycle with the Ti 2p signal detected by XPS survey spectra within the first 10 cycles. Although it was concluded that the 50 cycles of applied TiO_2 coating had no particularly negative effect on the overpotential, it also appeared to have no specific positive effect

on the stability, resulting in similar changes in overpotential with time for both the uncoated and coated Ru/Ni-MOF. However, the evidential suppression of the Ni(II)/Ni(III) peak in the Ni characterisation CVs and the decrease in electrocatalytic performance after ALD for the NF imply there may have been a difference in the affinity and attachment ability of the TiO_2 coating to the two different substrates.

6.2 Future Work

As both the 100°C and 270°C NH_3-based plasma treatment processes resulted in extensive damage of the MOF catalyst framework, a more in-depth study into the effect of varying plasma process parameters could lead to a NH_3-based plasma recipe that achieves an appropriate level of surface modification to increase catalytic activity. Particularly, observing the change in surface chemistry and morphology at shorter plasma treatment length intervals may present an optimal treatment time to avoid excessive damage to the catalyst. The potential of the H_2 plasma in increasing catalyst adhesion to the NF could be supported by observing a change in the double-layer capacitance values of the modified substrate. An increase in the double-layer capacitance for the NF after H_2 plasma treatment could indicate a rougher surface which would lead to additional area for catalyst deposition. Following deposition onto the plasma modified substrate, an improvement in adhesion may be evident by a further increase in the C_{DL} and decrease in overpotential for the Ru/Ni-MOF on modified NF compared to the unmodified version.

The ALD of TiO_2 protective coatings to increase HER catalyst stability could be improved by conducting early-stage growth studies of the coatings on the Ru/Ni-MOF electrode to improve the nucleation of the film on the complex 3D structure. As the use of H_2 plasma

pre-treatments to increase surface hydroxyls has been reported to improve the nucleation of ALD TiO_2 films, it could be applied to the Ru/Ni-MOF to increase substrate-coating affinity. Continuation of the deposition of TiO_2 to higher ALD cycle numbers could be explored to improve the stability of the Ru/Ni-MOF in long-term H_2 production experiments.

Bibliography

1. European Union. Regulation (EU) 2021/1119 of the European Parliament and of the Council of 30 June 2021 establishing the framework for achieving climate neutrality and amending Regulations (EC) No 401/2009 and (EU) 2018/1999 ('European Climate Law') [Internet]. Brussels: Publications Office of the European Union; 2021. Available from: http://data.europa.eu/eli/reg/2021/1119/oj

2. United Nations. What is Climate Change? [Internet]. UN; [cited 2025 May 21]. Available from: https://www.un.org/sites/un2.un.org/files/fastfacts-what-is-climate-change.pdf

3. Howlett J, Belan M. The Quantum Mechanics of Greenhouse Gases | Quanta Magazine. Quanta Magazine [Internet]. 2025 Sep 15. Available from: https://www.quantamagazine.org/the-quantum-mechanics-of-greenhouse-gases-20250915/

4. (IEA) IEA. Global Energy Review 2026 [Internet]. 2026. Available from: https://www.iea.org/reports/global-energy-review-2026

5. Department of the Environment, Climate and Communications. National Hydrogen Strategy [Internet]. Government of Ireland; 2023 [cited 2025 Oct 16]. Available from: https://assets.gov.ie/static/documents/national-hydrogen-strategy.pdf

6. Sustainable Energy Authority of Ireland. Energy in Ireland [Internet]. Dublin: Government of Ireland; 2023 [cited 2025 May 21]. p. 177. Report EII-2023-1.3. Available from: https://www.seai.ie/sites/default/files/publications/Energy-in-Ireland-2023.pdf

7. Chi J, Yu H. Water electrolysis based on renewable energy for hydrogen production. Chinese Journal of Catalysis. 2018 Mar;39(3):390–4. doi:10.1016/S1872-2067(17)62949-8

8. Squadrito G, Maggio G, Nicita A. The green hydrogen revolution. Renewable Energy. 2023 Nov;216:119041. doi:10.1016/j.renene.2023.119041

9. Incer-Valverde J, Korayem A, Tsatsaronis G, Morosuk T. "Colors" of hydrogen: Definitions and carbon intensity. Energy Conversion and Management. 2023 Sep;291:117294. doi:10.1016/j.enconman.2023.117294

10. Hermesmann M, Müller TE. Green, Turquoise, Blue, or Grey? Environmentally friendly Hydrogen Production in Transforming Energy Systems. Progress in Energy and Combustion Science. 2022 May;90:100996. doi:10.1016/j.pecs.2022.100996

11. Chatenet M, Pollet BG, Dekel DR, Dionigi F, Deseure J, Millet P, et al. Water electrolysis: from textbook knowledge to the latest scientific strategies and industrial developments. Chem Soc Rev. 2022;51(11):4583–762. doi:10.1039/D0CS01079K

12. Esposito DV. Membraneless Electrolyzers for Low-Cost Hydrogen Production in a Renewable Energy Future. Joule. 2017 Dec;1(4):651–8. doi:10.1016/j.joule.2017.07.003

13. Jones ER, Bierkens MFP, Van Vliet MTH. Current and future global water scarcity intensifies when accounting for surface water quality. Nat Clim Chang. 2024 Jun;14(6):629–35. doi:10.1038/s41558-024-02007-0

14. Hassan NS, Jalil AA, Rajendran S, Khusnun NF, Bahari MB, Johari A, et al. Recent review and evaluation of green hydrogen production via water electrolysis for a sustainable and clean energy society. International Journal of Hydrogen Energy. 2024 Jan;52:420–41. doi:10.1016/j.ijhydene.2023.09.068

15. Emam AS, Hamdan MO, Abu-Nabah BA, Elnajjar E. A review on recent trends, challenges, and innovations in alkaline water electrolysis. International Journal of Hydrogen Energy. 2024 Apr;64:599–625. doi:10.1016/j.ijhydene.2024.03.238

16. Liu T, Guan Y, Wu Y, Chu X, Liu B, Zhang N, et al. Ru nanoparticles immobilized on self-supporting porphyrinic MOF/nickel foam electrode for efficient overall water splitting. International Journal of Hydrogen Energy. 2024 Feb;57:408–19. doi:10.1016/j.ijhydene.2024.01.026

17. Malek A, Lu X, Shearing PR, Brett DJL, He G. Strategic comparison of membrane-assisted and membrane-less water electrolyzers and their potential application in direct seawater splitting (DSS). Green Energy & Environment. 2023 Aug;8(4):989–1005. doi:10.1016/j.gee.2022.06.006

18. Medford AJ, Vojvodic A, Hummelshøj JS, Voss J, Abild-Pedersen F, Studt F, et al. From the Sabatier principle to a predictive theory of transition-metal heterogeneous catalysis. Journal of Catalysis. 2015 Aug;328:36–42. doi:10.1016/j.jcat.2014.12.033

19. Yang Y, Yu Y, Li J, Chen Q, Du Y, Rao P, et al. Engineering Ruthenium-Based Electrocatalysts for Effective Hydrogen Evolution Reaction. Nano-Micro Lett. 2021 Dec;13(1):160. doi:10.1007/s40820-021-00679-3

20. Johanna M. Wagner. X-ray Photoelectron Spectroscopy. 1st ed. Nova Science Publishers, Incorporated; 2010. 291 p. (Chemical Engineering Methods and Technology).

21. Pinder JW, Major GH, Baer DR, Terry J, Whitten JE, Čechal J, et al. Avoiding common errors in X-ray photoelectron spectroscopy data collection and analysis, and properly reporting instrument parameters. Applied Surface Science Advances. 2024 Feb;19:100534. doi:10.1016/j.apsadv.2023.100534

22. Stevie FA, Donley CL. Introduction to x-ray photoelectron spectroscopy. Journal of Vacuum Science & Technology A: Vacuum, Surfaces, and Films. 2020 Dec 1;38(6):063204. doi:10.1116/6.0000412

23. NIST X-ray Photoelectron Spectroscopy Database [Internet]. [cited 2025 Jul 31]. Available from: https://srdata.nist.gov/xps/

24. Moulder JF, Chastain J, editors. Handbook of X-ray photoelectron spectroscopy: a reference book of standard spectra for identification and interpretation of XPS data. Update. Eden Prairie, Minn: Perkin-Elmer Corporation; 1992. 261 p.

25. Le DN, Nguyen-Truong HT. Analytical Formula for the Electron Inelastic Mean Free Path. J Phys Chem C. 2021 Sep 2;125(34):18946–51. doi:10.1021/acs.jpcc.1c05212

26. Watts JohnF, Wolstenholme J. An Introduction to Surface Analysis by XPS and AES. New ed. Chichester: Wiley; 2003. 212 p.

27. Herrera-Gomez A. Effect of monochromator X-ray Bragg reflection on photoelectric cross section. Journal of Electron Spectroscopy and Related Phenomena. 2010 Nov;182(1–2):81–3. doi:10.1016/j.elspec.2010.07.009

28. Tougaard S. Practical guide to the use of backgrounds in quantitative XPS. Journal of Vacuum Science & Technology A. 2021 Jan 1;39(1):011201. doi:10.1116/6.0000661

29. Shard AG. Practical guides for x-ray photoelectron spectroscopy: Quantitative XPS. Journal of Vacuum Science & Technology A. 2020 Jul 1;38(4):041201. doi:10.1116/1.5141395

30. Major GH, Fairley N, Sherwood PMA, Linford MR, Terry J, Fernandez V, et al. Practical guide for curve fitting in x-ray photoelectron spectroscopy. Journal of Vacuum Science & Technology A. 2020 Dec;38(6):061203. doi:https://doi.org/10.1116/6.0000377

31. Greczynski G, Hultman L. X-ray photoelectron spectroscopy: Towards reliable binding energy referencing. Progress in Materials Science. 2020 Jan;107:100591. doi:10.1016/j.pmatsci.2019.100591

32. Biesinger MC. Accessing the robustness of adventitious carbon for charge referencing (correction) purposes in XPS analysis: Insights from a multi-user facility data review. Applied Surface Science. 2022 Sep;597:153681. doi:10.1016/j.apsusc.2022.153681

33. Greczynski G, Hultman L. A step-by-step guide to perform x-ray photoelectron spectroscopy. Journal of Applied Physics. 2022 Jul 1;132:11101. doi:10.1063/5.0086359

34. Isaacs MA, Davies PR, Graf A, Morgan DJ, Palgrave R. XPS Insight Note: Coster–Kronig Broadening. Surface and Interface Analysis. 2025;57(7):548–54. doi:10.1002/sia.7410

35. Joseph Goldstein, Dale E. Newbury, Patrick Echlin, David C. Joy, Alton D. Romig Jr, Charles e. Lyman, et al. Scanning Electron Microscopy and X-Ray Microanalysis : A Text for Biologists, Materials Scientists, and Geologists [Internet]. 2nd ed. Springer; 1992. 830 p. Available from: https://ebookcentral.proquest.com/lib/dcu/reader.action?docID=3077317&c=UERG&ppg=1

36. Goldstein J, Newbury DE, Echlin P, Joy DC, Romig Jr. AD, Lyman CE, et al. Chapter 2: Electron Optics. In: Scanning Electron Microscopy and X-Ray Microanalysis : A Text for Biologists, Materials Scientists, and Geologists. [Internet]. 2nd ed. New York, NY: Springer; 1992 [cited 2025 Oct 9]. Available from:

https://ebookcentral.proquest.com/lib/dcu/detail.action?pq-origsite=primo&docID=3077317

37. Khursheed A. Chapter 1: Conventional SEM Design. In: Scanning Electron Microscope Optics and Spectrometers [Internet]. 1st ed. Singapore: World Scientific Publishing Company; 2010 [cited 2025 Oct 9]. Available from: https://ebookcentral.proquest.com/lib/dcu/reader.action?docID=731284&ppg=15&c=UERG

38. Davies TE, Li H, Bessette S, Gauvin R, Patience GS, Dummer NF. Experimental methods in chemical engineering: Scanning electron microscopy and X-ray ultra-microscopy—SEM and XuM. The Canadian Journal of Chemical Engineering. 2022;100(11):3145–59. doi:10.1002/cjce.24405

39. Pillai RR, Thomas V. Plasma Surface Engineering of Natural and Sustainable Polymeric Derivatives and Their Potential Applications. Polymers. 2023 Jan 12;15(2):400. doi:10.3390/polym15020400

40. He B, Yang Y, Yuen MF, Chen XF, Lee CS, Zhang WJ. Vertical nanostructure arrays by plasma etching for applications in biology, energy, and electronics. Nano Today. 2013 Jun;8(3):265–89. doi:10.1016/j.nantod.2013.04.008

41. Qin C, Tian S, Jiang ZJ, Thandavarayan M, Jiang Z. Low temperature plasma-assisted synthesis and modification of water splitting electrocatalysts. Electrochimica Acta. 2023 May;449:142179. doi:10.1016/j.electacta.2023.142179

42. Zhang Y, Rawat RS, Fan HJ. Plasma for Rapid Conversion Reactions and Surface Modification of Electrode Materials. Small Methods. 2017;1(9):1700164. doi:10.1002/smtd.201700164

43. Yu F, Liu M, Ma C, Di L, Dai B, Zhang L. A Review on the Promising Plasma-Assisted Preparation of Electrocatalysts. Nanomaterials. 2019 Oct 10;9(10):1436. doi:10.3390/nano9101436

44. Oxford Instruments Plasma Technology. FlexAL II Original Instructions. 2018.

45. Seger B, Tilley DS, Pedersen T, Vesborg PCK, Hansen O, Grätzel M, et al. Silicon protected with atomic layer deposited TiO2: durability studies of photocathodic H2 evolution. RSC Adv. 2013;3(48):25902. doi:10.1039/c3ra45966g

46. Seger B, Pedersen T, Laursen AB, Vesborg PCK, Hansen O, Chorkendorff I. Using TiO2 as a Conductive Protective Layer for Photocathodic H2 Evolution. J Am Chem Soc. 2013 Jan 23;135(3):1057–64. doi:10.1021/ja309523t

47. Pastukhova N, Mavrič A, Li Y. Atomic Layer Deposition for the Photoelectrochemical Applications. Advanced Materials Interfaces. 2021;8(7):2002100. doi:10.1002/admi.202002100

48. Lin Y, Kapadia R, Yang J, Zheng M, Chen K, Hettick M, et al. Role of TiO2 Surface Passivation on Improving the Performance of p-InP Photocathodes. J Phys Chem C. 2015 Feb 5;119(5):2308–13. doi:10.1021/jp5107313

49. Swaminathan S, Shandalov M, Oshima Y, McIntyre PC. Bilayer metal oxide gate insulators for scaled Ge-channel metal-oxide-semiconductor devices. Applied Physics Letters. 2010 Feb 22;96(8):082904. doi:10.1063/1.3313946

50. Puurunen RL. A Short History of Atomic Layer Deposition: Tuomo Suntola's Atomic Layer Epitaxy. Chemical Vapor Deposition. 2014;20(10-11–12):332–44. doi:10.1002/cvde.201402012

51. Cremers V, Puurunen RL, Dendooven J. Conformality in atomic layer deposition: Current status overview of analysis and modelling. Applied Physics Reviews. 2019 Jun 1;6(2):021302. doi:10.1063/1.5060967

52. Oke JA, Jen TC. Atomic layer deposition and other thin film deposition techniques: from principles to film properties. Journal of Materials Research and Technology. 2022 Nov;21:2481–514. doi:10.1016/j.jmrt.2022.10.064

53. Johnson RW, Hultqvist A, Bent SF. A brief review of atomic layer deposition: from fundamentals to applications. Materials Today. 2014 Jun;17(5):236–46. doi:10.1016/j.mattod.2014.04.026

54. Dufond ME, Diouf MW, Badie C, Laffon C, Parent P, Ferry D, et al. Quantifying the Extent of Ligand Incorporation and the Effect on Properties of TiO_2 Thin Films Grown by Atomic Layer Deposition Using an Alkoxide or an Alkylamide. Chem Mater. 2020 Feb 25;32(4):1393–407. doi:10.1021/acs.chemmater.9b03621

55. Bienek O, Fuchs B, Kuhl M, Rieth T, Kühne J, Wagner LI, et al. Engineering Defects and Interfaces of Atomic Layer-Deposited TiOx-Protective Coatings for Efficient III–V Semiconductor Photocathodes. ACS Photonics. 2023 Nov 15;10(11):3985–97. doi:10.1021/acsphotonics.3c00818

56. O'Donnell S, Jose F, Shiel K, Snelgrove M, McFeely C, McGill E, et al. Thermal and plasma enhanced atomic layer deposition of ultrathin TiO2 on silicon from amide and alkoxide precursors: growth chemistry and photoelectrochemical performance. J Phys D: Appl Phys. 2022 Feb 24;55(8):085105. doi:10.1088/1361-6463/ac360c

57. Palmolahti L, Ali-Löytty H, Hannula M, Saari J, Wang W, Tukiainen A, et al. Pinhole-resistant nanocrystalline rutile TiO2 photoelectrode coatings. Acta Materialia. 2022 Oct;239:118257. doi:10.1016/j.actamat.2022.118257

58. Elgrishi N, Rountree KJ, McCarthy BD, Rountree ES, Eisenhart TT, Dempsey JL. A Practical Beginner's Guide to Cyclic Voltammetry. J Chem Educ. 2018 Feb 13;95(2):197–206. doi:10.1021/acs.jchemed.7b00361

59. Kawashima K, Márquez RA, Son YJ, Guo C, Vaidyula RR, Smith LA, et al. Accurate Potentials of Hg/HgO Electrodes: Practical Parameters for Reporting Alkaline Water Electrolysis Overpotentials. ACS Catal. 2023 Feb 3;13(3):1893–8. doi:10.1021/acscatal.2c05655

60. Mahendra R. Awode. Introduction to Electrochemistry [Internet]. 1st ed. Global Media; 2009. 232 p. Available from:

https://ebookcentral.proquest.com/lib/dcu/reader.action?docID=3011348&c=UERG&ppg=169

61. Łukaszewski M, Soszko M, Czerwiński A. Electrochemical Methods of Real Surface Area Determination of Noble Metal Electrodes – an Overview. International Journal of Electrochemical Science. 2016 Jun;11(6):4442–69. doi:10.20964/2016.06.71

62. Xu X, Li L, Chen HC, Zhang X, Huang Y, Humayun M, et al. Ru-Enriched Metal–Organic Framework Enabling a Self-Powered Hydrogen Production System. ACS Catal. 2024 Aug 16;14(16):12051–63. doi:10.1021/acscatal.4c03722

63. Sun Y, Xue Z, Liu Q, Jia Y, Li Y, Liu K, et al. Modulating electronic structure of metal-organic frameworks by introducing atomically dispersed Ru for efficient hydrogen evolution. Nat Commun. 2021 Mar 1;12(1):1369. doi:10.1038/s41467-021-21595-5

64. Li S, Zhou Z, Liu G, Zhang Q, Gao Y, Zhu H, et al. Confining ruthenium nanoparticles in MOF pores for high-performance hydrogen evolution reaction. Chemical Engineering Journal. 2024 Aug;493:152820. doi:10.1016/j.cej.2024.152820

65. Hameed A, Batool M, Liu Z, Nadeem MA, Jin R. Layered Double Hydroxide-Derived Nanomaterials for Efficient Electrocatalytic Water Splitting: Recent Progress and Future Perspective. ACS Energy Lett. 2022 Oct 14;7(10):3311–28. doi:10.1021/acsenergylett.2c01362

66. Deng L, Hu F, Ma M, Huang SC, Xiong Y, Chen HY, et al. Electronic Modulation Caused by Interfacial Ni-O-M (M=Ru, Ir, Pd) Bonding for Accelerating Hydrogen Evolution Kinetics. Angewandte Chemie International Edition. 2021;60(41):22276–82. doi:10.1002/anie.202110374

67. Xu Y, Yu S, Ren T, Liu S, Wang Z, Li X, et al. Hydrophilic/Aerophobic Hydrogen-Evolving Electrode: NiRu-Based Metal–Organic Framework Nanosheets In Situ Grown on Conductive Substrates. ACS Appl Mater Interfaces. 2020 Aug 5;12(31):34728–35. doi:10.1021/acsami.0c03333

68. Tran TTN, Le TA, Dinh NTT, Hai ND, Truong TK, Yu J, et al. Crystalline Ru-Decorated MOF-Derived Amorphous CoMo-LDH Nanosheet Arrays as Bifunctional Catalysts for Overall Natural Seawater Electrolysis. ACS Appl Mater Interfaces. 2024 Oct 9;16(40):53675–87. doi:10.1021/acsami.4c09232

69. Biesinger MC, Payne BP, Lau LWM, Gerson A, Smart RStC. X-ray photoelectron spectroscopic chemical state quantification of mixed nickel metal, oxide and hydroxide systems. Surface & Interface Analysis. 2009 Apr;41(4):324–32. doi:10.1002/sia.3026

70. Biesinger MC, Payne BP, Grosvenor AP, Lau LWM, Gerson AR, Smart RStC. Resolving surface chemical states in XPS analysis of first row transition metals, oxides and hydroxides: Cr, Mn, Fe, Co and Ni. Elsevier. 2011 Jan 15;257(7):2717–30. doi::10.1016/j.apsusc.2010.10.051

71. Biesinger MC, Lau LWM, Gerson AR, Smart RStC. The role of the Auger parameter in XPS studies of nickel metal, halides and oxides. Phys Chem Chem Phys. 2012;14(7):2434. doi:10.1039/c2cp22419d

72. Morgan DJ. Resolving ruthenium: XPS studies of common ruthenium materials. Surface & Interface Analysis. 2015 Nov;47(11):1072–9. doi:10.1002/sia.5852

73. Grey LH, Nie HY, Biesinger MC. Defining the nature of adventitious carbon and improving its merit as a charge correction reference for XPS. Applied Surface Science. 2024 Apr;653:159319. doi:10.1016/j.apsusc.2024.159319

74. Payne BP, Biesinger MC, McIntyre NS. Use of oxygen/nickel ratios in the XPS characterisation of oxide phases on nickel metal and nickel alloy surfaces. Journal of Electron Spectroscopy and Related Phenomena. 2012 Aug;185(5–7):159–66. doi:10.1016/j.elspec.2012.06.008

75. De BS, Kumar P, Khare N, Luo JL, Elias A, Basu S. Microfabrication of the Ammonia Plasma-Activated Nickel Nitride–Nickel Thin Film for Overall Water Splitting in the Microfluidic Membraneless Electrolyzer. ACS Appl Energy Mater. 2021 Sep 27;4(9):9639–52. doi:10.1021/acsaem.1c01772

76. Liu C, Tseng CY, Wang YC, Cheng IC, Chen JZ. Low-Pressure Plasma-Processed Ruthenium/Nickel Foam Electrocatalysts for Hydrogen Evolution Reaction. Materials. 2022 Apr 1;15(7):2603. doi:10.3390/ma15072603

77. Qadeer MA, Zhang X, Farid MA, Tanveer M, Yan Y, Du S, et al. A review on fundamentals for designing hydrogen evolution electrocatalyst. Journal of Power Sources. 2024 Sep;613:234856. doi:10.1016/j.jpowsour.2024.234856

78. Meier JC, Galeano C, Katsounaros I, Witte J, Bongard HJ, Topalov AA, et al. Design criteria for stable Pt/C fuel cell catalysts. Beilstein J Nanotechnol. 2014 Jan 16;5:44–67. doi:10.3762/bjnano.5.5

79. Kolle-Görgen E, Fortunato G, Ledendecker M. Catalyst Stability in Aqueous Electrochemistry. Chem Mater. 2022 Dec 13;34(23):10223–36. doi:10.1021/acs.chemmater.2c02443

80. Lee WJ, Bera S, Woo H, Kim HG, Baek JH, Hong W, et al. In Situ Engineering of a Metal Oxide Protective Layer into Pt/Carbon Fuel-Cell Catalysts by Atomic Layer Deposition. Chem Mater. 2022 Jul 12;34(13):5949–59. doi:10.1021/acs.chemmater.2c00928

81. Hannula M, Ali-Löytty H, Lahtonen K, Sarlin E, Saari J, Valden M. Improved Stability of Atomic Layer Deposited Amorphous TiO_2 Photoelectrode Coatings by Thermally Induced Oxygen Defects. Chem Mater. 2018 Feb 27;30(4):1199–208. doi:10.1021/acs.chemmater.7b02938

82. Avila JR, Qadri SB, Freitas JAJr, Nepal N, Boris DR, Walton SG, et al. Impact of Growth Conditions on the Phase Selectivity and Epitaxial Quality of TiO2 Films Grown by the Plasma-Assisted Atomic Layer Deposition. Chem Mater. 2019 Jun 11;31(11):3900–8. doi:10.1021/acs.chemmater.8b05282

83. Biesinger MC, Lau LWM, Gerson AR, Smart RStC. Resolving surface chemical states in XPS analysis of first row transition metals, oxides and hydroxides: Sc, Ti, V, Cu and Zn. Applied Surface Science. 2010 Nov;257(3):887–98. doi:10.1016/j.apsusc.2010.07.086

84. Lee CS, Kim J, Son JY, Choi W, Kim H. Photocatalytic functional coatings of TiO2 thin films on polymer substrate by plasma enhanced atomic layer deposition. Applied Catalysis B: Environmental. 2009 Sep;91(3–4):628–33. doi:10.1016/j.apcatb.2009.06.037

85. Tran HH, Nguyen CT, Tendero C, Battiato S, Vo DCT, Carlos E, et al. Precision nanoengineering of photoelectrochemical devices via atomic layer deposition. Materials Science and Engineering: R: Reports. 2026 Jan;168:101153. doi:10.1016/j.mser.2025.101153

86. Liu X, Su Y, Chen R. Atomic-scale engineering of advanced catalytic and energy materials via atomic layer deposition for eco-friendly vehicles. Int J Extrem Manuf. 2023 Apr;5(2):022005. doi:10.1088/2631-7990/acc6a7

Appendix A

The nickel foam (NF) substrate purchased from MTI was first successively washed, with ultrasonication, in absolute ethanol (EtOH) and deionised (DI) water for 15 minutes for the removal of organic residues from the surface. A 15 minute sonication in 3 M HCl solution was then conducted to remove the native oxide layer. The NF was then rinsed several times in DI water before a final 15 minute ultrasonication in absolute ethanol and then dried at 60°C in an oven for 2 hours. A Ni double-layered hydroxide (NiLDH) layer was grown on the pre-treated substrate. A solution of $Ni(II)Cl_3.6H_2O$ (1.87 g, 7.9 mmol) and urea (2.57 g, 42.8 mmol) was dissolved in 67 ml DI water, stirred for 30 minutes and transferred to a 110 ml PTFE autoclave vessel. A weighed section of NF (17.5 cm^2) was completely immersed in the solution in the vessel. The PTFE vessel was then inserted into a stainless-steel, acid digestion reactor (Parr Instrument Co. model 4748), which was then placed in a laboratory oven at 120°C for 12 hours before returning to ambient temperature. The NF was removed and was visibly coated with a loosely adhered film of green oxide as shown in Figure B1. It was then washed three times by careful immersion in DI water and then dried at 60°C overnight. The mass of the deposited oxide was determined by weighing the fully dried sample. The growth of the NiLDH layer was non-uniform and therefore was physically thinned until a loading of roughly 3 mg/cm^3 remained as seen in Figure B2.

A solution of Azobenzene-4,4'-dicarboxylic Acid (ABDC – 238 mg, 0.88 mmol) dissolved in 55 ml Dimethylformamide (DMF) was prepared to convert the NiLDH to a Ni metal-organic-framework (Ni-MOF). Ethanol and DI water (5.5 ml of each) were stirred into the solution over 30 minutes. The NiLDH was then inserted into the solution in a clean 110 ml PTFE autoclave vessel. The acid digestion reactor was once again assembled and

placed in an oven for 8 hours at 120°C. Upon cooling to room temperature naturally, the orange-coloured Ni-MOF was removed from the vessel. It was then washed by immersion in fresh ethanol 3 times and dried again overnight at 60°C before weighing. The substrate mass typically increased by 0.4-0.5 mg/cm^3 following this conversion.

The Ni-MOF/NF sample and NF and Ni-LDH/NF control samples were reduced to 1.1 cm × 3.9 cm strips and immersed in a solution of $RuCl_3.xH_2O$ in absolute ethanol within a screw-capped glass vial. The vials were placed in an oven at 80°C for 18 hours. Once again, the samples were allowed to cool to room temperature before being removed from the vials and washed several times with absolute ethanol and DI water and drying at 80°C overnight. The Ru treatment involved in the preparation of the controls was identical to that described for the Ru/Ni-MOF except that either bare NF or the mass-reduced Ni-LDH/NF was used as the substrate.

Samples at each stage of the Ru/Ni-MOF electrode production and control sample synthesis are reproducible at a macroscale upon following the above procedure precisely. This level of reproducibility was confirmed by visual inspection and also by recording mass changes in the electrode. However, as the catalyst intrinsically does not grow entirely uniformly on the porous substrate from this deposition technique, in-depth characterisation by XPS and SEM were carried out for each individual sample to confirm the consistency of the sample characteristics before use in modification experiments.

Appendix B

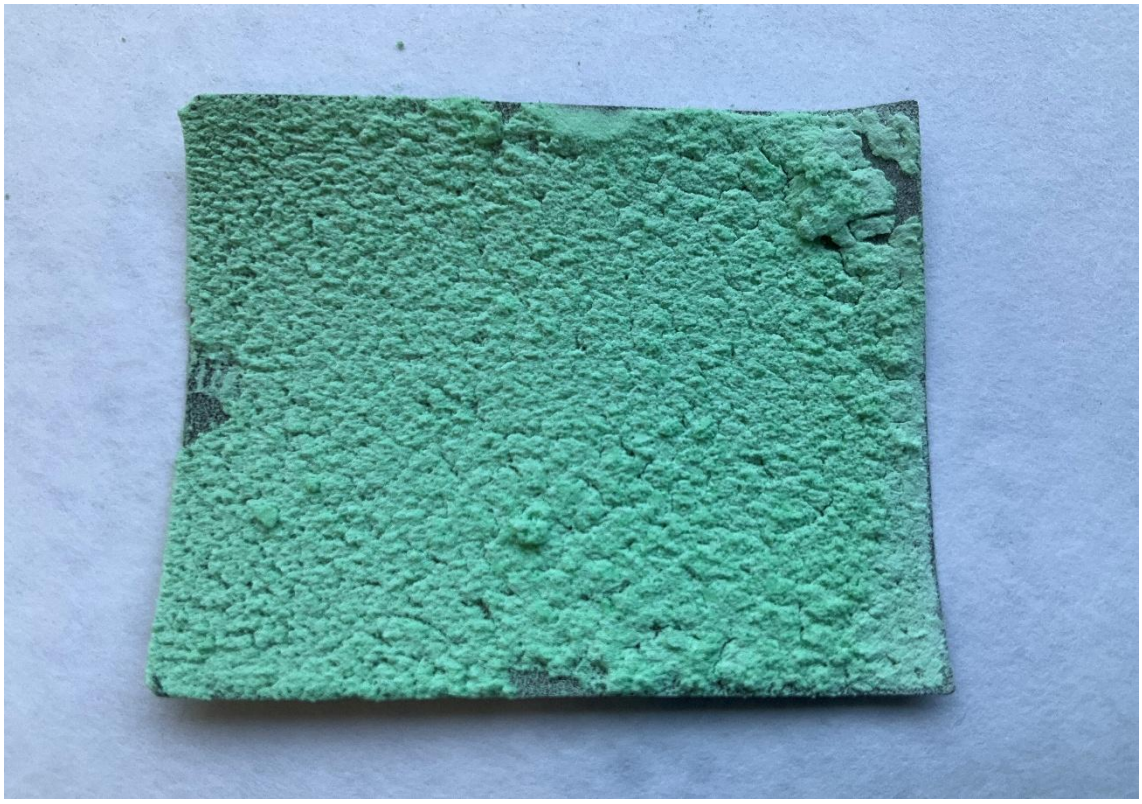


Figure B1 Non-uniform growth and green appearance of the Ni LDH on the Ni foam substrate shown as produced.

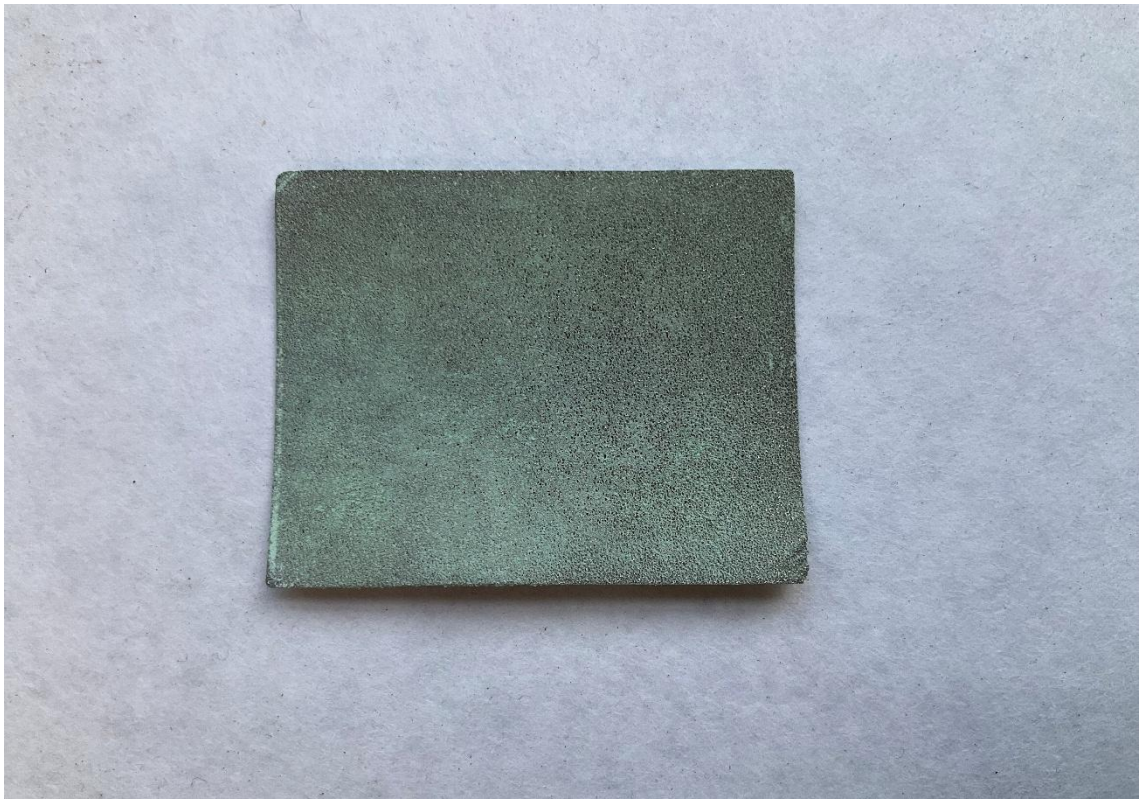


Figure B2 Ni LDH sample after physical thinning was carried out to obtain a loading of approximately 3 mg/cm^3.